

2003

Time-resolved optical studies of colossal magnetoresistance and charge -density wave materials

Yuhang Ren

College of William & Mary - Arts & Sciences

Follow this and additional works at: <https://scholarworks.wm.edu/etd>



Part of the [Condensed Matter Physics Commons](#), and the [Optics Commons](#)

Recommended Citation

Ren, Yuhang, "Time-resolved optical studies of colossal magnetoresistance and charge -density wave materials" (2003). *Dissertations, Theses, and Masters Projects*. Paper 1539623421.

<https://dx.doi.org/doi:10.21220/s2-p9sh-7514>

This Dissertation is brought to you for free and open access by the Theses, Dissertations, & Master Projects at W&M ScholarWorks. It has been accepted for inclusion in Dissertations, Theses, and Masters Projects by an authorized administrator of W&M ScholarWorks. For more information, please contact scholarworks@wm.edu.

**TIME-RESOLVED OPTICAL STUDIES OF COLOSSAL MAGNETO-
RESISTANCE AND CHARGE-DENSITY WAVE MATERIALS**

A Dissertation

Presented to

The Faculty of the Department of Applied Science

The College of William and Mary in Virginia

In Partial Fulfillment

Of the Requirements for the Degree of

Doctor of Philosophy

By

Yuhang Ren

April 2003

APPROVAL SHEET

This dissertation is submitted in partial fulfillment of

the requirements for the degree of

Doctor of Philosophy

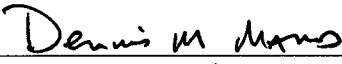


(Yuhang Ren)

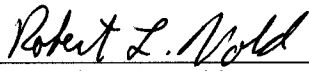
Approved, April 2003



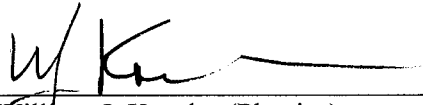
Gunter Lüpke (Advisor)



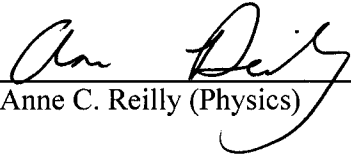
Dennis M. Manos



Robert L. Vold



William J. Kossler (Physics)



Anne C. Reilly (Physics)

Dedicated to my parents, Jifu Ren & Meiyang Zhang

and

my wife, Ying Wang

Contents

Acknowledgements	v
List of Figures	vii
Abstract	xi
1 Introduction	2
1. 1 Strongly correlated electron systems	2
1. 2 Time-resolved nonlinear optical spectroscopy.....	8
1. 3 Scope of this thesis	10
1. 4 Outline.....	12
2 Theory of time-resolved optical spectroscopy	14
2. 1 Photoexcited carrier relaxation.....	15
2. 1. 1 Coupled electron lattice systems.....	16
2. 1. 2 Correlated spin systems.....	19
2. 2 Photoexcited collective modes	21
2. 2. 1 Amplitudon oscillations	21
2. 2. 2 Phason oscillations.....	26
3 Experimental details	33
3. 1 Femtosecond time-resolved optical spectroscopy	33
3. 1. 1 Three-wave mixing processes as an infrared source.....	34
3. 1. 2 Pulse generation for pump-probe experiments	36

3. 1. 3 Experimental setup.....	42
3. 2. 1 Quasi-one dimensional CDW conductors	45
3. 2. 2 CMR manganites	46
4 Low dimensional CDW systems.....	48
4. 1 Introduction to quasi-one dimensional CDW conductor	49
4. 1. 1 CDW ordering in quasi-1D materials	49
4. 1. 2 Collective excitations in 1D CDW conductors.....	50
4. 2 Low-energy CDW dynamics.....	53
4. 2. 1 Dispersion relation of the collective modes	53
4. 2. 3 Anisotropy of the transverse phason.....	59
5 Colossal magneto-resistance manganites	64
5. 1 Introduction	65
5. 1. 1 Electronic properties of doped manganites	65
5. 1. 2 Charge ordering and phase separation of CMR manganites	67
5. 2 Experimental results	69
5. 2. 1 Opening of pseudogap.....	69
5. 2. 2 Dispersion relation of the collective mode.....	75
5. 2. 3 Temperature evolution of the collective mode.....	81
5. 2. 4 Quasiparticle dynamics	85
5. 2. 4 Slow spin relaxation process	89
5. 2. 5 Strain-effect on spin relaxation dynamics.....	94
6 Summary and conclusions.....	99
Bibliography	102
Vita.....	119

Acknowledgements

First of all, I would like to thank my advisor, Professor Gunter Lüpke. I greatly appreciate the advice and support he provided me throughout my time at College of William and Mary. His overwhelming knowledge, scientific tenacity, and optimism contributed invaluable to this work. For this and for critically reviewing the manuscript I am indebted to him.

My sincere gratitude goes to Prof. Marshall F. Onellion and Michael Schneider from the University of Wisconsin-Madison for initiation of this research. I have been fortunate in having some wonderfully intelligent peers to discuss ideas with and to learn from. Dr. K. A. Nelson (MIT), Dr. Ivan Bozovic (Stanford Uni.) are fellow femtosecond spectroscopists, and many of the ideas presented here have been developed and refined in conversations with these individuals. I have also learned things of value from all the other Lüpke group members and lab mates that I have worked with: Haibin Zhao, Shuyan Zhang, Xinghui Zhang, Baozhou Sun, Hailong Huang, Qiguang Yang, and Keoki Seu.

Particular thanks are due to our collaborators: Dr. Qi Li and Yufeng Hu from Penn. Stat. University, Dr. Zhuan Xu from Zhejiang University, China, and Dr. N. H. Hur and Dr. H. S. Hong from Korea Research Institute of Standards and Science. It would be impossible for us to finish this work if they didn't provide us with high quality manganite and charge-density-wave thin films and single crystals.

I would also like to express my appreciation to my doctoral dissertation committee members: Dr. Dennis M. Manos, Dr. Robert L. Vold of Applied Science, Dr. William J. Kossler and Dr. Anne Reilly of Physics for agreeing to serve. I especially appreciate their career advice and encouragement during my stay here.

Finally, I wish to express my gratitude to my family, whose support and encouragement has been invaluable to my academic success: my parents, Jifu Ren and Meiyang Zhang, who instilled in me a love of learning and the value of perseverance, and who have provided love and assistance from afar; my wife Ying Wang, who provided endless love and support during the past four years, without her I don't think I would have made it through this place; my parents-in-law, Zhifang Lu and Wenjun Wang, who provided encouragement, great holiday meals, and baby-sitting and my brothers, Yugang Ren and Yuke Ren. They are the foundation for who I am, and anything I have been able to accomplish is a tribute to them.

List of Figures

Figure	Page
1. The schematic structure of $K_{0.3}MoO_3$.	5
2. a) Crystal structure of doped manganites: $La_{1-x}RE_xMnO_3$ b) the magnetic phase diagram of the $La_{1-x}Ca_xMnO_3$ system from Schiffer et al. [18].	6
3. An excitation-deexcitation cycle. Details see text.	16
4. A schematic of amplitudon excitation in 1D CDW.	22
5. a) A schematic of longitudinal phason excitation in 1D CDW; b) A schematic of transverse phason excitation.	27
6. Schematic diagram of phason excitation and detection.	29
7. Configuration of the mode-locked Ti:sapphire laser (Tsunami, Spectra-Physics).	37
8. A schematic of the regenerative Ti:sapphire amplifier system.	39
9. Layout of the optical parametric amplifier (OPA-800C, Spectra-Physics).	41
10. Pump-probe setup for two color experiments.	43
11. Pump-probe setup for one-color experiments.	45
12. a) Photograph of $K_{0.33}MoO_3$ single crystal having a typical dimension of 2 cm along b axis; b) Resistivity (ρ) along the chain direction as a function of temperature in $K_{0.3}MoO_3$.	46
13. Resistivity (ρ) as a function of temperature in NSMO thin films on different substrates.	47
14. Transient reflectivity change ΔR at 800-nm probe wavelength	

- from $K_{0.3}MoO_3$ single crystal at 35 K. The inset depicts the fast oscillations on a short time scale. 54
15. Transverse phase (Ω_-) and amplitude (Ω_+) mode dispersion relations of $K_{0.3}MoO_3$ at 30 K in the long-wavelength limit. 55
16. The time evolution of ΔR at $E \parallel b$ for: a) $K_{0.3}MoO_3$ single crystal at 30 K; and b) $K_{0.33}MoO_3$ single crystal at 290 K with the pump laser wavelength at 800 nm, and the probe wavelength at 800 nm and 400 nm, respectively. 58
17. a) Transient reflectivity change ΔR in $K_{0.3}MoO_3$ at 400-nm probe wavelength with the polarization vector parallel ($E \parallel b$) and perpendicular ($E \perp b$) to the chain direction. The inset shows the anisotropy of the oscillation period in the a' - b plane; b) Anisotropy of ΔR for different probe polarization angle with respect to the b axis (θ vs. b) on $K_{0.33}MoO_3$. 60
18. Temperature dependence of the transverse phason velocity, c_{\parallel} , in $K_{0.3}MoO_3$ along the chain direction. 61
19. A schematic phase diagram of doped manganites from N. Mathur et al [16]. 67
20. A schematic illustrating the up- and down-spin density of states for perovskite manganites. The experimental observed pseudogap at E_F is also indicated [99]. 70
21. Thermomodulation mechanism: a) Photoexcitation, where the arrows represent possible electronic transitions from occupied (hatched) to unoccupied electronic states; b) Fermi smearing thereby opening some states and blocking others for optical

transition; c) A derivative-like feature (i.e. absorption $\Delta\alpha$) with respect to the probe photon energy ω when the probe photon energy matches the energy of d-band to E_F transition.	71
22. Reflectivity change ΔR_0 (at $\Delta t = 0$) in LCMO single crystal as a function of a) temperature with a probe energy at 0.51 eV, 1.08 eV, and 1.55 eV; b) probe energies at 10 K and 60 K.	73
23. Time evolution of ΔR for LCMO single crystal at 180 K.	74
24. a) Time evolution of reflectivity change, ΔR for LCMO thin film with probe wavelengths varied from ultraviolet to mid-infrared; b) Fourier transforms of the ΔR traces shown in a).	76
25. Collective mode dispersion relation of LCMO at room temperature.	77
26. a) Schematic of density wave formation: k -space as indicated from ARPES measurements; b) CE-type structure proposed in LCMO along the c axis by Asaka et al. [42]; c) density wave formation in real space with a wave length of $3.3a$ for layered manganites [26].	78
27. Transient reflectivity change ΔR of LCMO on NGO at different temperatures near T_C .	82
28. (a) Coherent oscillations of LCMO at different temperatures without decay components; (b) Fourier transforms of the signal transients shown in (a).	83
29. Crystallographic representation of the one-dimensionally modulated structure associated with CDW in a layered manganite, $\text{La}_{1.2}\text{Sr}_{1.8}\text{Mn}_2\text{O}_7$ [131].	84
30. ΔR_0 of LCMO vs temperature for two different pump beam power.	86

31. Temperature dependence of second fast relaxation component, τ_B ; Inset shows the power dependence of ΔR_0 . 87
32. Transient reflectivity ΔR of: a) LCMO and b) LMO single crystals around T_C (or T_N) at 800 nm wavelength. The dotted lines indicate the zero position. 89
33. Temperature dependence of $\Delta \tilde{R}$ at $\Delta t = 500$ ps: a) LCMO single crystal ($\lambda_{\text{pump}} = 1.4 \mu\text{m}/\lambda_{\text{probe}} = 800$ nm) and 400-nm thin film ($\lambda_{\text{pump}} = 800$ nm / $\lambda_{\text{probe}} = 5.2 \mu\text{m}$), and b) LMO single crystal ($\lambda_{\text{pump}} = 1.29 \mu\text{m}/\lambda_{\text{probe}} = 800$ nm). The solid lines indicate the power-law dependence. 90
34. The relaxation time τ_B as a function of temperature for LCMO and LMO single crystals. The solid line indicates the power-law dependence. The inset depicts a schematic diagram of carrier excitation/relaxation processes in LCMO. 92
35. Transient reflectivity ΔR of NSMO (400 nm) on different substrates: (a) LaAlO₃ (001), (b) SrTiO₃ (001), NdGaO₃ (110), and (d) NdGaO₃ (110) with post-oxygen annealing. The dotted lines indicate the zero position. 94
36. Long relaxation component Π vs temperature obtained from ΔR for different strained NSMO thin films. The solid lines show fits of Eq. (31). 96

Abstract

This thesis presents measurements of collective modes and ultrafast carrier relaxation dynamics in charge-density-wave (CDW) conductors and colossal magneto-resistance (CMR) manganites by means of femtosecond time-resolved optical spectroscopy. In these experiments, a femtosecond laser pump pulse excites a broad frequency spectrum of low-energy collective modes and electron-hole pairs via interband transitions in the material, thereby changing its optical properties. The low-energy collective excitations and quasiparticle relaxation and recombination processes are monitored by measuring the resulting photoinduced absorption as a function of probe pulse wavelength and time delay after photoexcitation. Therefore, the technique enables direct real-time measurements of non-equilibrium low-energy collective excitations and quasiparticle recombination dynamics.

First, we developed a general model to describe the photogeneration and detection mechanism of collective modes based on light absorption in two-color pump-probe experiments. The excitation of the density wave states can be well described by a spatially and time-dependent order parameter, which includes phase and amplitude excitations (phasons and amplitudons). The excitation mechanism is different from previous pump-probe transmission experiments in weakly absorbing crystals, in which the wave-vector of the excited modes is determined by the phase-matching condition of the pump beam. Since the absorption depth in CMR and CDW conductors is ~ 100 nm for wavelengths in the visible to infrared range, a broad spectrum of collective modes with frequencies down to a few GHz are excited and propagate normal to the surface into the material. According to the model, the dispersion of the long-wavelength phason and amplitudon can be measured by changing the probe wavelength.

Second, we performed the first pump-probe spectroscopy from the ultraviolet to mid-infrared wavelength range to study low-frequency collective excitations, including temperature evolution, dispersion, damping, and anisotropy of amplitude mode and transverse phason in quasi-one dimensional CDW conductors, $\text{K}_{0.3}\text{MoO}_3$ and $\text{K}_{0.33}\text{MoO}_3$ on ultrafast time scale. The transverse phason exhibits an acoustic-like dispersion relation in the frequency range from 5 – 40 GHz. The phason velocity is strongly anisotropic with a very weak temperature dependence. In contrast, the amplitude mode exhibits a weak (optic-like) dispersion relation with a frequency of 1.66 THz at 30 K.

Third, we present femtosecond time-resolved infrared spectra from doped perovskite manganite thin films and single crystals. A low-energy collective mode is observed and discussed in terms of the opening of a pseudogap resulting from charge/orbital ordering phases. The softening of the collective mode cannot be explained solely by electronic instability. A cooperative Jahn-Teller type distortion of the MnO_6 octahedra coupled to the collective mode is necessary to explain our results. Moreover, the quasiparticle dynamics in the vicinity of the metal-insulator transition is strongly affected by the presence of a pseudogap, phase separation and percolation, which are strongly dependent on temperature. Furthermore, a very long-lived relaxation process is observed, both in the metallic and insulating phase but which is absent in the paramagnetic phase. Therefore it is ascribed to a slow spin relaxation process. The dynamics of the spin system is further investigated in strained and unstrained thin films, which show a strong strain effect.

**TIME-RESOLVED OPTICAL STUDIES OF COLOSSAL MAGNETO-
RESISTANCE AND CHARGE-DENSITY WAVE MATERIALS**

Chapter 1

Introduction

1.1 Strongly correlated electron systems

Understanding the physics of strongly correlated systems [1] – i.e., systems exhibiting a strong interplay among the electronic-, lattice-, spin-, and/or orbital degrees of freedom (e.g., the high T_C cuprates [2], magnetic oxides [1, 3-5], heavy fermion systems [6], etc.) – has evolved into one of the most important problems confronting the condensed matter and materials science communities for several reasons.

First, strongly correlated systems tend to exhibit a rich variety of phases due to a strong competition among the various degrees of freedom [1]. The complex phase diagrams of correlated systems typically involve the close proximity of disparate phases, such as antiferromagnetic insulating, exotic superconducting, ferromagnetic, and non-Fermi liquid metallic, whose relationships are not yet well understood. It is therefore of great scientific interest to explore the relationship among the disparate

phases exhibited by these systems, particularly by studying the evolution of structural and dynamical properties of these systems across their diverse phase boundaries.

The effect of strong electron-electron correlations on the basic properties of a compound can be seen by considering the case of LaMnO_3 , which, although not discussed further in this thesis, represents a very typical example. This oxide, if treated within the independent-electron approximation (i.e., writing the total wave function of the N -electron system in the form of an antisymmetrized product of single-electron wave functions), is expected to be metallic, with an odd number of electrons per unit cell and a partially filled d -band. In reality, as a consequence of strong correlations, which suppress charge fluctuations and therefore the electrical conductivity, LaMnO_3 is a rather good insulator at all temperatures, with an optical gap of about 3 eV [7].

Second, the diverse phases of many strongly correlated systems are also associated with exotic and dramatic phenomena whose origins are not yet well understood, including: “colossal” sensitivities of physical properties (e.g., structure, transport properties, magnetic properties, etc.) to external perturbations, including magnetic field [8-9], and optical illumination [10]; self-organization of charges (e.g., charge ‘stripe’) [11], orbitals (e.g., orbital-ordering) [11], and/or spins (e.g., magnetic polaron formation); and exotic phase behavior, such as non-Fermi liquid behavior, and electronic phase separation on length scales ranging from nanometer to micrometer [12]. Understanding the nature and origin of these exotic phenomena, as well as the novel states of matter exhibited by correlated systems, is of great scientific interest.

Third, in addition to the substantial fundamental interest in the exotic properties exhibited by strongly correlated systems, it has long been recognized that the dramatic

responsiveness of these materials to external control makes these systems potentially technologically useful as switches, sensors, and storage components. Importantly, a deeper understanding of how the exotic phases and physical properties of strongly correlated systems can be controlled is an essential prerequisite to effectively utilizing these systems as devices.

The dramatic transport properties exhibited by strongly correlated systems have raised a common central issue: what is the nature of the low-energy collective excitations? The low-energy collective modes participate in the diverse phase transitions exhibited by correlated systems and they respond to small external perturbations that drive static and dynamical transport. The collective modes, including the orbital degree of freedom, have a great impact on extraordinary properties. For example, Chuang et al. concluded that the exotic Fermi-surface topology in a layered manganite $\text{La}_{1.2}\text{Sr}_{1.8}\text{Mn}_2\text{O}_7$ is due to charge density wave (CDW) instabilities even in the ferromagnetic metallic state [13].

A detailed understanding of the intricate dynamics of electronic-, lattice-, spin-, and/or orbital degrees of freedom in strongly correlated systems therefore requires a careful investigation of how the low energy excitations evolve through the various phases of correlated systems. In this thesis, we apply time-resolved optical techniques to investigate the low energy dynamics of two prototypical strongly correlated systems:

a) CDW conductors

One-dimensional systems with modulated CDW are ideal for studying collective excitation phenomena. One such example is the linear chain compound $\text{K}_{0.3}\text{MoO}_3$ (KMO) which undergoes a metal-insulator transition at $T_{\text{CDW}} = 183$ K. A CDW ground state develops below T_{CDW} where the long-range order appears. Above the

Peierls transition temperature, KMO is an anisotropic metal. Electrical conductivity along the chains is typically three orders of magnitude smaller than that of copper and one to three orders of magnitude larger than perpendicular to the chains [14].

The structure of KMO contains rigid units comprised of clusters of ten distorted MoO_6 octahedra, sharing corners along the monoclinic b -axis, as illustrated in Fig. 1. This corner sharing provides an easy path for the conduction electrons along the chain direction. The chains of the distorted MoO_6 octahedra also share corners along the $[102]$ direction and form infinite slabs separated by the alkaline cations. Along the chains, electrons are highly delocalized.

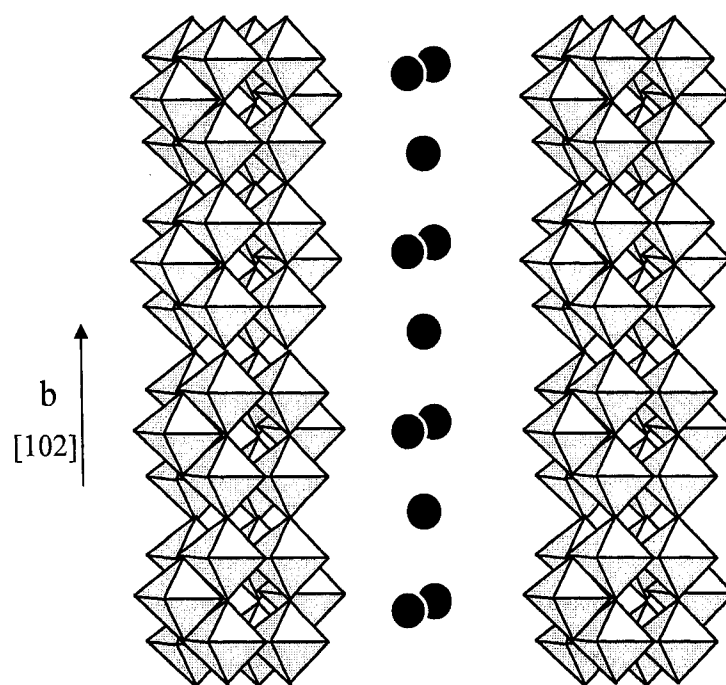


Figure 1. The schematic structure of $\text{K}_{0.3}\text{MoO}_3$ [14].

b) Doped Manganites

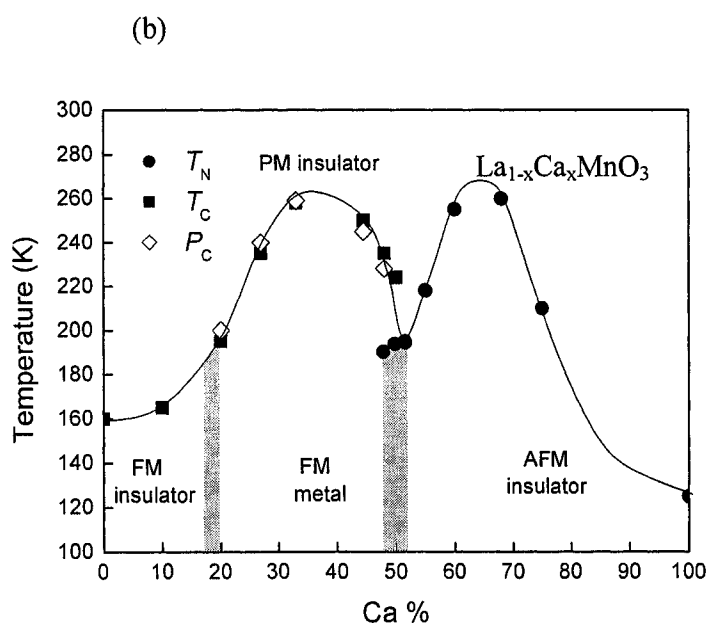
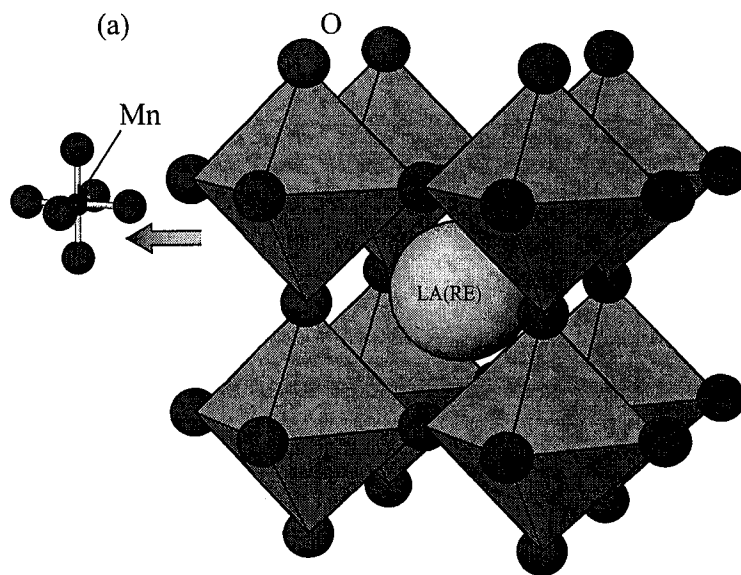


Figure 2. a) Crystal structure of doped manganites: $\text{La}_{1-x}\text{RE}_x\text{MnO}_3$ b) the magnetic phase diagram of the $\text{La}_{1-x}\text{Ca}_x\text{MnO}_3$ system from Schiffer et al. [18].

Thin films of doped manganites with large magnetoresistance at room temperature open up new possibilities for applications in diverse areas of technology, including

magnetic random access memories and read heads for hard disk drives. The recent interest in magnetoresistance of doped perovskite manganites was initiated by the discovery of a large room-temperature magnetoresistance, of the order $\Delta R/R(H=0) > 60\%$ with a 7-tesla field, in epitaxial thin films, $\text{La}_{0.67}\text{Ba}_{0.33}\text{MnO}_3$ [15]. This was soon followed by the report of McCormack et al. [16] and Jin et al. [17] that thin-film $\text{La}_{0.67}\text{Ca}_{0.33}\text{MnO}_3$ exhibits $\Delta R/R(H=6 \text{ T}) = 127000\%$ at 77 K. This large magnetoresistance effect has since been referred to as “colossal magnetoresistance”.

Manganites share the same crystal structure as the mineral perovskite. As shown in Fig. 2 (a), each manganese atom is surrounded by six equal-distance oxygen atoms to form a regular MnO_6 octahedron. The six oxygen atoms occupy the faces of a cube. Between the octahedral, at the corners of the cubes, lies a mixture of trivalent rare earth (LA) and divalent alkaline earth (RE) cations. These cations act as a charge reservoir for the manganese-oxygen bonds. Manganites have the general formula $\text{La}_{1-x}\text{RE}_x\text{MnO}_3$, and the overall manganese valence ranges from 3+ (atomic $3d^4$ configuration at $x=0$) to 4+ ($3d^3$ at $x=1$).

The magnetic phase diagram of the $\text{La}_{1-x}\text{Ca}_x\text{MnO}_3$ system is shown in Fig. 2(b) [18]. This phase diagram is also qualitatively true for other doped manganite perovskites such as $\text{Nd}_{1-x}\text{Sr}_x\text{MnO}_3$ and $\text{La}_{1-x}\text{Sr}_x\text{MnO}_3$ [1]. The Curie temperature peaks around $x \sim 0.3$. The maximum Curie temperature of 380 K was observed in $\text{La}_{0.7}\text{Sr}_{0.3}\text{MnO}_3$. The structural properties of the doped manganite perovskites show a strong correlation to their magnetic state. When the value of doping level x is increased, a metallic and ferromagnetic state develops, accompanied by a diminishing orthorhombic distortion.

1. 2 Time-resolved nonlinear optical spectroscopy

The experimental requirements for studying low-energy dynamics of complex phase behavior and phase transitions in strongly correlated systems are quite severe, particularly in the long-wavelength limit. Specifically, the need to investigate the low energy dynamics directly in systems for which the charge-, spin-, lattice-, and orbital-degrees of freedom are often of comparable importance demands a versatile spectroscopy capable of coupling to all these excitations. While stationary infrared spectroscopy measures the total of all contributions to the mid-infrared reflectivity and cannot clearly discern spectrally similar components, nonlinear time-resolved spectroscopy can provide such a distinction by separating the components in the time-domain.

Nonlinear optical interactions of laser fields with matter provide powerful spectroscopic tools for the understanding of microscopic interactions and dynamic processes. The ability to control pulse duration (to few femtoseconds), bandwidths (up to a 1 Hz resolution), and peak intensities (up to 10^{19} W/cm²) provides novel probes of elementary dynamic events. The advent of laser pulse sequences with controlled shapes and phases have opened up new directions with exciting possibilities. By virtue of the recent development of femtosecond lasers, ultrafast time-domain spectroscopies, especially pump-probe techniques, have been applied to studies of coherent excitations in various materials.

The strong coupling between spin, charge, and lattice degrees of freedom in strongly correlated systems makes it possible to manipulate the material properties via cooperative effects induced by optical excitation. The characteristic of the approach is that the system investigated is no longer in thermodynamic equilibrium. It is rather in an excited state whose decay into electronic-, spin-, and lattice- degrees of freedom is

being probed. The electromagnetic responses of the materials often occur on different time-scale. Recent ultrafast optical experiments on high- T_C superconductors (HTS) and colossal magnetoresistance (CMR) materials have given information on the time scales of carrier and condensate relaxation dynamics by nonequilibrium excitation of the carrier system at photon energies of 1.5 eV and subsequently studying its dynamics either at the same interband energies or in the far-infrared range [19-21]. Furthermore, the pump-probe technique has been shown to be a powerful tool for studying ultrafast magnetization dynamics. Time resolved magneto-optical techniques have been employed in ordinary metals to investigate de- and re-magnetization for several years, beginning with the key experiment by Beaurepaire et al. [22]. Most recently, a pump-probe magneto-optical Kerr effect (MOKE) technique has been employed to the direct investigation of ultrafast spin dynamics in a double exchange ferromagnet, $\text{Sr}_2\text{FeMoO}_6$ [23]. The authors observed a slow spin relaxation process toward the quasi-equilibrium state through weak heat exchange with the reservoir at quasi-equilibrium temperature [23].

In order to clarify the mechanisms behind the formation of the low-energy condensate of strongly correlated systems, it is essential to understand the elementary excitations in the mid-infrared energy range [24]. The low-energy electromagnetic response of strongly correlated systems contains valuable information on electronic excitations and their correlated dynamics. However, the collective modes usually appear in the millimeter range ($\sim 1-10$ meV), which is very difficult to reach by conventional optical spectroscopy. The limitation has been overcome by using mid-infrared pump-probe and THz time-domain spectroscopy (TDS), which are powerful tools to reveal the low-energy charge dynamics of strongly correlated material systems [24-25]. In particular, THz time-domain spectroscopy is a coherent ultrafast

optical technique in which electric field transients are used to measure the complex conductivity of a material. A sample can be optically excited and probed with a terahertz (THz) pulse to measure induced conductivity changes with picosecond resolution. Spin- and lattice- relaxation dynamics have been demonstrated with THz-TDS in $\text{La}_{0.7}\text{Ca}_{0.3}\text{MnO}_3$ and $\text{La}_{0.7}\text{Sr}_{0.3}\text{MnO}_3$ thin films [25].

Recently, time-resolved optical studies revealed collective excitations in the CDW conductor KMO [26]. Here, we present two-color spectroscopic experiments pump probe of CDW conductors and CMR manganites in the mid-infrared regime. The data provide completely new spectroscopic information on the dispersion relation and temperature evolution of low energy excitations in strongly correlated systems [26]. We will discuss in detail the detected collective oscillation modes and the electronic and/or magnetic excitation and relaxation processes, in order to explore the low energy dynamics of different correlated phases, and elucidate the manner in which these dynamics evolve through low temperature phase transitions, e.g., metal-insulator, charge-ordering, ferromagnetic-paramagnetic.

1. 3 Scope of this thesis

In the course of this thesis, I performed the first time-resolved spectroscopic measurements on two distinct, but related compounds, whose common feature is that they all belong to the class of strongly correlated electron systems:

Charge density wave conductor - The collective CDW excitations in quasi-one dimensional CDW conductors, blue bronze ($\text{K}_{0.3}\text{MoO}_3$) and red bronze ($\text{K}_{0.33}\text{MoO}_3$) are investigated for the first time in the long-wavelength limit for a broad temperature range (from 4 K – 325 K). The transverse phase mode (phason) and amplitude mode (amplitudon) are in different low-frequency regimes. Under weak light illumination (5 mW) of KMO at 30 K the transverse phason exhibits an acoustic-like dispersion

relation in the long-wavelength limit. The dispersion relation of the transverse phase mode is measured in the frequency range from 5 – 40 GHz by time resolved transient reflectivity spectroscopy. In contrast, the amplitude mode exhibits a weak (optic-like) dispersion relation with a frequency $\Omega_+(q = 0) = 1.66$ THz at 30 K. The discussion of the low-energy collective excitations includes the temperature evolution, dispersion relationship and anisotropy of amplitudon and transverse phason.

Colossal magnetoresistance manganites - The first time-resolved spectroscopic data obtained from doped perovskite manganite thin films and single crystals are presented over a wide temperature range. The observed low-energy collective mode is discussed in terms of the opening of a pseudogap and charge/orbital ordering phases. Distinct charges modify the uniformity of the charge density, leading to the development of the CDW condensate, which cooperates with a Jahn-Teller distortion and competes with the electron itinerancy favored by double exchange. Damping of the oscillatory component of the transient reflectivity in the vicinity of the MI transition is discussed with respect to inhomogenous phases. The temperature evolution of a soft-lattice mode provides further information about electronic and structural instability and phase changes. Furthermore, we showed that the quasiparticle dynamics in the vicinity of the metal-insulator transition are strongly affected by the presence of a pseudogap, phase separation and percolation, which are strongly dependent on temperature. A very long-lived relaxation process observed in time-resolved transient reflectivity measurements from doped manganite single crystals and thin films is ascribed to a slow spin relaxation. We also discuss strain-dependent spin dynamics in NSMO near the metal-insulator transition.

1. 4 Outline

In chapter 2, we give a brief theoretical description of the collective modes, photoexcitation and relaxation processes, focusing on the recent work on one-dimensional CDW conductors and CMR manganites. In section 2.1, we first present a model for the initial photoexcited carrier relaxation processes in metallic phase with no contribution from the spin system. Next, we extend the investigation to include electron-spin and spin-lattice interaction. In section 2.2, we briefly review some of the most important properties of the low energy excitation spectrum and collective modes in CDW conductors. Next, we describe the theory for the excitation of amplitudon oscillations in reflectivity or transmission experiments in CDW material referred to as the displacive excitation of coherent modes (DECM). Finally, we describe the mechanism of photo-generation of coherent transverse phasons based on light absorption in two-color pump probe experiments.

In chapter 3, we present the experimental techniques. The descriptions include the three-wave mixing processes, the laser systems, and the experimental setups used for this thesis. In the last part of this chapter, we describe the sample preparation and characterization for 1D CDW and CMR materials.

In chapter 4, we present our first-time time-resolved spectroscopic data obtained from the quasi-one dimensional CDW conductors, $K_{0.3}MoO_3$ and $K_{0.33}MoO_3$, in which collective modes have been studied extensively both theoretically and experimentally. We analyze the data by using the model introduced in chapter 2. This enables us to obtain important information about the low-energy collective excitations, including the temperature evolution, dispersion relationship and anisotropy of amplitudon and phason.

In chapter 5, we present ultrafast time-resolved nonlinear spectroscopic data on doped perovskite manganites. We first give a general introduction to the CMR phenomena, focusing on charge ordering phases and phase separation in LCMO, a prototypical CMR material. In section 5.2, we present the first time-resolved spectroscopic data taken for a LCMO thin film and single crystal, which reveal a strongly damped low-energy collective mode. In section 5.2.4, we discuss quasiparticle dynamics in the vicinity of a metal-insulator transition in terms of small polaron formation and phase separation/percolation. Finally, a very long-lived relaxation component observed in time-resolved transient reflectivity measurements from doped manganites are ascribed to a slow spin relaxation process, which also shows a very strong strain effect in NSMO thin films.

In chapter 6, we give a summary and outlook.

Chapter 2

Theory of time-resolved optical spectroscopy

Recently, femtosecond pump-probe techniques have been applied to the study of various materials. In pump-probe experiments on a number of conducting or semiconducting materials, besides the relaxation processes, oscillations have been observed in reflectivity (or transmission through thin samples) with frequencies that correspond to acoustic and optical phonon modes, as well as, amplitudon and phason [27-31]. A number of mechanisms have been proposed to explain the relaxation and oscillation processes in semiconductors and metallic phases, including Allen's model, the displacive excitation of coherent phonons (DECP), impulsive stimulated Raman scattering (ISRS), and the propagation of acoustic longitudinal stress pulses [27-32]. In this chapter, we briefly review some of the most important properties of these mechanisms, focusing on reflectivity changes in a low energy excitation spectrum associated with different phases. First, we consider the energy transfer following photoexcitation between three subsystems: the electron gas, the spin system, and the

lattice. We present a model for the initial photoexcited carrier relaxation processes in the metallic phase with no contribution from the spin system [32]. The model predicts that the thermal relaxation of electrons in metals is determined by the electron-phonon relaxation time, which is proportional to the average electron-phonon coupling constant, λ , a very important parameter in the theory of strongly correlated systems. Next, we extend the investigation to time-resolved pump-probe studies with electron-spin and spin-lattice interaction. Further, we describe the theory for the excitation and detection of amplitudon oscillations in transient reflectivity or transmission experiments from CDW conductors. In the last section, we focus on the photo-generation mechanism of coherent phasons based on light absorption in two-color pump probe experiments. According to the model, the dispersion of the long-wavelength phasons can be measured by changing the probe wavelength. The model is sufficiently general to treat low-energy collective mode excitations in colossal magnetoresistance materials as well as charge-density wave conductors.

2. 1 Photoexcited carrier relaxation

The material response to a high-intensity ultrashort photoexcitation can be treated by considering the energy transfer between three subsystems: the electron gas at temperature T_e , the spin system at temperature T_s , and the lattice at temperature T_l . The dynamics of the whole system is governed by the internal relaxation of each subsystem and its interaction and energy exchange with the others. The temporal evolution of the system is phenomenologically described by coupled differential equations [33-35]:

$$C_e(T_e) \frac{dT_e}{dt} = -G_{el}(T_e - T_l) - G_{es}(T_e - T_s) + P(t) \quad (1)$$

$$C_l(T_l) \frac{dT_l}{dt} = G_{el}(T_e - T_l) + G_{sl}(T_s - T_l) - \kappa \nabla^2 T_l \quad (2)$$

$$C_s(T_s) \frac{dT_s}{dt} = G_{es}(T_e - T_s) - G_{sl}(T_s - T_l) \quad (3)$$

where $\kappa \nabla^2 T_l$ represents lattice thermal conductivity losses; C_e , C_s , and C_l are the electronic, spin, and lattice contribution to the specific heat, respectively; G_{el} , G_{es} , and G_{sl} are parameters describing the electron-lattice, electron-spin, and spin-lattice energy transfer rates among the three subsystems. Heat conduction through phonons should dominate the electronic heat conduction, given the rather large electrical resistivity in correlated systems (even in metallic state), according to Wiedemann-Franz law. The laser term $P(t)$ is applied to the electronic system since the initial heating process occurs only in the electron bath.

First, we discuss a model for the initial photoexcited carrier relaxation processes in a metallic phase with no contribution from the spin system.

2. 1. 1 Coupled electron lattice systems

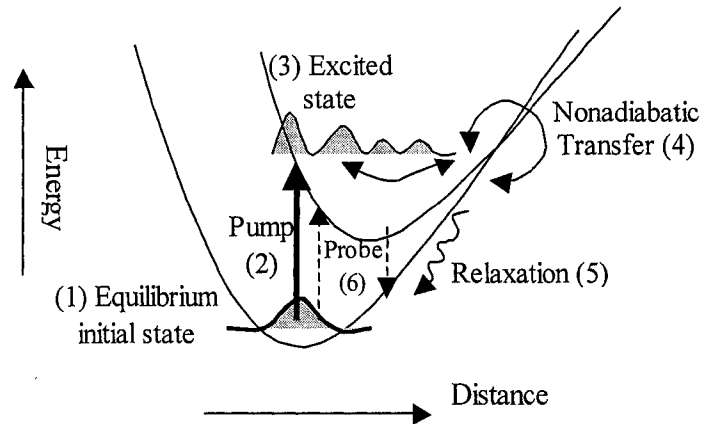


Figure 3. An excitation-deexcitation cycle. Details see text.

As shown in Fig. 3, an initial correlated state (1) is partially promoted to the excited electronic state by the pump pulse (2), leaving a ‘‘hole’’ in the ground state density. The excited state population moves to the crossing point (3) where it can cross back to the ground state potential via a nonadiabatic transition (4). Once on the ground electronic potential surface the hot vibration cools back to the bottom of the well (5). The dynamics is followed in time by a short - weak probe pulse (6). The electron-electron thermalization time $\tau_{e-e} \sim \frac{\hbar E_F}{2\pi E^2}$ [36], where E is the carrier energy measured from the Fermi energy E_F , is of the order of several femtoseconds. We can assume the process to be instantaneous since τ_{e-e} is fast compared to the pulse duration. As τ_{e-e} is much faster than the period of a typical phonon vibration, electrons are decoupled from the lattice, and the electronic system can be described with the electronic temperature T_e which differs from the lattice temperature T_l . Because the heat capacity of the electron gas is much smaller than the heat capacity of the lattice, T_e can be much higher than T_l . In experiments performed with high photoexcitation density pulses T_e can reach several hundred or even thousand degrees K above T_l .

By measuring the temporal dependence of the reflectivity change on the picosecond timescale we can experimentally determine the relaxation time of the photoexcited electronic system. In general two effects should be considered: first, the energy relaxation due to electron-electron scattering and scattering with other excitations (phonons, plasmons, etc.), and second, the transport of energy out of the probed volume.

Energy relaxation through electron-phonon scattering was theoretically investigated by Allen in 1987 motivated by experimental data [32]. Dr. Allen

followed the model of Kaganov et al. [37] considering the system of electrons and phonons with thermal distribution functions f_k and n_Q determined by T_e and T_l , respectively. Furthermore, he assumed that i) diffusion driven by spatial inhomogeneities is negligible, which is a good approximation in the case where the mean free path is short, ii) acceleration due to external or internal fields is negligible, and iii) no other collision processes are important. The collision integrals describing the time development of f_k and n_Q can be approximated by

$$\frac{\partial f_k}{\partial t} = -\frac{2\pi}{\hbar N_c} \sum_Q |M_{kk'}|^2 \{ f_k (1 - f_{k'}) [(n_Q + 1) \delta(\varepsilon_k - \varepsilon_{k'} - \hbar\omega_Q) + n_Q \delta(\varepsilon_k - \varepsilon_{k'} + \hbar\omega_Q)] \\ - (1 - f_k) f_{k'} [(n_Q + 1) \delta(\varepsilon_k - \varepsilon_{k'} + \hbar\omega_Q) + n_Q \delta(\varepsilon_k - \varepsilon_{k'} - \hbar\omega_Q)] \} \quad (4)$$

$$\frac{\partial n_Q}{\partial t} = -\frac{4\pi}{\hbar N_c} \sum_k |M_{kk'}|^2 f_k (1 - f_{k'}) [n_Q \delta(\varepsilon_k - \varepsilon_{k'} + \hbar\omega_Q) - (n_Q + 1) \delta(\varepsilon_k - \varepsilon_{k'} - \hbar\omega_Q)] \quad (5)$$

where k and Q are the electron and phonon wave vectors, respectively, N_c is the number of unit cells in the sample and $M_{kk'}$ is the electron-phonon matrix element normalized to the unit cell of magnitude $(E_F \hbar\omega_D)^{1/2}$. The additional factor 2 in the second equation accounts for electron spin degeneracy. In this model, Allen considered other collision processes - electron-electron (e-e) and phonon-phonon (ph-ph) scattering - being active in keeping the distributions f_k and n_Q equal to local equilibrium distributions characterized by T_e and T_l , which depend on time. In the case where the geometry of the experiment prevents electron transport out of the probed volume or the electron mean free path is short in comparison with the optical skin depth, the e-e and ph-ph collision integrals are equal to zero. If f_k and n_Q are known at $t = 0$, and the above assumptions stand, then the equations determine their temporal evolution. Dr. Allen calculated the rate of energy exchange by taking into

account that $E_L \sim 3N_c k_B T_l$, since most of the experiments were performed at room temperature and $E_L \sim E_0 + \gamma T_e^2 / 2$, where $\gamma = \pi^2 N_c N_0 k_B^2 / 3$ (N_0 is the density of state of both spins per unit cell). A simple expression for the rate of change of the electronic temperature was derived

$$\frac{\partial T_e}{\partial t} = \gamma_T (T_l - T_e); \quad \gamma_T = \frac{3\hbar\lambda\langle\omega^2\rangle}{\pi k_B T_e} \left(1 - \frac{\hbar^2\langle\omega^4\rangle}{12\langle\omega^2\rangle k_B^2 T_e T_l} + \dots \right) \quad (6)$$

where $\lambda\langle\omega^n\rangle = 2 \int_0^\infty [\alpha^2 F(\Omega) / \Omega] \Omega^n d\Omega$ and $\alpha^2 F(\Omega)$ is the product of the electron phonon coupling strength α^2 , and the phonon density of states $F(\Omega)$, both functions of energy. From Eq. (6), Allen was able to extract the values of the average electron-phonon coupling constant using experimental data from Au [38], Cu [39] and W [40]. The obtained values are in very good agreement with the λ extracted from resistivity [41] and neutron scattering data [42]. In the following years several measurements of λ -s of various metals exhibiting superconductivity at low temperatures were carried out by a group at MIT [43-44], always in very good agreement with the data obtained by other techniques. This group also performed the pump-intensity dependence measurements again in excellent agreement with Allen's model. The average electron-phonon coupling constant, λ , is a very important parameter in the theory of strongly correlated systems, because the coupling parameter reflects the two-way competition more directly than temperature and measures the strength with which valence electrons interact with the crystal lattice. Recently, the decrease of the electron-phonon coupling constant has been used to explain the spectral weight transfer of doped manganites including the increase of the lower band width in the ferromagnetic metallic state [43-45].

2. 1. 2 Correlated spin systems

Besides the interactions between the electrons and lattice, the coupling of electron-spin and spin-lattice degrees of freedom is also very important to describe the physics of strongly correlated systems. For example, the response of a magnetic material following photoexcitation can be treated by considering the energy transfer between the three subsystems: the electron gas at temperature T_e , the spin system at temperature T_s , and the lattice at temperature T_l . The dynamics of the whole system is governed by the internal relaxation of each subsystem and its interaction and energy exchange with the others. The temporal evolution of the system is phenomenologically described by Eqs. (1) - (3) [33-35].

Within the dipole approximation, optical transitions preserve the electronic spins, $\Delta S = 0$, such that the spin polarization of the excited electronic distribution is the same as in the ground state. According to Eqs. (1) - (3), the onset of demagnetization, and dynamic spectral weight transfer (DSWT), is governed by the electronic, lattice, and magnetic contributions to the specific heat, the energy exchange rates G_{ij} , and their temperature dependence. The absorption change due to DSWT can be expressed as:

$$\Delta A_{DSWT} = \Delta A_{DSWT_e}(\omega_{pump}; \omega_{probe}, t, T) + \Delta A_{DSWT_l}(\omega_{pump}; \omega_{probe}, T) \times [1 - \exp(-t/\tau_{sl})]. \quad (7)$$

The first term represents the demagnetization due to electronic-spin interaction, whereas the second term represents the dynamics governed by the slow lattice-spin thermalization and its lattice-spin interaction time constant.

Based on the principle of causality, the Kramers-Kronig transformation states that a change in the absorption coefficient (ΔA) throughout the spectrum Ω [45] leads to a change in the index of refraction:

$$\Delta n(\omega_{pump}; \omega_{probe}) = \frac{2}{\pi} \int_0^{\infty} \frac{\Omega \Delta A(\omega_{pump}; \Omega)}{\Omega^2 - \omega_{probe}^2} d\Omega. \quad (8)$$

For the colossal magnetoresistance material $\text{La}_{0.7}\text{Ca}_{0.3}\text{MnO}_3$ (LCMO), given the electronic heat capacity coefficient, $\gamma \sim 5 \text{ mJ/mol.K}^2$ [46-47] and a deposited energy density $E \sim 0.25 \text{ } \mu\text{J/cm}^2$ typical in pump-probe experiments, the initial electronic temperature heating at T_C can be estimated as $\Delta T_e \sim 65 \text{ K}$. Electron-lattice energy exchange occur on a picosecond time scale through the strong electron-phonon coupling. The lattice with its larger specific heat (Debye temperature $\theta_D \sim 450 \text{ K}$), $C_l \sim 110 \text{ J/mol.K}$ [48-49], acquires an excess temperature of $\Delta T_l \sim 0.6 \text{ K}$ at T_C . The measured temperature-dependent time constants vary from $\sim 110 \text{ ps}$ at 260 K to 20 ps below 50 K which is in good agreement with the model expected with a weak spin-orbital coupling [33].

2. 2 Photoexcited collective modes

In this section, we discuss the mechanisms for photo-excitation of low energy collective modes in the well-known CDW system $\text{K}_{0.3}\text{MoO}_3$, and doped manganites $\text{La}_{1-x}\text{Ca}_x\text{MnO}_3$. As expected for a complex order parameter, $|\Delta|e^{i\phi}$, both phase and amplitude excitations occur. In first approximation, the modes are decoupled and represent independent oscillations of the amplitude and phase of the order parameter [14]. First, we discuss the amplitudon oscillations based on the model of displacive excitation of coherent phonons (DECP), where only A_1 symmetry Raman-active modes are observed.

2. 2. 1 Amplitudon oscillations

A charge-density wave is a modulation of the conduction electron density in a metal and an associated modulation of the lattice atom positions¹. The collective modes are formed by electron-hole pairs, involving the wave vector $2k_F$, when electrons and holes on the opposite side of the Fermi surface are coupled, referred to as “Fermi nesting”. This leads to the formation of CDW and the accompanying lattice distortion. In quasi-one-dimensional metals at low temperatures, the elastic energy cost to modulate the atomic positions is less than the gain in conduction electron energy, so the CDW state is the preferred ground state. At high temperatures, the electronic energy gain is reduced by thermal excitation of electrons across the gap, so the metallic state is stable. The second-order phase transition that occurs between the metallic and charge-density wave states is known as the Peierls transition [50]. The CDW develops along the chain direction. The CDW state is characterized by a complex order parameter $\psi = \Delta e^{i\phi}$. The amplitude Δ determines the size of the electronic energy gap and the magnitude of the atomic displacements. The phase

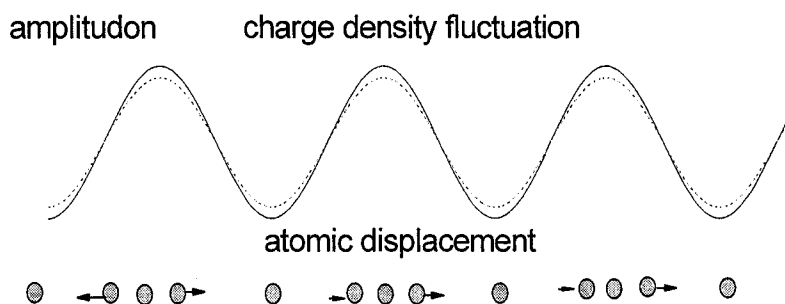


Figure 4. A schematic of amplitudon excitation in 1D CDW.

¹ A detailed description of the CDW phenomenon and mechanism is given in the recent book by Grüner [24]

ϕ determines the position of the CDW relative to the underlying lattice. Variations of ϕ and Δ can arise from collective modes known as phasons and amplitudons, respectively.

The modulation of the amplitude Δ changes the condensation energy and has therefore a finite frequency. As shown in Fig. 4, fluctuations of the single particle gap in charge density wave materials also lead to fluctuations of the ionic positions. The amplitude mode oscillation energy is substantially lower than the gap energy [14].

Temperature dependences of amplitude mode frequencies and damping were studied experimentally in KMO by Raman scattering [51] and neutron spectroscopy [52]. At temperatures close to zero, the amplitudon frequency is ~ 1.7 THz. The frequency lowers as T_C^{3D} is approached [51-52], but no drop to zero occurs. This seems to indicate that the amplitude excitations are controlled by the mean-field behavior of the distorted Peierls chain [53]. Neutron data show continuous behavior at T_C^{3D} , meaning that the amplitude mode frequency does not drop abruptly at T_C^{3D} due to a finite coupling to the phase modes [14].

The dispersion relation of the amplitude mode was evaluated first by Lee, Rice, and Anderson using a one-dimensional electron-phonon Hamiltonian [54]. In the long-wavelength limit, the electron-phonon interaction transforms the acoustic phonons near the zone boundary into an optical (Ω_+) and an acoustic branch (Ω_-). The dispersion relation for the optical branch (Ω_+) is obtained for the frequency of the amplitude mode:

$$\Omega_+^2 = \lambda(\omega_{2k_F})^2 + \frac{1}{3} \left(\frac{m}{m^*} \right) (v_F q)^2, \quad (9)$$

where λ is the electron-phonon coupling constant, ω_{2k_F} is the phonon frequency, m^* is the effective mass, v_F is the Fermi velocity, and q is the wave number.

Since for amplitude mode oscillations there is no net displacement of the electronic charge with respect to the ion positions, the mode is expected to be Raman active and of A_1 symmetry (A_1 modes are the so-called "breathing modes", which do not lower the symmetry of the lattice; the A_1 symmetry displacements preserve the symmetry of the actual lattice and have a continuum of possible values; the equilibrium position of A_1 displacements is determined by minimizing the free energy of the system).

Excitation of the amplitude modes depend on the instantaneous surrounding electron density $n(t)$ as shown in Fig. 4, which in turn involves displacements of the ions about their equilibrium positions, Q_0 . By deriving the time dependence of the ionic coordinate $Q(t)$, we can find the displacement of the amplitudons.

In our measurements, the pump pulse produces a time dependent displacive excitation of the charge-density amplitude. The displacement is strongly coupled with vibrations of the ion equilibrium position $Q_0(t)$. Since the typical time of the perturbation of the electronic system τ_i is much shorter than the vibration period of the collective mode $2\pi/\omega_A$, the photoexcitation can be thought of as a $\delta(t)$ – function-like perturbation of the charge density. In turn, the response of the amplitudon to this perturbation is a modulation of the reflectivity $\Delta R_A / R$ of the form: $A(T)e^{-\gamma} \cos(\omega t)$ based on the DECP mechanism [29]. The derivation below assumes the density of occupied states, $n(t)$, as the source of DECP [29].

The time scale to increase $n(t)$ in bands above E_F after photoexcitation is short compared to the equilibration time of the ionic system. The instantaneous change of $n(t)$ leads to a change in the quasi-equilibrium A_1 ionic coordinate and thereby coherently exciting A_1 vibrational modes.

The equation describing the rate of change of $n(t)$ in the sample is:

$$\frac{dn(t)}{dt} = \rho P(t) - \beta n(t) \quad (10)$$

The first term on the right-hand side is the rate of carrier generation in the excited band, which is assumed to be proportional to the pump pulse temporal profile: $P(t) = E_{pump} g(t)$ is the energy in the excitation pulse arriving per unit area per unit time at the surface and ρ is the proportionality constant. The second term is the transfer rate of electrons back to the ground state. The source of excitation of the A_1 mode is the dependence of the equilibrium A_1 coordinate $Q_0(t)$ on $n(t)$. We take this dependence to be linear: $Q_0(t) = \kappa n(t)$.

The equation governing the time dependence of the coordinate $Q(t)$ is then:

$$\frac{d^2 Q(t)}{dt^2} = -\omega_0^2 [Q(t) - Q_0(t)] - 2\gamma \frac{dQ(t)}{dt}, \quad (11)$$

Here ω_0 is the angular frequency of the A_1 mode, and γ represents the damping constant of the modes.

Assuming that the excitation from the pump pulse is short compared to the A_1 phonon oscillation cycle, we can approximate the normalized pulse shape function, $g(t)$ with a δ -function giving the exponential time dependence of $n_p(t) \propto e^{-\beta t}$. Then the time dependence of the coordinate $Q(t)$ is given by:

$$Q(t) = \frac{\omega_0^2 \kappa \rho E_{pump}}{(\omega_0^2 + \beta^2 - 2\beta\gamma)} [e^{-\beta t} - e^{-\gamma t} (\cos(\omega t) - \frac{\beta - \gamma}{\omega} \sin(\omega t))]. \quad (12)$$

where $\omega = \sqrt{\omega_0^2 - \gamma^2}$. The reflectivity R is a function of the complex dielectric constant, which is in turn modulated by n , T_e , and Q . If $R(0)$ is the unperturbed reflectivity before the arrival of the pump pulse, then the differential reflectivity change, $\Delta R(t)$, due to the photoexcitation can be written as:

$$\frac{\Delta R(t)}{R(0)} = \frac{1}{R(0)} \left[\frac{\partial R}{\partial n} n(t) + \frac{\partial R}{\partial T_e} \Delta T_e(t) + \frac{\partial R}{\partial Q} Q(t) \right]. \quad (13)$$

By writing the reflectivity in terms of complex dielectric function and approximating the sufficiently narrow pump and probe pulses as δ -function, we obtain the time dependence of the photoinduced reflectivity

$$\frac{\Delta R(t)}{R(0)} = A e^{-\beta t} + B \frac{\omega_0^2}{(\omega_0^2 + \beta^2 - 2\beta\gamma)} \left[e^{-\beta t} - e^{-\gamma t} (\cos(\omega t) - \frac{\beta - \gamma}{\omega} \sin(\omega t)) \right] \quad (14)$$

with

$$A = \frac{1}{R} \left[\left(\frac{\partial R}{\partial \varepsilon_1} \right) \left(\frac{\partial \varepsilon_1}{\partial n} \right) + \left(\frac{\partial R}{\partial \varepsilon_2} \right) \left(\frac{\partial \varepsilon_2}{\partial n} \right) \right] \rho \varepsilon_{pump}$$

and

$$B = \frac{1}{R} \left[\left(\frac{\partial R}{\partial \varepsilon_1} \right) \left(\frac{\partial \varepsilon_1}{\partial Q} \right) + \left(\frac{\partial R}{\partial \varepsilon_2} \right) \left(\frac{\partial \varepsilon_2}{\partial Q} \right) \right] \kappa \rho \varepsilon_{pump}.$$

The fit to the differential reflectivity taken at low temperatures on 1D charge density wave insulator $K_{0.3}MoO_3$ and 2D charge density wave insulator 1T-TaS₂ using Eq. (14) gives an excellent agreement with the theory [55-56].

In DECP the oscillations in transient reflectivity $\Delta R(t)$ are excited with a $\cos(\omega t)$ dependence, where $t = 0$ is the time of arrival of the probe pulse. The phase shifts from a simple $\cos(\omega t)$ were found to be rather small, since ω_0 is usually an order of magnitude larger than β and γ . An important prediction of DECP model is also the linear dependence of the oscillatory amplitude on the pump pulse integrated intensity that has also been experimentally confirmed [55-56]. The main difference between DECP and ISRS or other nonlinear impulsive excitation mechanisms is that in case of DECP the A_1 symmetry modes should be the only ones observed [29].

2. 2. 2 Phason oscillations

Besides the amplitude mode, other important collective excitations in quasi-one dimensional CDW systems are the phase modes (phasons). Phasons are the linear excitations of the order parameter: phase ϕ in CDW systems. The phase displacement can be parallel or perpendicular to the direction of the CDW. The former represents a longitudinal phase mode (Fig. 5a)), the latter a transverse phase mode (Fig. 5b)).

At long wavelengths, the longitudinal phasons are subjected to quasi-particle excitation and Coulomb forces. Lee, Rice, and Anderson pointed out that Coulomb interaction will raise the longitudinal phason frequency to a longitudinal optic (LO)

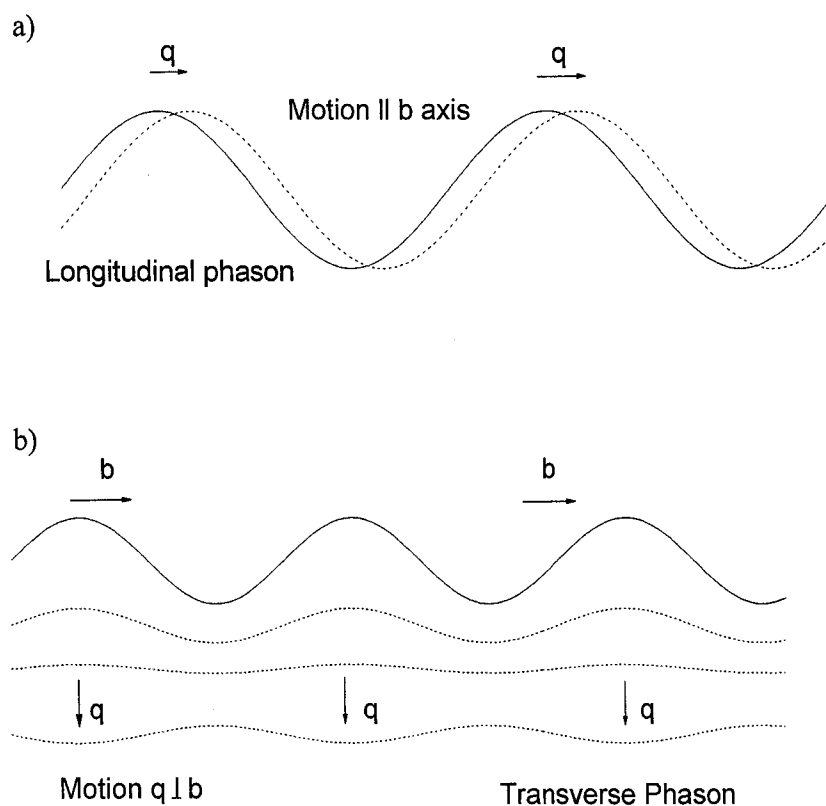


Figure 5. a) A schematic of longitudinal phason excitation in 1D CDW; b) A schematic of transverse phason excitation in 1D CDW.

frequency at zero temperature and the CDW becomes rigid due to pinning at impurity sites [54].

Recently, Viroztek and Maki applied a thermal Green's function theory to calculate the dispersion relations of the collective CDW modes taking into account long-range Coulomb interaction and quasi-particle screening [57]. The longitudinal phase mode (as shown in Fig. 5a)) exhibits a linear acoustic-like dispersion for wavevectors q less than the Thomas-Fermi screening wavevector q_0 and becomes an optic-like mode with an energy gap when no screening occurs, i.e., $q > q_0$ [14]:

$$\begin{aligned}\Omega_{L-}^2 &= \frac{(c_0 q)^2}{1 - f_s}, & q \ll q_0 \\ \Omega_{L-}^2 &= \frac{3}{2} \lambda \omega_{2k_F}^2 f_s + c_0^2 q^2, & q \gg q_0,\end{aligned}\quad (15)$$

where the phase velocity, $c_0 = (m/m^*)^{1/2} v_F$, q is the wave number, f_s is the static condensate density ($f_s \leq 1$) and $q_0 = \omega_p v_F^{-1} (1 - f_s)^{1/2}$ with ω_p the plasma frequency. The dispersion relation of the longitudinal phase mode provides a sensitive probe for the screening of Coulomb interaction by quasi-particles and the depinning of the CDW modes. When Coulomb forces are screened by quasi-particles excited above the Peierls gap, the collective motion is compensated by the quasi-particle current and the longitudinal phase mode remains acoustic [14].

In contrast, the transverse phase modes (as shown in Fig. 5b)) are unaffected by Coulomb interaction. In this case, the following dispersion relation is obtained for the frequency of transverse phase mode (Ω) [14]:

$$\Omega_{T-}^2 = (c_0 q)^2. \quad (16)$$

Below, we describe quantitatively the process in which a low-energy transverse phason wave packet is generated and detected by nonlinear time-resolved

spectroscopic measurements [26]. The phason oscillations cause a change in dielectric constant, $\Delta\epsilon$, which results in a modulation of $\Delta R(t)$. The basic idea is depicted in Fig. 6.

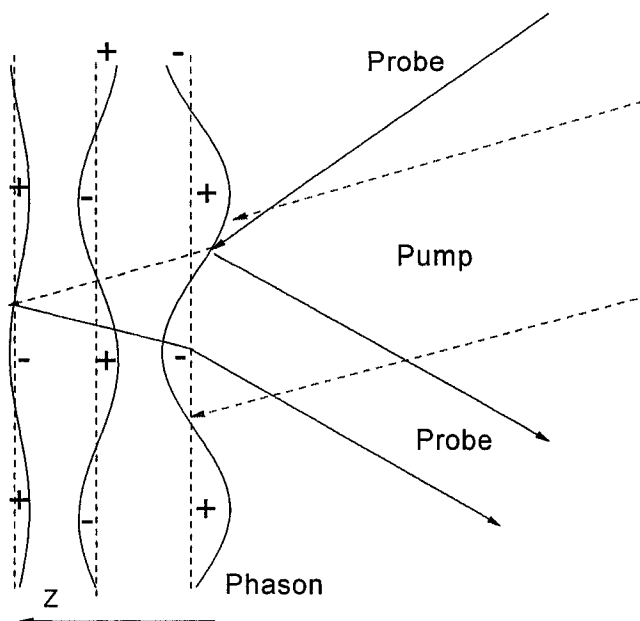


Figure 6. Schematic diagram of phason excitation and detection.

The pump light passes through a CDW crystal and is absorbed in the top layers. The heated charge carriers expand and generate a disturbance of the CDW. The charge density excitation will propagate away from the surface into the material. In this way, the transverse phasons are excited and propagate normal to the surface. We use a time-delayed probe light pulse to detect the frequency spectrum of the charge density fluctuation. Part of the probe light pulse is reflected by the wave front of the charge-density fluctuations, and the remainder at the surface of the CDW single

crystal. These reflections interfere constructively or destructively depending on the position and time of the CDW excitation.

Since the penetration depth, ξ , of the light is small compared to the laser spot size (~ 2 mm for our case) on the sample, a one-dimensional treatment of the propagation of the CDW is acceptable [27, 58]. The CDW amplitude at distance z from the surface is denoted $D(z,t)$. The reflectivity undergoes a change ΔR because the optical constants of the crystal are changed by the propagating CDW:

$$\Delta n(z,t) = \frac{\partial n}{\partial D} D(z,t) \approx \alpha D(z,t), \quad (17)$$

where α is a constant in first approximation. The complex amplitude of the probe pulse reflected from the CDW will be:

$$E_{pr} = E_0 \alpha \int_0^z D(z,t) \exp(-2ikz \cos \theta) dz, \quad (18)$$

where k is the wave number of the light in the material, θ is the angle between the wave vector of the probe pulse and the surface normal, and E_0 is the amplitude of the probe pulse. If the reflection coefficient at the surface of the film is r_0 , then the effective reflection coefficient, allowing for interference, is:

$$R(t) = \left| r_0 + a \int_0^z D(z,t) \exp(-2ikz \cos \theta) dz \right|^2. \quad (19)$$

To first order approximation in $D(z,t)$, the time-dependent part of $R(t)$ is:

$$\Delta R(t) = r_0^* a \int_0^z D(z,t) \exp(-2ikz \cos \theta) dz + c.c. \quad (20)$$

We can express the CDW excitations in terms of its Fourier components D_q :

$$D(z,t) = \int_0^\infty dq D_q \exp[i(qz - \omega_q t)] \exp(-\gamma_q t) \quad (21)$$

where ω_q and γ_q are the frequency and damping of the phason with wave vector q in the z -direction. Inserting Eq. (21) into Eq. (20) yields

$$\Delta R(t) = 2\pi\omega_0^* a D_K \exp(-i\omega_K t) \exp(-\lambda_K t) + c.c. \quad (22)$$

with $K = 2k \cos \theta$ (phase matching condition).

We see from Eq. (22) that $\Delta R(t)$ should be an oscillatory function of the time delay Δt of the probe beam relative to the pump beam. The model is in excellent agreement with our recent measurements in blue bronze ($\text{K}_{0.3}\text{MoO}_3$) and red bronze ($\text{K}_{0.33}\text{MoO}_3$) single crystals and doped manganite (e.g. $\text{La}_{0.67}\text{Ca}_{0.33}\text{MnO}_3$) thin films [26, 59]. Such oscillations generally occur provided that (i) the CDW crystal is strongly absorbing, i.e., $\xi \leq \lambda/n\cos\theta$, (ii) $\Delta t \leq 2\tau_B$ (Δt being the optical pulse duration and τ_B is the oscillation period in ΔR), (iii) α is large enough for the oscillations to be resolved, and (iv) there is coherent overlap between the optical reflections.

An important feature of the result is that for a specific probe wavelength $\Delta R(t)$ only involves one particular Fourier component D_K of the excited CDW oscillation. The frequency of the oscillations is the frequency of a transverse phason with wavenumber K , and the damping of the oscillations is the damping of the same phason. Thus, from a measurement of $\Delta R(t)$ one can deduce the phase velocity and damping rate of phasons of a defined frequency in the Brillouin range.

The only requirement is that the Fourier component D_K is large enough to give measurable oscillations in $\Delta R(t)$. The duration of CDW propagation in the sample is of order ξ/v with phase velocity v , which is typically a few picoseconds (~ 10 ps in $\text{K}_{0.3}\text{MoO}_3$ and $\text{K}_{0.33}\text{MoO}_3$). So the actual duration Δt of the optical pulse has little influence provided that $\Delta t < \xi/v$. The temporal Fourier transform of the CDW

excitation in the material is proportional to $\frac{1}{(\nu/\xi) + i\omega}$. This corresponds to a broad spectrum down to frequencies of order ν/ξ (~ 10 GHz for $\text{K}_{0.3}\text{MoO}_3$ and $\text{K}_{0.33}\text{MoO}_3$). The coherent modes across a range of wave vectors near the Brillouin zone center are excited and peaked at a wave vector of order one inverse laser penetration depth. The penetration depth of the light (~ 100 nm) is small compared to the laser spot size (~ 2 mm) on the sample, and therefore modes with a wavevector normal to the surface are predominantly excited.

Chapter 3

Experimental details

In section 3.1, we describe the experimental methods of infrared-pulse generation, the light sources, and two slightly different pump-probe setups used for the experiments in this thesis. In section 3.2, we present some details on preparation and sample characterization of CMR manganites and CDW conductors.

3. 1 Femtosecond time-resolved optical spectroscopy

The development of femtosecond laser systems has opened the door for studying ultrafast dynamical processes, which range from nuclear motion in molecules to relaxation mechanisms of charge carriers in solids. A characteristic of the approach is that the system investigated is no longer in thermodynamic equilibrium. It is rather in an excited state whose decay into electronic-, spin-, and lattice- degrees of freedom is being probed. In this section, we present the experimental methods, setups, the light sources and the detection systems used for our nonlinear time-resolved experiments in this thesis.

3. 1. 1 Three-wave mixing processes as an infrared source

Three-wave mixing is a versatile method for generating short and tunable pulses at wavelengths ranging from ultraviolet (> 200 nm) to mid-infrared (up to $20 \mu\text{m}$). Examples of three-wave mixing are sum-frequency generation (SFG), second-harmonic generation (SHG), difference-frequency generation (DFG), and optical parametric generation and amplification (OPG and OPA). These techniques are now standard practice in time-resolved spectroscopy [60-62]. In these processes, oscillating electrical fields at two or three different frequencies are coupled to each other.

For OPA wavelength conversion used in this thesis, we employed a specially designed crystal, β -barium borate (BBO). This crystal has, due to its crystal symmetry (or the absence thereof), both a nonzero $\chi^{(2)}$ and a strong birefringence, which we utilize for phase-matching. In general, the phase-matching can be of 'type 1' (pump polarization is perpendicular to both signal and idler), 'type 2' (pump and idler polarizations are perpendicular to the signal), or 'type 3' (pump and signal polarizations are perpendicular to idler). The infrared pulses used for the time-resolved experiments presented in this thesis are all generated by OPA processes.

In general, the dielectric polarization $P(t)$ at time t in a medium can be written as a power series in the electrical field:

$$P(t) \propto \chi^{(1)}E(t) + \chi^{(2)}E^2(t) + \chi^{(3)}E^3(t) + \dots \quad (23)$$

Here, the coefficients $\chi^{(n)}$ are the n -th order susceptibilities of the medium. For any three-wave mixing process, the second-order term is crucial; it is only nonzero in media that have a broken inversion symmetry. If we write

$$E(t) = E_1 e^{i\omega_1 t} + E_2 e^{i\omega_2 t} + c.c., \quad (24)$$

where *c.c.* denotes the complex conjugate, the second-order term in Eq. (1) will read

$$P^{(2)}(t) \propto \sum \chi^{(2)} n_0 E_1^{n_1} E_2^{n_2} e^{i(m_1\omega_1+m_2\omega_2)t} + c.c., \quad (25)$$

where the summation is over $(n_0, n_1, n_2, m_1, m_2) = (1, 2, 0, 2, 0), (1, 0, 2, 0, 2), (2, 2, 0, 0, 0), (2, 0, 2, 0, 0), (2, 1, 1, 1, -1), (2, 1, 1, 1, 1)$. The six combinations (n_x, m_x) correspond, respectively, to the second harmonic of E_1 , the second harmonic of E_2 , the optically rectified signals of E_1 and E_2 , the difference frequency, and the sum frequency. A medium that is pumped by the fields E_1 and E_2 will radiate a field E_3 with an angular frequency $\omega_3 = m_1\omega_1 + m_2\omega_2$.

In a typical situation, we have to consider the position dependence of the electrical fields. The electrical fields are traveling waves with an electric field

$$E_j(x, t) = e^{i(\omega_j t - k_j x)}, \quad (26)$$

at position x , with the wave vector $k_j = n(\omega_j)\omega_j / c$, where c is the velocity of light and $n(\omega_j)$ is the index of refraction of the medium at angular frequency ω_j . Thus, the second-order polarization angular frequency ω_3 is:

$$P^{(2)}(x, t) \propto \sum E_1^{n_1} E_2^{n_2} e^{i(\omega_3 t - (m_1 k_1 + m_2 k_2) \cdot x)}. \quad (27)$$

At each position x , the oscillating second-order polarization radiates at angular frequency ω_3 and a corresponding wave vector $k_3 = n(\omega_3)\omega_3 / c$. Constructive interference, and therefore a high intensity ω_3 field, will occur only if

$$k_3 = m_1 k_1 + m_2 k_2. \quad (28)$$

This is known as the *phase matching condition*. Typically, three-wave mixing is done in a birefringent crystalline material (i.e., the index of refraction depends on the polarization and direction of the light that passes through), where the polarizations of the fields and the orientation of the crystal are chosen such that the phase-matching condition is fulfilled.

Optical parametric amplification is a special case of difference frequency generation ($\omega_3 = \omega_1 - \omega_2$) where the pump field amplitude E_1 is much larger than E_2 . The field E_3 that is generated causes E_2 to increase by the simultaneous DFG process ($\omega_2 = \omega_1 - \omega_3$). Because phase matching for the generation of ω_3 implies phase matching for the generation of ω_2 , light at frequencies ω_2 and ω_3 is generated simultaneously. The latter means that in OPA, a photon at frequency ω_1 is 'split' into two photons at frequencies ω_2 and ω_3 . The two fields at frequencies ω_2 and ω_3 are usually referred to as signal (the one with the higher frequency) and idler (the lower frequency), and the field at ω_1 is called the pump (not to be confused with the term 'pump' in a pump-probe experiment). Parametric generation (OPG) is the limiting case where, initially, $E_2 = E_3 = 0$. Though Eq. (39) suggests that second-order polarizations at neither ω_2 nor ω_3 would be generated, the latter does happen in reality, because of quantum-mechanical properties of the electric field.

3. 1. 2 Pulse generation for pump-probe experiments

The essential components of femtosecond time-resolved optical systems are very stable pulsed lasers. In the experiments performed in our laboratory, we use three combined subpicosecond laser systems, including a Ti:sapphire oscillator (Tsunami, Spectra-Physics), a Ti:sapphire regenerative amplifier (Spitfire, Spectra-Physics) and an optical parametric amplifier (OPA-800C, Spectra-Physics). The pulses with 150-fs duration are tunable in wavelength from 400 nm to 10 μm .

Mode-locked Ti:sapphire oscillator

A schematic of the mode-locked Ti:sapphire laser (Tsunami, Spectra-Physics) is shown in Fig. 7 [63]. The Ti:sapphire crystal is pumped through a pump beam

steering mirror (P_1) and a pump beam focus mirror (P_2) by a continuous wave Nd:YAG laser (Millennia V, Spectra-Physics) with an output power of 5 W at a wavelength of 532 nm.

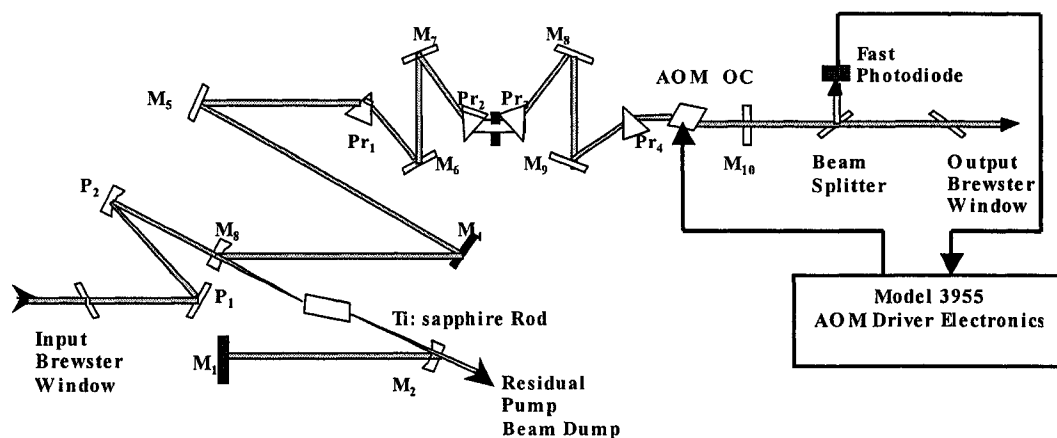


Figure 7. Configuration of the mode-locked Ti:sapphire laser (Tsunami, Spectra-Physics).

The cavity beam is centered and focused in the Ti:sapphire rod by cavity focus mirrors (M_2 and M_3). The cavity fold mirrors (M_4 and M_5) fold the beam and allow the laser to run in a mode-locked mode at convenient repetition frequencies near 80 MHz. The prisms (Pr_1 and Pr_4) in conjunction with the prisms, Pr_2 and Pr_3 , compensate for positive group velocity dispersion (GVD) in the cavity. The tuning slit is used to adjust the laser wavelength and the output pulse bandwidth. The prism mirrors (M_6 through M_9) direct the cavity beam from M_5 through the prisms and into the acoustic-optic modulator (AOM). The AOM is driven by an RF electronics module to provide proper pulsing at start-up. At the cavity end, the high reflector, M_1 , reflects all laser light back into the cavity whereas the output coupler, M_{10} , another cavity end mirror, allows a small percentage ($< 5\%$) to pass through as the output

beam. At the output (~ 800 nm wavelength), an additional beam splitter reflects a small amount of the beam to a silicon diode detector. The fast silicon diode is used for monitoring the pulsed/CW operation.

The critical alignment of the laser system includes pumping and mode-locking optimization. First, the pump illumination in the oscillator must be collinear with the cavity mode over a relatively long length of the laser rod. The pump light is focused to a narrow line within the rod and the oscillating laser mode is similarly focused and overlapped within the same volume - known as longitudinal pumping. The second procedure is the mode-locking optimization. It includes dispersion compensation control (pulse width) and output power. First, one adjusts the prism dispersion until the spectrum increases in bandwidth when more prism glass is inserted into the beam. Then one optimizes the Tsunami output power. A power meter is placed in the Tsunami beam path and mirrors M_1 and M_{10} are adjusted for maximum output power with the procedure: first vertical (blue) button then horizontal (green) button. The pump power and dispersion compensation can be varied to obtain the desired output power and pulse width. The optimization procedure can be performed with the help of a spectrum analyzer and an auto-correlator.

Regenerative Ti:sapphire amplifier

Figure 8 shows the configuration of our regenerative Ti:sapphire amplifier system (Spitfire, Spectra-Physics) [64]. The seed pulse from the Ti:sapphire oscillator (Tsunami, Spectra-Physics) goes through a Faraday isolator (optical diode), which prevents pulses from traveling back into the oscillator, and a pockels cell, which is used as a gate allowing a single pulse to enter the amplifier cavity. This pulse then makes several passes through the Ti:sapphire crystal, which is pumped by a Q-

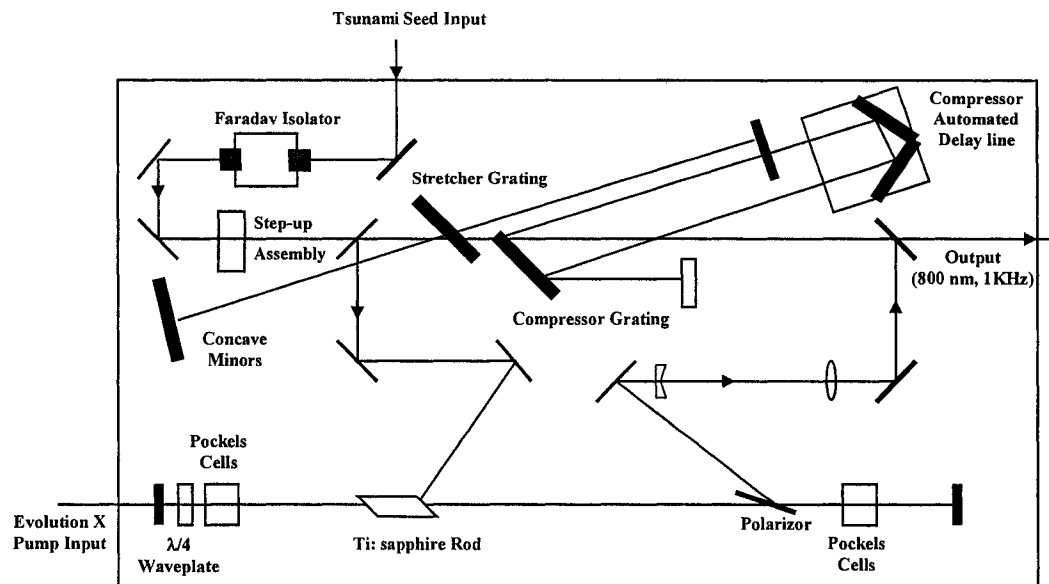


Figure 8. A Schematic of the regenerative Ti:sapphire amplifier system (Spitfire, Spectra-Physics).

switched, frequency-doubled neodymium-doped yttrium lithium fluoride (Nd:YLF) laser. Once most of the pump energy has been extracted from this crystal by the seed pulse, a second electro-optic modulator (Pockels Cell) switches the amplified pulse out of the cavity.

The regenerative amplifier is usually operated close to saturation in order to maximize efficiency and pulse-to-pulse stability. Depending on the beam diameter in the crystal and the amount of pump energy, the Ti:sapphire regenerative amplifier is capable of delivering gains as high as 10^6 . By the time the overall gain has passed 10^5 , the pulse energy in a regenerative Ti:sapphire amplifier typically begins to approach the millijoule level. For femtosecond pulses, the resultant high peak power would damage the Ti:sapphire laser crystal. To avoid catastrophic damage, pulses in regenerative amplifiers are stretched in time (~ 200 ps) before amplification and

recompressed after. Because the gain per individual pass is low and many passes are required, it is vitally important to minimize cavity losses in order to optimize net gain per pass. This necessitates the use of low-loss optics that feature high reflectivity and very low scatter. In terms of output characteristics, one of the major advantages of a regenerative amplifier is that the spatial profile and pointing of the output beam is defined by the cavity. With a well-designed cavity, our regenerative amplifier is capable of delivering transform-limited ultrafast pulses in a very high-quality TEM₀₀ mode.

To ensure optimum alignment of the amplifier, it can be operated first as a laser in the absence of a seed pulse. The procedure should be: turn off the triggering of the two Pockels cells, remove the quarter-wave plate, adjust the pump beam and cavity end mirror alignment to optimize lasing in “free-running” mode, and replace the wave plate indicating no lasing. The trick is to make sure that the beam passes through the two cavity irises. The next step is to align the mode-locked seed beam into the Spitfire resonator. The procedure should be: close the shutter of the pump laser (Evolution X), reflect the seed beam into the cavity, tune the seed beam through the cavity-aligned irises by adjusting two mirrors leading the seed beam into the cavity. Then one can finish the final optimization with both the pump beam and the seed beam in the cavity. The procedure should be: optimize the overlap of the seed beam and pump beam in the laser rod by checking the intra-cavity pulse train spectrum on the oscilloscope, optimize the timing synchronization of the pockels cells with maximum output, optimize the output beam mode by slightly tuning the cavity focus mirror and end mirrors, repeat the above steps and finally have a round and clean mode output beam with maximum power. Details on the stretch and compress optimization are given in the Spitfire manual for the detailed procedures [64].

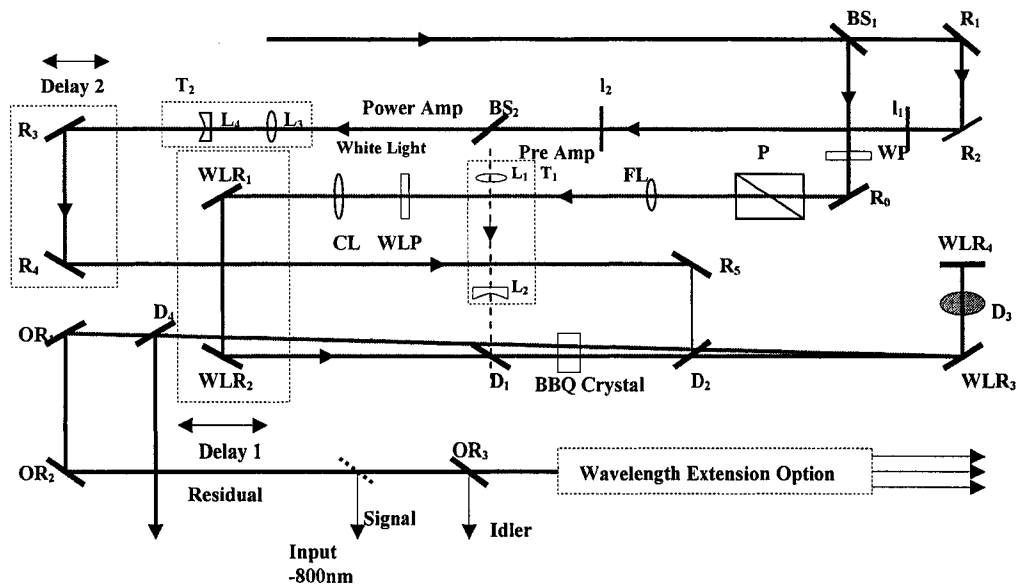


Figure 9. Layout of the optical parametric amplifier (OPA-800C, Spectra-Physics).

Optical parametric amplifier

Another important pulse generation source is the OPA-800C laser system (Spectra-Physics). The OPA system converts the 800 nm pulses from the Ti:sapphire amplifier to longer wavelengths through a type-2 OPA process (section 3.1.1). The system uses a BBO crystal as the nonlinear medium. The output pulses are tunable in the range 1140 -1600 nm (signal) and 1600 - 2650 nm (idler). Furthermore, a special-cut BBO crystal and an AgGaS₂ crystal provide the second-harmonic and different-frequency mixing (DFM) of the signal and idler beams (600 nm - 1150 nm, 3 - 10 μ m).

The femtosecond OPA-800C layout is shown in Fig. 9. The amplified Ti:sapphire beam is first reflected off two mirrors that flip the polarization from horizontal to vertical, then it is split into two legs. In the first leg, approximately 96% of the energy is transmitted and used for pumping the OPA. The remaining < 4% is

reflected by a beam splitter BS_1 to produce a white light continuum that provides the seed pulse for the OPA. A half-wave plate and a thin film polarizer control the beam energy, and a lens focuses the beam into a sapphire plate where the white light (WL) continuum is generated. The beam is re-collimated and relayed to the OPA crystal through a variable delay stage.

In the second leg, the major portion of the amplified beam is split into two pump beams, each of which is down-collimated to pump the BBO crystal. About 15% of the beam is used to pump the first pass (preamplifier stage) and the remainder is used to pump the second pass (power amplifier). In the preamplifier stage, the pump beam is steered to the BBO crystal by using a dichroic mirror, D_1 , and combined with the white light that is generated in the WL arm. The white light is temporally overlapped with the pre-pump by optimizing the first delay stage. The signal and idler beams generated in the preamplifier stage provide the seed pulse for the power amplifier stage.

The power amplifier pump beam is overlapped collinearly with the returning idler beam in the BBO crystal for the final amplification. The second delay stage is used to temporally overlap the power pump beam with the idler beam returning from mirror WLR_4 . The amplified signal and idler output wavelengths are determined by the phase-matching angle of the BBO crystal. Meantime, we have to adjust each delay stage for optimum output energy. The critical point for optimizing the OPA system is to overlap different beams in the BBO crystal as described above. More details are given in the OPA-800C manual [65].

3. 1. 3 Experimental setup

Two slightly different pump-probe setups have been used for the experiments in this thesis. Both setups allow polarization-resolved, wavelength-dependent time resolved optical studies, over a temperature range from 4-325 K.

Two-color setup

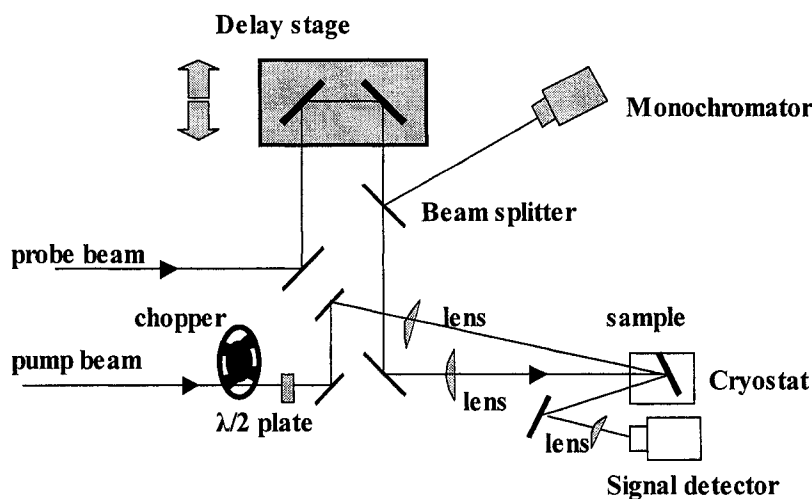


Figure 10. Pump-probe setup for two color experiments.

Figure 10 shows our two-color polarization-resolved pump-probe setup. The 150-fs pump pulses at 1.55-eV or 3.1-eV photon energy are delivered by a Ti:sapphire regenerative amplifier, whereas an optical parametric amplifier (OPA-800C, Spectra-Physics) provides the probe pulses with 150-fs duration tunable in wavelength from 400 nm to 10 μm . Two calcium fluoride lenses (focus length: 50 cm) are used to collimate the pump and probe pulses into an overlapping region of the sample with spot-diameter 2 mm. The sample is mounted either in a cryostat for temperature dependent measurements (down to 4 K) or on a rotation stage for polarization-resolved measurements. The pump beam polarization is adjustable with respect to the polarization of the probe beam. A translation stage provides the variable time delay

between the pump and probe pulses. The typical pump beam power for our experiments is less than 10 mW, and the probe beam power is less than 1 mW. The samples are mounted in an optical cryostat for temperature-dependent measurements.

For the detection, the reflected probe beam is focused onto a small photo-diode by a calcium fluoride lens through neutral density filters. Three different detector systems are used for different wavelength ranges to measure the reflectivity change (ΔR). They are a home-built Si photo diode detector, a commercial liquid nitrogen-cooled HgCdTe (MCT) photoconductive detector (EG&G Judson, Model J15D) and a InSb infrared detector (EG&G Judson, Model J15InSb-S01M-60) usable for wavelengths from 400 nm to 920 nm, 900 nm to 5500 nm, and 5500 nm to 10000 nm, respectively. The detected signal is first amplified by a low-noise voltage preamplifier. A SR250 gated integrator & boxcar averager, and a lock-in amplifier are used to average and extract the transient change of the reflected signal, ΔR , of the probe beam. The wavelength of the probe beam is measured with a monochromator.

One-color setup

Figure 11 shows our one-color, polarization-resolved setup. The setup for one-color experiments differs from the two-color setup in that the probe pulse is a small fraction of the pump pulse instead of a separately generated pulse. By means of a beamsplitter and two rutile (TiO_2) polarizers, the polarization components parallel and perpendicular to the pump pulse polarization are measured separately. The other parameters and schemes in one-color measurements are the same as those of the two-color experiments.

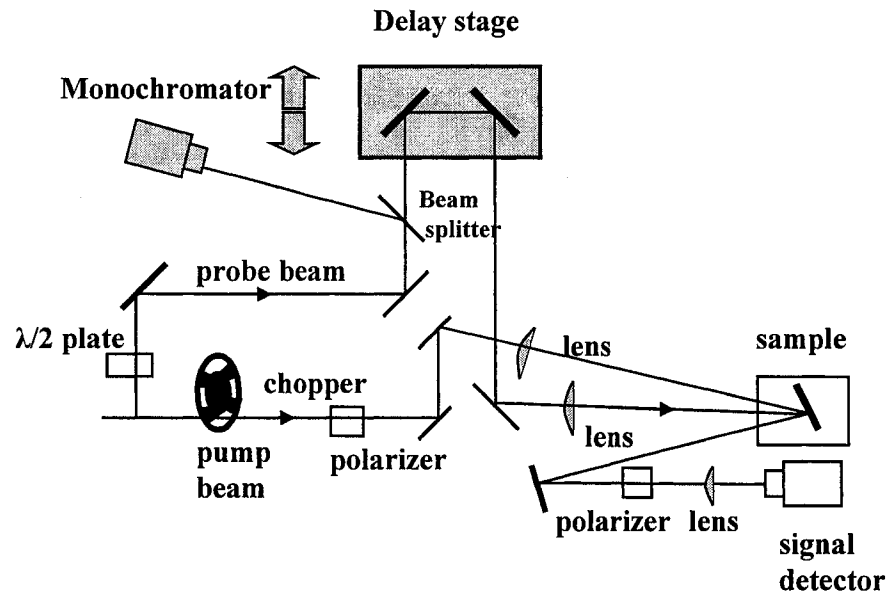


Figure 11. Pump-probe setup for one-color experiments.

3. 2 Sample preparation and characterization

3. 2. 1 Quasi-one dimensional CDW conductors

$K_{0.3}MoO_3$ (blue bronze) and $K_{0.33}MoO_3$ (red bronze) single crystals used in our experiments were prepared by Dr. Zhuan Xu from Zhejiang University in China using the electro-crystallization of high-temperature solution (ENTS) method [66]. The KMO crystals have a typical dimension of 2 cm along b axis as shown in Fig. 12 a). The crystal composition and structure were analyzed by Type AN10 X-ray energy dispersive spectrometer (EDS) and Philips APD1700 X-ray diffractometer (XRD) with Cu K_α radiation. The resistivity (Fig. 12b)) and differential resistance were determined by a four-probe method using a Datron Autocal Digital Multimeter (Input resistance $>10,000$ M Ω) and Lock-in Amplifier (Princeton Applied Research, Model 5210).

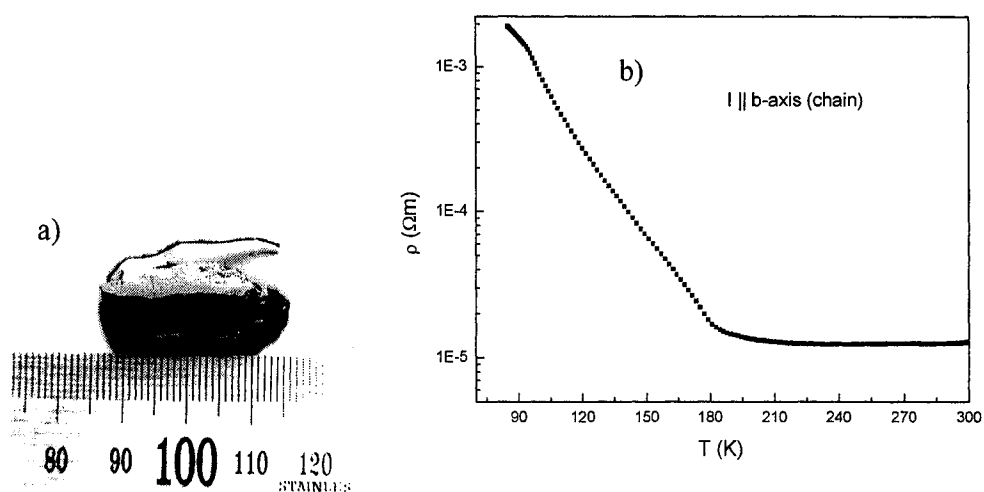


Figure 12. a) photograph of $K_{0.33}MoO_3$ single crystal having a typical dimension of 2 cm along b axis; b) Resistivity (ρ) along the chain direction as a function of temperature in $K_{0.3}MoO_3$.

3. 2. 2 CMR manganites

The single crystals of $LaMnO_3$ and $La_{0.7}Ca_{0.3}MnO_3$ used in our experiments were grown by Dr. N. H. Hur's group (Center for CMR Materials, and Superconductivity Laboratory, Korea Research Institute of Standards and Science, Korea) using the floating zone method [67].

The structures of the samples were checked with a Rigaku RAD diffractometer using $Cu K_{\alpha}$ radiation (XRD) with the power of 3 kW. The oxygen content of the samples were determined by iodometric titration and the cation compositions of the single crystals were checked by electron-probe microanalysis using an electron microscope. The scanning electron microscopy (JEOL6400) was employed to examine the surface morphology. Magnetic and transport data were measured on a

Quantum Design MPMS-5 SQUID magnetometer or a PPMS-7 magnetometer [67].

The single crystals were polished or cleaved before our optical measurements.

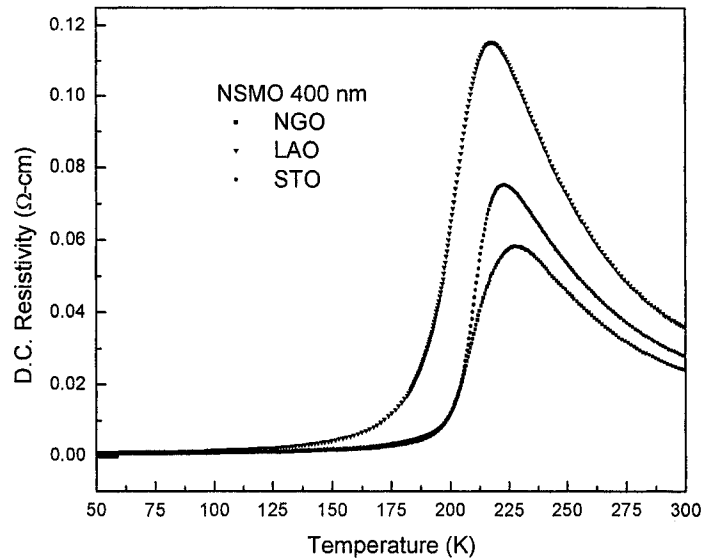


Figure 13. Resistivity (ρ) as a function of temperature in NSMO thin films on different substrates.

Thin film manganite samples used in our measurements were provided by Qi Li's group from Penn State University grown by pulsed laser deposition [59, 68]. Five $\text{RE}_{0.67}\text{A}_{0.33}\text{MnO}_3$ thin-film samples (where RE is a trivalent rare earth element and A is a divalent alkali dopant), including $\text{La}_{0.67}\text{Sr}_{0.33}\text{MnO}_3$, $\text{Pr}_{0.67}\text{Sr}_{0.33}\text{MnO}_3$, $\text{La}_{0.67}\text{Ca}_{0.33}\text{MnO}_3$, $\text{Nd}_{0.67}\text{Sr}_{0.33}\text{MnO}_3$, and $\text{Pr}_{0.67}\text{Ca}_{0.33}\text{MnO}_3$ of different thickness (100, 200 and 400 nm) were grown on three different substrates: NdGaO_3 (NGO) (110), LaAlO_3 (LAO) (100), and SrTiO_3 (STO) (100) ($5 \times 5 \text{ mm}^2$) [59, 68]. The STO, LAO, and NGO substrates induce compressive, tensile, and no strain in the manganite films. The magnetic and transport properties of the samples were characterized by electrical resistivity (Fig. 13) and magnetization measurements.

Chapter 4

Low dimensional CDW systems

Charge-density-wave conductors show strikingly nonlinear and anisotropic electrical properties, gigantic dielectric constants, unusual elastic properties, and rich dynamical behaviors [14, 69]. Recently, the main motivation for studying CDW materials was to test the validity of theoretical models of dynamic phase transition. CDW dynamics has been discussed in relation to vortex lattice systems in type-II superconductors and collective excitations in colossal magnetoresistance materials [56, 70-71].

In this chapter, we present the first time-dependent spectroscopy from the ultraviolet to mid-infrared spectrum of low-frequency collective excitations: dispersion, damping, and anisotropy of amplitude mode (AM) and phase mode (PM) in quasi-one dimensional CDW conductors, $K_{0.3}MoO_3$ and $K_{0.33}MoO_3$ on ultrafast time scales. First, we give a general introduction to the CDW phenomenon, focusing on the low energy excitation spectra in a quasi-one dimensional material, $K_{0.3}MoO_3$.

In the next sections, we present our time-resolved spectroscopic data from the quasi-one dimensional CDW conductors, $K_{0.3}MoO_3$ and $K_{0.33}MoO_3$. We analyze the data by using the theoretical model introduced in chapter 2. The discussion of the low-energy collective excitations includes the temperature evolution, dispersion relationship and anisotropy of amplitudon and transverse phason.

4. 1 Introduction to quasi-one dimensional CDW conductor

4. 1. 1 CDW ordering in quasi-1D materials

A detailed description of the CDW phenomenon is given in the recent book by Grüner [14]. A charge-density wave is a modulation of the conduction electron density in a metal and an associated modulation of the lattice atom positions. Although similar modulations are observed in many different types of solids, those which give rise to the unusual properties of quasi-one-dimensional metals have three special features: (1) like superconductivity, CDW formation is due to an instability of the metallic Fermi surface involving electron-phonon interaction; (2) CDW results in energy gaps at the Fermi surface; and (3) CDW wavelength is $\lambda_c = \pi/k_F$, where k_F is the Fermi wave vector [72].

The main reason for the occurrence of CDW in quasi-1D materials is the reduction of phase space from three-dimensions (3D) to one-dimension. This can be explained in terms of a 1D electron gas. In this case, the Fermi surface consists of only two points: one at k_F and the other at $-k_F$. The electronic susceptibility in 1D for $T=0$ is given by Lindhard response function [73]:

$$\chi(q) = \int \frac{d\vec{k}}{2\pi} \frac{f_k - f_{k+q}}{\epsilon_k - \epsilon_{k+q}} = \frac{e^2}{\pi\hbar v_F} \ln \left| \frac{q + 2k_F}{q - 2k_F} \right| \quad (T=0) \quad (29)$$

exhibiting a divergence at $q=2k_F$ [74]. This implies that any small external perturbation leads to a divergent charge redistribution suggesting that at $T=0$ the electron gas itself is unstable with respect to the formation of a periodically varying electron charge density with the wavelength π/k_F . This divergent response function caused by the topology of the Fermi surface - usually referred to as Fermi nesting - leads to various instabilities at low temperatures, depending on the particular interaction of the electronic system. The CDW ground state develops in low dimensional metals as a consequence of the electron-phonon interaction. In quasi-one-dimensional metals at low temperatures the elastic energy cost to modulate the atomic positions is less than the gain in conduction electron energy, so the CDW state is the preferred ground state. At high temperatures, the electronic energy gain is reduced by thermal excitation of electrons across the gap, so the metallic state is stable. The second-order phase transition that occurs between the metallic and CDW states is known as the Peierls transition [14].

4. 1. 2 Collective excitations in 1D CDW conductors

As expected for a complex order parameter $|\Delta|e^{i\phi}$, both phase (ϕ) and amplitude (Δ) excitations occur. In first approximation, the modes are decoupled and represent independent oscillations of the amplitude and phase of the order parameter. Both the amplitude and phase modes are the low-energy collective excitations in CDW materials. These modes are relevant to strong exchange effects and electron-electron correlations.

CDWs, mostly studied so far, are incommensurate (IC) with respect to the underlying lattice. The spatial variation of the CDW phase in an IC structure is

referred to as a phason. A dynamical mode associated with this CDW variation, also referred to as the phason, is theoretically a gapless long-wavelength excitation, which carries an electrical current.

First, we discuss the longitudinal phason (Fig. 5(a)). From frequency-dependent conductivity measurements it follows that the dynamics of the pinned CDW in $\text{K}_{0.3}\text{MoO}_3$ is quite complex [75]. In the $q = 0$ limit, the phase excitation corresponds to the translational motion of the undistorted condensate. Such a translational motion does not change the condensation energy and consequently the excitation for $q = 0$ is gapless. One finds that the frequency of the mode remains finite at $q = 0$ due to pinning of the CDW by impurities. Pinning acts as a restoring force shifting the phason frequency to some finite value also at $q = 0$. AC conductivity data at temperatures well below T_e^{3D} show a well-defined high frequency pinning mode ($q = 0$) at ~ 0.1 THz and a distribution of low-frequency pinning modes [75].

At very low temperatures ($T \ll T^{3D}$), the electrical and thermal properties of CDW conductors exhibit many features characteristic of a glass. The single-particle density is very small and the screening is ineffective, so the CDW is stiffened by Coulomb interactions. Only pinning-related CDW compressions and expansions change the charge density. The long-range Coulomb forces modify the phason dispersion relation ($\omega_\phi \propto q$) and bring a strong temperature dependence in the dispersion relation. When Coulomb forces are screened by quasi-particles excited above the Peierls gap, the collective motion is compensated by the quasi-particle current and the longitudinal phase mode remains acoustic [14]. The dispersion relation of the longitudinal phase mode provides a sensitive probe for the screening of the Coulomb interaction by quasi-particles and the depinning of the CDW modes.

In contrast, the transverse phase modes (Fig. 5(b)) are unaffected by Coulomb interaction. The transverse phason dispersion remains acoustic in the entire temperature range as indicated by Viroztek and Maki [57]. The transverse modes do not involve an electrical current. In general, the transverse phason velocity is comparable to the sound velocity and is of an order or much smaller than the longitudinal phason velocity at very low temperature ($T \ll T^{3D}$) [57].

Besides the two different phason modes, another important collective excitation of the CDW state is the amplitude mode. The modulation of the CDW amplitude changes the condensation energy and has therefore a finite frequency. In CDW conductors, fluctuations of the single particle gap lead to fluctuations of the ionic positions. The amplitude mode oscillation frequency is substantially lower than the gap frequency. Since amplitude mode oscillations involve no net displacement of the electronic charge with respect to the ionic positions, the mode is expected to be Raman active. Its temperature dependence can be calculated within the Ginzburg-Landau theory and was found to drop to zero at the Peierls transition temperature.

Experimentally, the temperature dependence of amplitude mode frequency and damping was studied recently by time-resolved nonlinear pump-probe technique, as well as, Raman and neutron spectroscopy [31, 76-77]. The amplitude excitations are controlled by the mean-field behavior of the distorted Peierls chain. At temperatures close to zero, the amplitudon frequency in $\text{K}_{0.3}\text{MoO}_3$ is $\omega_A \sim 1.7$ THz. The frequency softens as T_c^{3D} is approached, but does not drop to zero completely [14]. Neutron data also show continuous behavior at T_c^{3D} . It follows that at $q = 2k_F$ there is an overdamped structure in the vicinity of T_c^{3D} that evolved from underdamped Kohn anomaly and separates into amplitude and phase modes at temperatures below T_c^{3D} .

Theoretical studies of the dynamics of the Peierls chain [77] indeed show coupling between phason and amplitudon in some temperature interval below T_c^{3D} and indicate that the dynamics of the collective modes is not strongly affected by interchain coupling. This is supported by neutron [77] and Raman [76] data as well.

4. 2 Low-energy CDW dynamics

$K_{0.3}MoO_3$ is the most intensively studied quasi-1D CDW conductor due to the availability of large single crystals. In this section, we report on the first time-resolved spectroscopic measurements of the collective CDW excitations in quasi-one dimensional CDW conductors, $K_{0.3}MoO_3$ and $K_{0.33}MoO_3$ in the long-wavelength limit at 30 K. We present the dispersion relation (in the frequency range from 5 – 40 GHz), phase damping constant, temperature dependence and anisotropy of the transverse phase mode in $K_{0.3}MoO_3$ and $K_{0.33}MoO_3$. The dispersion relation, damping and temperature dependence of amplitude mode were studied as well.

4. 2. 1 Dispersion relation of the collective modes

In the time-resolved experiments, a $K_{0.3}MoO_3$ (or $K_{0.33}MoO_3$) single crystal is excited by 150-fs pump pulses at 1.55-eV photon energy delivered by a Ti:sapphire regenerative amplifier operating at 1-KHz repetition rate. The KMO single crystal (5 mm*5 mm*0.5 mm) is *c*-axis oriented. The probe beam, polarized parallel to the sample surface, probes directly the (*a'*-*b*)-plane reflectivity, where *a'* represents the [102] direction of the $K_{0.3}MoO_3$ (or $K_{0.33}MoO_3$) single crystal. The *b*-axis is the direction along the chain. An optical parametric amplifier (OPA-800C, Spectra-Physics) provides the 150-fs probe pulses tunable in wavelength from 400 nm to 10

μm . The unfocused pump beam, spot-diameter 2 mm, and the time-delayed probe beam are overlapped on the sample with their polarization perpendicular to each other. The typical pump beam power is less than 4 mW, and the probe beam power is less than 1 mW. The change of the reflected probe beam intensity (ΔR) induced by the pump beam is recorded as a function of time delay for different wavelengths of the probe beam ($\lambda_{\text{probe}} = 400 \text{ nm} - 2.5 \mu\text{m}$). A SR250 gated integrator & boxcar averager, and a lock-in amplifier are used to measure the transient reflectivity change ΔR of the probe beam.

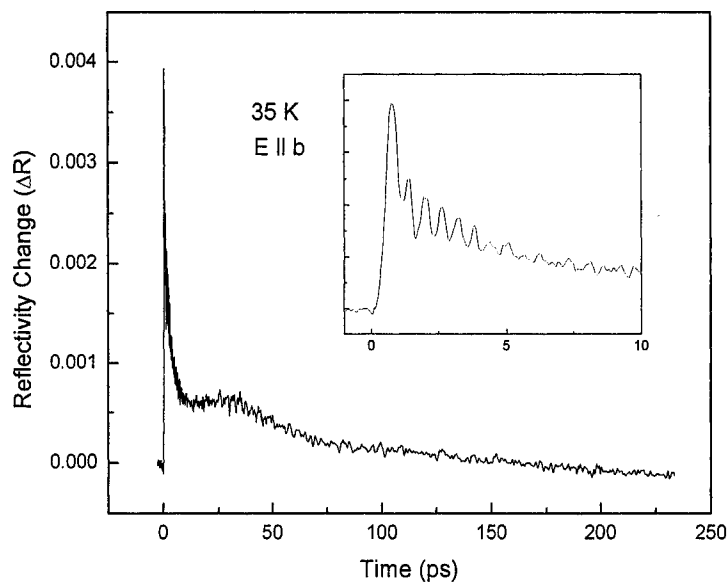


Figure 14. Transient reflectivity change ΔR at 800-nm probe wavelength from $\text{K}_{0.3}\text{MoO}_3$ single crystal at 35 K. The inset depicts the fast oscillations on a short time scale.

Figure 14 shows the time evolution of ΔR for a $\text{K}_{0.3}\text{MoO}_3$ single crystal at 35 K. The data are taken with pump and probe wavelength at 800 nm. The probe beam polarization is parallel to the chain direction ($E \parallel b$). The decay of ΔR shows two

damped oscillatory components on top of a bi-exponential decay. The fast oscillations of ΔR are shown on a picosecond time scale in the inset of Fig. 14. The trace shows several damped oscillations. The frequency of these oscillations is ~ 1.67 THz obtained by Fourier transformation. This value is in good agreement with the frequency of the amplitude mode in $\text{K}_{0.3}\text{MoO}_3$ obtained from previous time-resolved optical measurements [31], as well as neutron [77] and Raman scattering [76]. The amplitude of the fast oscillation is independent of the probe pulse polarization and rather isotropic in the a' - b plane, which is consistent with the A_1 symmetry of the amplitude mode [31]. Besides the fast oscillation, the data also reveal a slow strongly overdamped modulation of ΔR (Fig. 14). The frequency of this mode is ~ 0.015 THz.

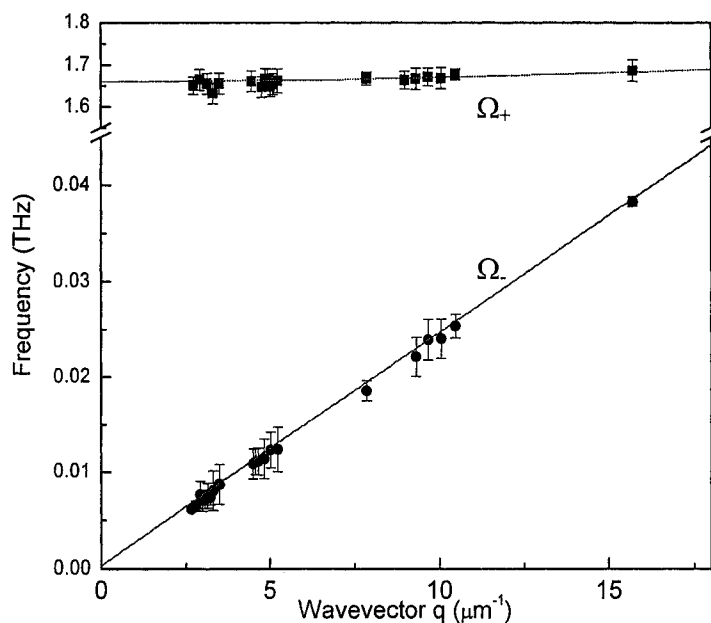


Figure 15. Transverse phase (Ω_-) and amplitude (Ω_+) mode dispersion relations of $\text{K}_{0.3}\text{MoO}_3$ at 30 K in the long-wavelength limit.

To identify the origin of these slow oscillations we performed spectroscopic measurements of ΔR as a function of probe wavelength in the range of 400 to 2500 nm.

The dispersion relations of the slow and fast oscillations of ΔR in $K_{0.3}MoO_3$ at 30 K are displayed in Fig. 15. The wave number is given by $q = 2\pi/\lambda$, where λ is the probe wavelength and n is the refractive index of $K_{0.3}MoO_3$. The dispersionless amplitude mode exhibits a gap for $q \rightarrow 0$, with a frequency $\Omega_+(q=0) \sim 1.66$ THz (Fig. 16). This value is close to the frequency of the unrenormalized longitudinal optical phonon mode, $\omega_{2k_F} = 1.5$ THz [14]. From $\Omega_+(q=0) = \lambda^{n/2} \omega_{2k_F}$ follows that λ' is approximately unity in good agreement with the value obtained from mean field theory and recent optical studies [14]. The observed frequency dependence of the slow oscillation is in full agreement with the linear dispersion relation of the transverse phase mode as predicted by Eq. (16). The slope of the Ω -branch gives a phason velocity of $c_0 = 1.4 \pm 0.1 \times 10^3$ m/s. This value is in very good agreement with the transverse phason velocity predicted by Viroztek and Maki [57].

The frequency of these collective modes is found to be independent of the polarization and wavelength of the pump beam. This excitation mechanism is different from previous pump-probe transmission experiments in weakly absorbing crystals [78], in which the wave-vector of the excited modes is determined by the phase-matching condition of the pump beam. Since the absorption depth in $K_{0.3}MoO_3$ is ~ 100 nm for wavelengths in the visible to infrared range, a broad spectrum of the collective mode down to frequencies of order ν/ξ (~ 5 GHz for $K_{0.3}MoO_3$ and $K_{0.33}MoO_3$) are excited and propagate normal to the surface into the material. We use a time-delayed probe light pulse to detect the frequency spectrum of the charge density fluctuation. Part of the probe light pulse is reflected by the wave front of the

excited charge-density fluctuations, and the remainder at the surface of the CDW single crystals. These reflections interfere constructively or destructively depending on the position and time of the charge density modulation (Chap. 2). Because of the phase matching condition for the probe pulse, the frequency of the oscillations is the frequency of a transverse phason with certain wavenumber, and the damping of the oscillations is the damping of the same phason. Thus, from a measurement of $\Delta R(t)$ we can deduce the phase velocity and damping rate of transverse phasons with low-frequency in the Brillouin range.

In principle, both the longitudinal and transverse phason should couple to the probe pulse and give oscillatory components to the time-resolved reflectivity change, $\Delta R(t)$. However, since the pump spot size at the crystal is quite large, the sample surface within that spot is excited in a more or less spatially uniform manner. The pump pulse is strongly absorbed at the surface, so that the excitation of the sample has a large gradient going into the sample from the surface, and a very small gradient across the pump spot. The wave vector component must be very nearly zero in any direction along the surface (also along the chain direction) but can be large in the direction normal to the surface (i.e. "transverse" direction). This is similar to femtosecond excitation of acoustic wavepackets that propagate into the sample from a strongly absorbing sample, e.g., work by Hao and Maris [79-80]. Thus, the charge density wave propagation develops in $K_{0.3}MoO_3$ normal to the surface, i.e., (a' - b) plane, so that only the transverse phason is generated. The photo-induced transverse phason shows a linear acoustic-like dispersion relation in the long-wavelength limit as shown in Fig. 15. The behavior is consistent with theoretical prediction of the transverse phason [57].

Further information on the transverse phason dynamics is obtained from the dependence of period, amplitude, and damping rate on the doping concentration between the two bronze oxides. Figure 16 shows the time evolution of ΔR for a $K_{0.3}MoO_3$ single crystal at 30 K and a $K_{0.33}MoO_3$ single crystal at 290 K. The data are taken with the pump laser wavelength at 800 nm, whereas the probe wavelength is

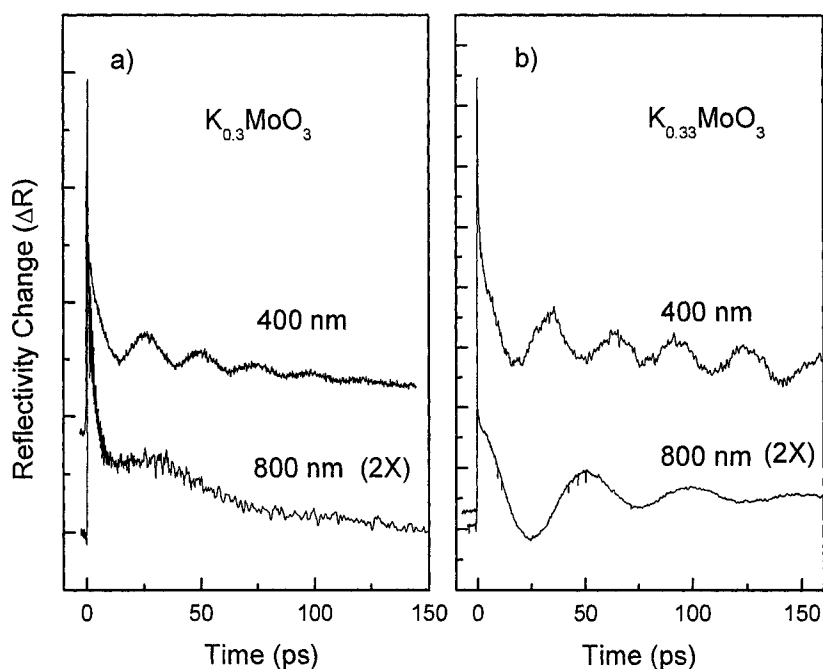


Figure 16. The time evolution of ΔR at $E \parallel b$ for a) a $K_{0.3}MoO_3$ single crystal at 30 K; and b) a $K_{0.33}MoO_3$ single crystal at 290 K with the pump laser wavelength at 800 nm, and the probe wavelength at 800 nm and 400 nm, respectively.

800 nm and 400 nm, respectively. The probe beam polarization is parallel to the chain direction ($E \parallel b$). Similar to the blue bronze, the red bronze signal, ΔR , also shows a slow oscillatory component on top of a bi-exponential decay. However, the 400-nm data of red bronze reveal a longer modulation period of 31.3 ps ($E \parallel b$) as compared to 23.5 ps observed in $K_{0.3}MoO_3$. The oscillations in $K_{0.33}MoO_3$ persist well for at least

$\Delta t=600$ ps with very little damping. Similarly, the 800-nm data of $\text{K}_{0.33}\text{MoO}_3$ (Fig. 16 (b)) shows at least three modulation period in contrast to the strongly overdamped modulation of ΔR at 800-nm probe wavelength for $\text{K}_{0.3}\text{MoO}_3$ (Fig. 16 (a)). This is consistent with polarized reflectivity spectra of $\text{K}_{0.33}\text{MoO}_3$, which show different intensities and resonances with respect to $\text{K}_{0.3}\text{MoO}_3$ [81].

In contrast to the fast damping rate, $\tau_A \cong 10$ ps, observed for the amplitude mode [76], a least-square fit of the 400-nm data in $\text{K}_{0.3}\text{MoO}_3$ gives a damping constant $\tau_p > 55$ ps for the transverse phason oscillation at $\Omega = 0.035$ THz (Fig. 16 (a)). Although the damping constant is in good agreement with the underdamped response from ac-conductivity measurements [82], the value is quite different from the parameters reported in far-infrared [83] and neutron scattering measurements [77]. The difference can be explained by the coupling between pinned modes and transverse phasons in distinct frequency range. The mode is very weakly damped at microwave frequencies ($\omega/2\pi \gg 10^{10}$ Hz) [26].

4. 2. 3 Anisotropy of the transverse phason

Figure 17 (a) shows the transient reflectivity change ΔR of $\text{K}_{0.3}\text{MoO}_3$ at room temperature measured with the probe beam polarization parallel ($E \parallel b$) and perpendicular ($E \perp b$) to the chain direction. The pump laser wavelength is 800 nm, whereas the probe wavelength is 400 nm. In contrast to the 800-nm trace in Fig. 14, which shows only one strongly damped oscillation, the 400-nm data reveal clear modulations with a period of 23.5 ps ($E \parallel b$) and 33 ps ($E \perp b$), which persist well for five periods.

The inset of Fig. 17 shows the anisotropy of the transverse phason oscillation period in the a' - b plane at room temperature. From Eq. (16), $\Omega_{T-} = cq$, the transverse

phason velocity with $E \perp b$ is calculated as $c_{\perp} = 1.1 \pm 0.1 \times 10^3$ m/s, which is smaller than the transverse phason velocity with $E \parallel b$, $c_{\parallel} = 1.4 \pm 0.1 \times 10^3$ m/s. This anisotropy is due to the difference of the CDW coupling along and normal to the chains [26].

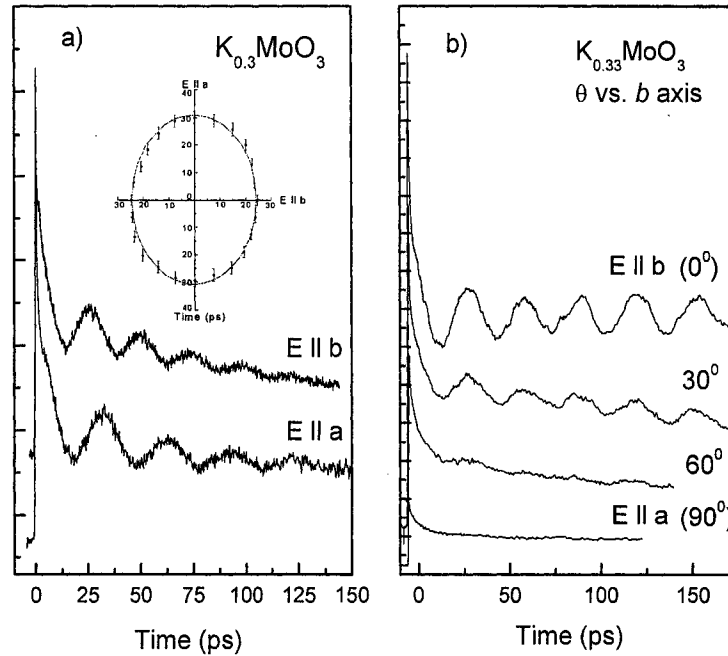


Figure 17. a) Transient reflectivity change ΔR in $K_{0.3}MoO_3$ at 400-nm probe wavelength with the polarization vector parallel ($E \parallel b$) and perpendicular ($E \perp b$) to the chain direction. The inset shows the anisotropy of the oscillation period in the a' - b plane; b) The anisotropy of the oscillatory pump-probe signal for different probe polarization angle with respect to the b axis (θ vs. b) on $K_{0.33}MoO_3$.

For a quasi-1D system density wave fluctuations on the neighboring chains become correlated because of the inter-chain interactions and this leads to a transition to a ground state with three-dimensional, long-range order. The Coulomb interactions between two neighboring chains tend to align the chains with a certain coherence length, ξ_{\perp} . The coupling is different (anisotropic) parallel and perpendicular to the

chain. The anisotropy can be observed as the probe beam polarization is rotated from parallel ($E \parallel b$) with the chain direction to perpendicular ($E \perp b$). The argument is supported by x-ray data from $K_{0.3}MoO_3$ [84]. The analysis of the Bragg pattern shows a crossover at ~ 200 K from 3D fluctuation region that exists up to approximately 20 K above T_c^{3D} to a region where quasi-2D fluctuations exist [84].

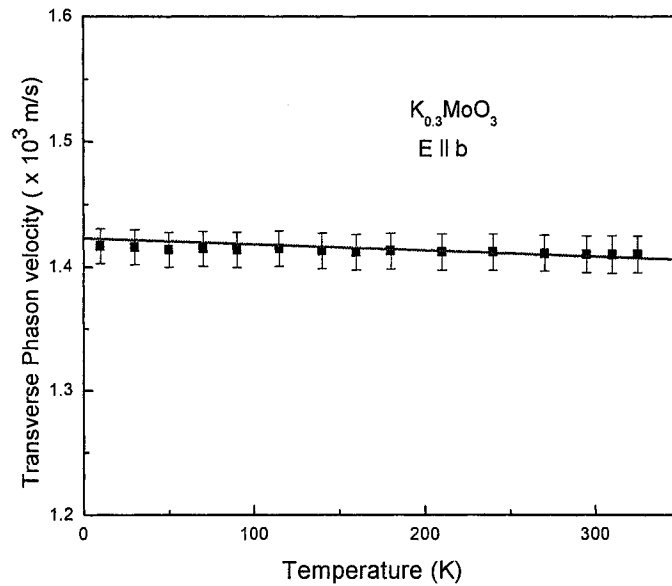


Figure 18. Temperature dependence data of the transverse phason velocity, $c_{||}$ in $K_{0.3}MoO_3$ along the chain direction.

In contrast to the blue bronze, $K_{0.3}MoO_3$, the anisotropy must be more pronounced in red bronze, $K_{0.33}MoO_3$, considering that the states at E_F in the blue bronze are delocalized, whereas they are localized in $K_{0.33}MoO_3$ [81]. Due to further reduction of the phase space, only short-range correlations occur in $K_{0.33}MoO_3$ along the chain direction. Coulomb interactions cannot lead to a coherent CDW modulation on the neighboring chains. Our anisotropy measurements on $K_{0.33}MoO_3$ support this argument. As shown in Fig. 17b), a strong oscillatory signal occurs when the

polarization of the probe beam is parallel to the chain direction, $E \parallel b$. The oscillations fade away in the direction of $E \perp b$. The results are in agreement with stronger anisotropy of the $4d$ electronic band structure, in $K_{0.33}MoO_3$ vs. $K_{0.3}MoO_3$ [81].

It is interesting to further discuss the temperature evolution of the transverse-phason spectrum. In contrast to the longitudinal phason, which splits into two modes: one acoustic and one optical mode in the presence of Coulomb interaction, the transverse modes remain acoustic in the entire temperature range. Figure 18 shows the temperature dependence data of the transverse phason velocity, c_{\parallel} , in $K_{0.3}MoO_3$ along the chain direction. c_{\parallel} shows a very weak temperature dependence. This is in good agreement with the theoretical predictions [57]:

$$c_{\parallel} \propto [m/m_s^*(T)]^{1/2} \quad (30)$$

where m is the electron mass, $m_s^*(T)$ is the temperature dependent phason mass in the static limit. The results are also strikingly confirmed by neutron inelastic scattering measurements [77].

In summary, we have measured for the first time dispersion and anisotropy of the collective CDW excitations in quasi-one dimensional CDW conductors, blue bronze ($K_{0.3}MoO_3$) and red bronze ($K_{0.33}MoO_3$) in the long-wavelength limit for a broad temperature range (from 4 K – 325 K). A linear gapless (acoustic-like) dispersion relation is observed for the low-energy transverse phasons. The phason velocity is strongly anisotropic with a very weak temperature dependence. The amplitude mode exhibits a weak (optic-like) dispersion relation with a frequency $\Omega_+(q$

$\omega = 0) = 1.67$ THz at 30 K. This mode is softening and disappearing as T approaches T_{CDW} .

Chapter 5

Colossal magneto-resistance manganites

The richness of the physical properties of CMR manganites originates from the strong interplay between the charge, lattice, orbital, and spin degrees of freedom found in these systems [85-98]. Although several mechanisms, involving double exchange (DE) [85-87], electron-phonon interactions [88-97], and electron-electron correlations [85-87, 97-100], have been proposed to explain the observed CMR effect, a clear understanding of its microscopic origin is still lacking. Presently, the dynamics of Jahn-Teller (JT) distortions of the MnO_6 octahedra and charge-ordering phases are found to be crucial to elucidate the metal-to-insulator (MI) transition and the CMR effect [88-100].

In this chapter, we present ultrafast time-resolved nonlinear spectroscopic data from the ultraviolet to mid-infrared range near the MI transition in doped perovskite manganites: $\text{La}_{0.67}\text{Ca}_{0.33}\text{MnO}_3$ (LCMO), $\text{La}_{0.67}\text{Sr}_{0.33}\text{MnO}_3$ (LSMO), $\text{Nd}_{0.67}\text{Sr}_{0.33}\text{MnO}_3$ (NSMO), and $\text{LaMnO}_{3+\delta}$ (LMO). We first give a general introduction to the CMR

phenomena, focusing on charge ordering phases and phase separation in a prototypical CMR material, LCMO. In the next section, we present the first time-resolved spectroscopic data taken from LCMO thin film and single crystal, which reveal a strongly damped low-energy collective mode. The origin of this mode is attributed to the opening of a pseudogap resulting from charge/orbital ordering phases. The regular pattern of the valence electrons modifies the uniformity of the charge density, leading to the development of a CDW condensate which cooperates with Jahn-Teller distortion and compete with the electron itinerancy favored by double exchange (DE) mechanism. Damping of the oscillatory components in the vicinity of the MI transition is discussed with respect to inhomogenous phases. The temperature evolution of a soft-lattice mode provides further information about electronic and structural instability and phase changes. In section 5.2.4, we discuss quasiparticle dynamics in the presence of small polarons, phase separation and percolation. Further, a very long-lived relaxation component is observed in time-resolved transient reflectivity measurements from LCMO, LSMO, NSMO and LMO single crystals and thin films. The results are ascribed to a slow spin relaxation process caused by pseudogap opening and phase segregation. Last, we discuss the effect of strain on spin dynamics in NSMO near the metal–insulator transition.

5. 1 Introduction

5. 1. 1 Electronic properties of doped manganites

One peculiar feature of the doped manganite perovskites is the close association of ferromagnetism with metallic conduction. Zener [85] proposed the mechanism of double exchange to explain this correlation. Doping of the trivalent rare-earth site by

divalent ions causes a corresponding number of Mn^{3+} ions to become Mn^{4+} . The displacement of these holes (sometimes referred to as Zener carriers [85]) increases the conductivity. The strong positive exchange coupling between the Mn^{3+} and Mn^{4+} ions in $\text{Mn}^{3+}\text{-O-Mn}^{4+}$ provides a mechanism for ferromagnetic ordering. A resonance hybrid between the two states $\Psi_1: \text{Mn}^{3+}\text{-O}^{2-}\text{-Mn}^{4+}$ and $\Psi_2: \text{Mn}^{4+}\text{-O}^{2-}\text{-Mn}^{3+}$ is energetically favored. For such a simplified model, the transfer integral for one electron becomes [85-87] $t_{ij} = b_{ij} \cos(\theta_{ij} / 2)$, where θ_{ij} is the angle between the two ionic spins and b_{ij} is the coupling constant. When considered in the environment of an extended lattice, this interplay between dopant level and the magnetic ground state leads to the theoretical proposal of either a canted or a spiral ground state for the Mn spin, with θ_{ij} determined by dopant concentration x [85-87].

Double exchange provides a mechanism for the simultaneous onset of metallicity and ferromagnetism. On the other hand, Millis et al. [88-89] showed that a Hamiltonian containing only double exchange is insufficient to account for the large magnetoresistance observed in these CMR compounds. The calculated resistance is too small. It has an incorrect temperature- and magnetic-field dependence when compared with experiment. They concluded that a strong electron-phonon interaction, in this case, mediated by the Jahn-Teller coupling of the Mn^{3+} ions, must be included. The competing tendency, toward localization, comes about through the Jahn-Teller effect, in which a valence electron stabilizes a local distortion of the oxygen octahedron surrounding each manganese atom. In this way, a carrier can be trapped by a self-induced crystal distortion.

Energetically, the competition between double exchange and Jahn-Teller effect may be understood as follows. Double exchange delocalizes the valence electrons, lowering their kinetic energy. By contrast, localized valence electrons save energy

because they produce Jahn-Teller distortions. However, localized electrons have a higher kinetic energy, and delocalized electrons suppress the Jahn-Teller effect (and electron-phonon coupling effects in general). Therefore, the competition between double exchange and Jahn-Teller effect typically leads to complex mesoscopic textures of doped manganites.

5. 1. 2 Charge ordering and phase separation of CMR manganites

Manganites display three electronic phases: charge-ordered insulator (COI), ferromagnetic metal (FMM), and a paramagnetic phase (PM). The COI, FMM, and PM phases may be plotted on a schematic diagram such as Fig. 19 [100]. At any point in the diagram, the thermodynamically stable phase depends on the relative strengths of two competing processes: double exchange and Jahn-Teller effect as discussed above. The vertical axis of the phase diagram is temperature, which influences the two-way competition in that ordered phases typically form below a few hundred

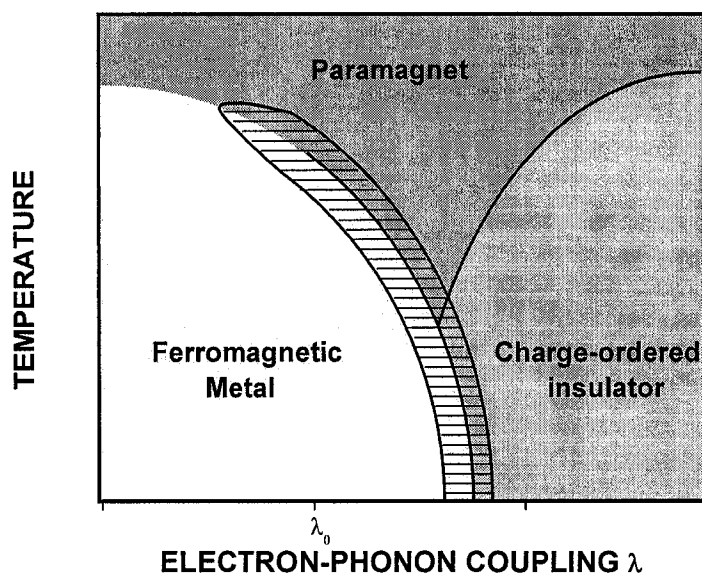


Figure 19. A schematic phase diagram of doped manganites from N. Mathur et al [16].

Kelvin. The horizontal axes is the electron-phonon coupling parameter, λ , which reflects the two-way competition and measures the strength with which valence electrons interact with the crystal lattice. COI and FMM states have very similar energies, resulting in the two-phase coexistence of FMM and COI regions [98,100-102]. The similarity of the energies of the FMM and COI phases leads to a sensitive balance between FMM and COI regions that can be tilted in favor of the COI phase by an increase in the structure distortion away from the ideal cubic perovskite lattice [98,100-102]. The structural distortion can be increased by applying internal pressure by the substitution of smaller ions at the *A* site (*A* site refers to the ABO_3 perovskite structure) or by applying anisotropic stress [102].

Beyond the pure phase behavior, the observation of electronic phase separation in these materials is generally accepted. It has been shown that for a wide range of temperature and lattice coupling constant, λ , there is a coexistence of FMM and COI phases [98,100-102], which can be tilted in favor of the FMM phase by the application of a magnetic field or external hydrostatic pressure. The phase coexistence has been observed also for different values of hole-doping concentration x [100]. For example, the tendency has been verified for doping levels of LCMO in the middle of the FM regime. Evidence of charge inhomogeneities at low temperature was reported from muon spin resonance [103], x-ray absorption [104], and optical experiments [105-106], whereas at high temperatures polaron-like inhomogeneities were inferred from neutron scattering experiments [92, 107] and x-ray absorption [108]. The phase transition and associated magnetoresistance properties were also related to a percolation of metallic ferromagnetic domains from scanning tunneling spectroscopy [109].

5. 2 Experimental results

In the doped manganites, it has recently been recognized that dynamic or spatially fluctuating correlations of charge/spin/orbital degrees of freedom can play an important role in the CMR phenomena [85-98]. The nanoscale fluctuating charge/orbital modulations cooperate with Jahn-Teller distortions and compete with the electron itinerancy favored by double exchange [88-100]. Recently, neutron scattering experiments showed that short-range correlation of the so-called CE-type charge ordering exists in the ferromagnetic (FM) manganite, LCMO, above the Curie temperature T_C , explaining its large resistivity and magnetoresistance near T_C [92, 107]. Therefore, it is fundamentally important to better understand the dynamic or short-range charge/spin stripes, in relation to the physical properties of the CMR materials.

In this section, we report on the first time-resolved spectroscopic measurements of the collective excitations and quasiparticle dynamics in a prototypical CMR material, LCMO, in the long-wavelength limit. The quasiparticle dynamics in the vicinity of a metal-insulator transition are discussed with respect to the opening of a pseudogap, phase separation and percolation. Furthermore, we elucidate the origin of a strongly damped low-energy collective mode, its dispersion relation, temperature evolution and dependence on hole-doping concentration of LCMO.

5. 2. 1 Opening of pseudogap

The low-temperature state of LCMO is a very poor metal with the resistivity on the order of the inverse of Mott's minimum metallic conductivity. Such poor conductivity would typically be regarded as the outcome of either very strong scattering (a short mean free path on the order of the lattice constant) or a very small number of carriers

(small Fermi surface (FS) volume). However, ARPES experiments in layered manganites directly showed that neither can be the case [13]. In order to resolve this inconsistency, other mechanisms must be included, the most obvious of which is the suppression of spectral weight near E_F [13].

Unusual behavior in the spectral weight of the ARPES dispersive peak, falling rapidly over quite a large energy scale (nearly 0.5 eV) as the peak approaches E_F , was previously termed the “pseudogap” (Fig. 20) [110-111]. It is not expected in the simple theory of metals, in which the spectral weight remains constant until it is cut by the Fermi function. This pseudogap will decrease the conductivity by removing a large portion of the carriers from the conduction process. As the temperature is raised above T_C , the pseudogap removes nearly all remaining spectral weight at E_F , which is

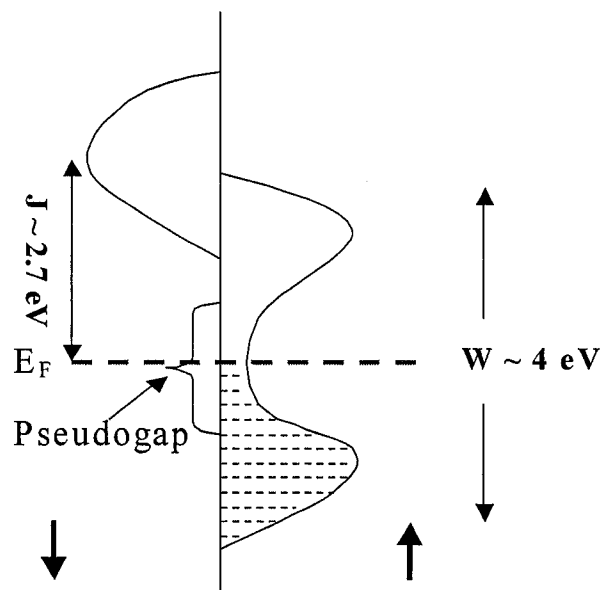


Figure 20. A schematic illustrating the up and down-spin density of states for 3-dimensional manganites. The experimentally observed pseudogap at E_F is also indicated [99].

consistent with the insulating behavior of the high-temperature phase. Therefore, the pseudogap appears to be critical for explaining the poor conductivity of both phases.

The loss of spectral weight due to pseudogap opening can be monitored as a function of temperature and probe pulse energy by measuring the reflectivity change, ΔR_0 (i.e., $\Delta R(t=0)$), in our two-color pump-probe setup as described in Chap. 4. The principle of the measurement is similar to thermo-modulation spectroscopy, which involves periodically perturbing the sample's temperature and measuring the changes in the optical absorption spectrum occurring in synchronism with the perturbation (Fig. 21). Since electron-electron scattering, τ_{e-e} , is much faster than the period of a typical phonon vibration, electrons are decoupled from the lattice, and the electronic system can be described by high photoexcitation density pulses. Since only changes in

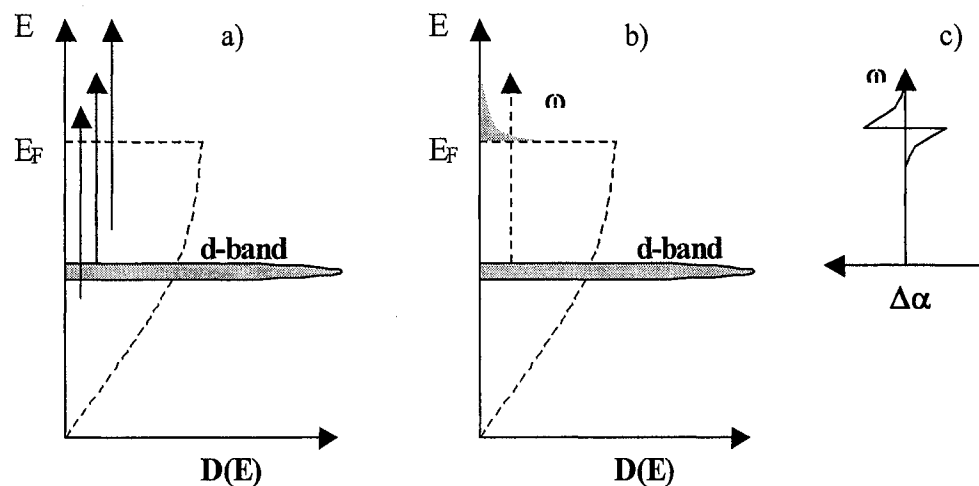


Figure 21. Thermomodulation mechanism: a) photoexcitation, where the arrows represent possible electronic transitions from occupied (hatched) to unoccupied electronic states, results in b) Fermi smearing thereby opening some states and blocking others for optical transition. c) A derivative-like feature (i.e. absorption $\Delta\alpha$) with respect to the probe photon energy ω when the probe photon energy matches the energy of d-band to E_F transition [56].

the optical spectrum are measured, the modulation spectroscopy is very sensitive to the critical points in the band structure, i.e. the presence of narrow bands below E_F giving rise to large joint density of states [112].

For the transient reflectivity measurements the samples were mounted in an optical cryostat. The laser system consists of a Ti:sapphire regenerative amplifier (Spitfire, Spectra-Physics) and an optical parametric amplifier (OPA-800C, Spectra-Physics) delivering 150-fs short pulses at a 1-kHz repetition rate tunable from 400 nm to 10 μm . A two-color pump-probe setup is employed with the pump beam power < 6 mW and the probe beam power < 1 mW as described in Chap. 4.

Under pump-illumination, the Fermi distribution of unoccupied states, $\rho = 1 - 1 / \{1 + \exp[-(E_F - E_d - \hbar\omega) / kT]\}$ increases slightly for $\hbar\omega < E_F - E_d$. That is $\partial\rho / \partial t > 0$, and more d -band electrons absorb probe photons, resulting in a reflectivity decrease ($\partial R_0 / R_0 < 0$), i.e. transient absorption. On the other hand, for $\hbar\omega > E_F - E_d$, there is a decrease in the number of unoccupied states above E_F and thus $\partial R_0 / R_0 > 0$ i.e. transient bleaching. As $\hbar\omega = E_F - E_d$, there is no modulation of the unoccupied state sampled, because to first order $\partial\rho / \partial t = 0$ [112].

As shown in Fig. 22(a), the polarity reversal with increasing temperature can be understood easily in terms of a pump-induced change in unoccupied electronic states near the Fermi level. These states are probed by monitoring the change in reflectivity at a probe energy of 1.08 eV, 0.51 eV and 1.55 eV, respectively. The probe pulse induces transitions of electrons from the upper edge of a filled e_g band of d electrons (E_d) to an unoccupied e_g band close to the Fermi level.

Thus, for LCMO single crystal (Fig. 22(a)), the polarity reversal represents the opening of a pseudogap with increasing the temperature. We consider fit the data

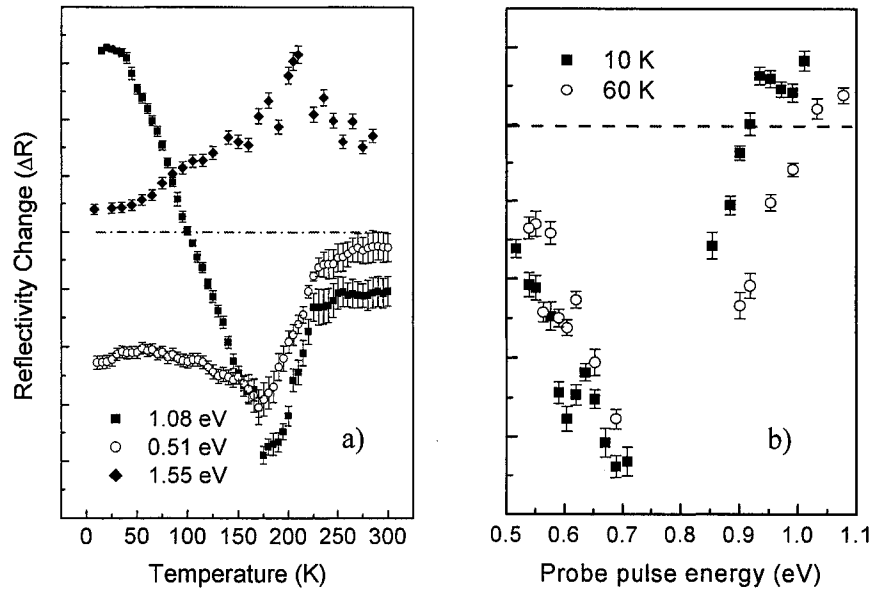


Figure 22. The reflectivity change ΔR_θ (at $\Delta t=0$) in LCMO single crystal as a function of a) temperature with a probe energy at 0.51 eV, 1.08 eV, and 1.55 eV, respectively; b) probe energies at 10 K and 60 K.

taken with a probe energy of 1.08 eV (Fig. 22 a)). At very low temperature ($T \ll T_C$), ΔR_θ is constant with the same joint spectral density around E_F . ΔR_θ starts to decrease at $T \sim 50$ K. The pseudogap size reaches 1.08 eV at 100 K as temperature increases. Above T_C , ΔR_θ is constant again with no change of the pseudogap. For comparison, we repeat the measurement with a probe energy of 0.51 eV and 1.55 eV (Fig. 22(a)). We can clearly see a similar trend of the reflectivity change, ΔR_θ , although for 0.51 eV (1.55 eV) probe pulse ΔR_θ remains negative (positive) for the whole temperature range, as expected for $\hbar\omega < (>)E_F - E_d$, respectively.

The opening of a pseudogap is also confirmed by the spectroscopic pump-probe measurements at 10 K and 60 K (Fig. 22(b)). The pseudogap size clearly shifts from

0.92 eV to 1.02 eV with increasing temperature. This is in good agreement with the loss of spectral weight around T_C observed by recent ARPES spectra [13, 110-111, 113].

A number of possibilities exist to explain the pseudogap, both intrinsic and extrinsic. We begin with the extrinsic possibilities, which we argue can be largely excluded. First, there is the extrinsic ohmic loss effect due to poor conductivity [114]. However, recent experiments [115-116] and theories [116] convincingly argue that this is very unlikely to be a major concern. Next, there is the matrix element effect, which will modulate the spectral intensities near E_F and in general has both energy- and momentum-dependent terms. Chuang et al. have taken their ARPES spectra at

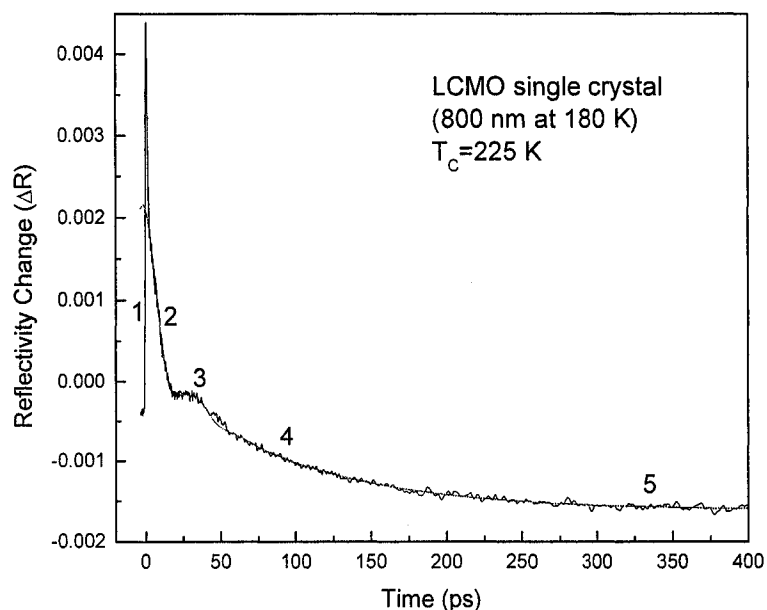


Figure 23. Time evolution of ΔR for LCMO single crystal at 180 K.

various photon energies (between ~ 20 and 50 eV) and polarizations for layered manganites [13]. The authors indicated that the spectral weight loss trend is still robust although the weights do vary slightly with photon energy, which excludes the matrix element effect. Additionally, optical conductivity experiments have also shown the absence of the Drude peak in LCMO [97], which may be closely related to the pseudogap. Intrinsic effects to explain the pseudogap include Jahn-Teller effects [88-89, 117], polaronic [118-119] or bipolaronic [120] effects, strong on-site Coulomb interactions [121], and electronic phase separation [88, 122]. Time-resolved spectroscopy can be used to probe the dynamics of these intrinsic effects and to elucidate their relationship to the pseudogap.

5. 2. 2 Dispersion relation of the collective mode

Figure 23 shows a typical time evolution of ΔR for LCMO single crystal. The data are taken at 180 K with pump and probe wavelength of 800 nm. After the initial laser pulse excitation (process 1), the decay of ΔR clearly shows an oscillatory component on top of a multi-exponential decay (process 2, 4, 5). The slow oscillations (3) of ΔR are strongly overdamped. Only one, or at most two, oscillations can be observed in the trace of ΔR . The frequency of this mode is estimated to be ~ 30 GHz. To identify the origin of the slow oscillations, we performed spectroscopic measurements of ΔR in LCMO thin films as a function of probe wavelength in the range 400 nm to 5500 nm.

Figure 24 displays the coherent overdamped oscillations of the LCMO film at several probe wavelengths varied from ultraviolet (400 nm) to mid-infrared (2300 nm) without the exponential decaying part. The oscillatory signals can be observed in the

whole wavelength range. With increasing probe wavelength the oscillations become weaker and more damped. Two oscillations can be observed for the probe wavelength range from ultraviolet (~ 400 nm) to near-infrared (~ 1000 nm). However, only one oscillation is observed for probe wavelengths above 1250 nm. More interestingly, the

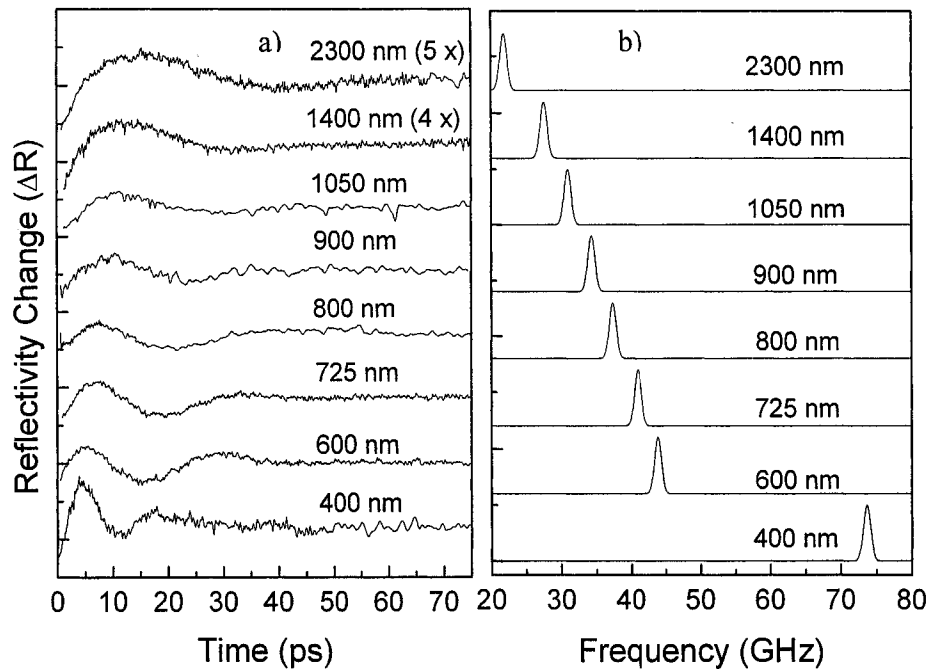


Figure 24. a) Time evolution of reflectivity change, ΔR for LCMO thin film with probe wavelengths varied from ultraviolet to mid-infrared; b) Fourier transforms of the ΔR traces shown in a).

oscillation component shows a strongly dispersive behavior.

The change of oscillation period can be well identified with the shift of the oscillation maximum and minimum. The oscillations become slower from ultraviolet to mid-infrared range (Fig. 24 (a)). As shown in Fig. 24 (b), the frequency of the

oscillations decreases from 73.83 GHz at 400 nm to 37.4 GHz at 800 nm to 21.8 GHz at 2300 nm.

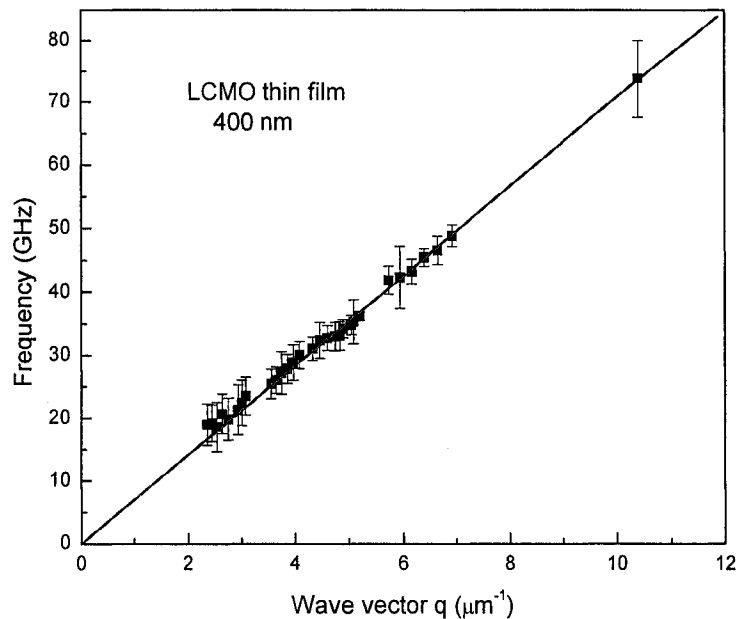


Figure 25. Collective mode dispersion relation of LCMO at room temperature.

The dispersion relation of the slow oscillation of ΔR in LCMO at room temperature is displayed in Fig. 25. The wave number is given by $q = 2n/\lambda$, where λ is the probe wavelength and n is the refractive index of LCMO [123]. By changing the wave vector of the probe photon the frequency of the oscillations in LCMO increased proportional to the wave number. The slope gives a phase velocity of $c_0 = 7.1 \pm 0.1 \times 10^3$ m/s.

The frequency of the coherent mode found to be independent of the polarization and wavelength of the pump beam. The wave-vector of the excited modes is determined by the phase-matching condition of the probe beam as described in Chap.

2. Since the absorption depth in LCMO is ~ 100 nm for wavelengths in the visible to infrared range, a broad spectrum of coherent modes are excited and propagate normal to the surface into the material up to frequency, ~ 2 THz. In what follows, we argue that the observed oscillations are due to a transverse phason in LCMO resulting from charge-ordering phase.

Most recently, Biswas *et al.* confirmed that the substrate strain can induce charge-ordering phases in LCMO based on their low-temperature magnetic force microscopy and magnetotransport measurements [124]. Additionally, charge-ordering characteristics in LCMO have been recently reported by Fäth *et al.* from scanning tunneling spectroscopy [109]. With this technique, a clear phase-separated state was observed below T_C using thin film [109].

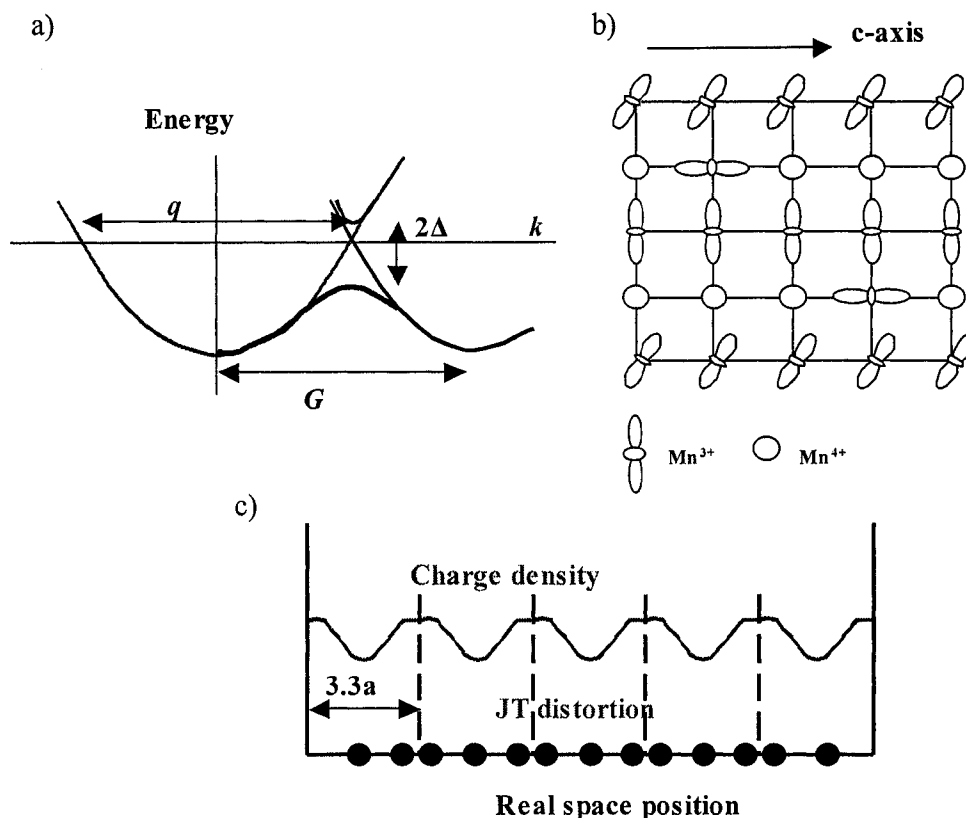


Figure 26. a) Schematic plot for density wave formation: k space as indicated from ARPES measurements; b) CE-type structure as proposed in LCMO along the c axis by Asaka *et al.*[42]; c) density wave formation in real space with a wave length of $3.3a$ for layered manganites [26].

New evidence for charge-ordering lies in the Fermi surface (FS) topology deduced by recent angle-resolved photoemission spectroscopy (ARPES) measurements of layered CMR oxide, $\text{La}_{1.2}\text{Sr}_{1.8}\text{Mn}_2\text{O}_7$ [13]. The authors suggested that key to many properties of the manganites appear to be parallel straight sections of the FS, which are highly susceptible to nesting instabilities [13]. The hole-like portions are very straight, more than expected from local spin density approximation calculation, especially near the corners of the hole pockets. Such straight parallel segments indicate that the electronic properties of these compounds should be considered as quasi-1D. This is consistent with recent experimental [126-127] and theoretical works [128] showing stripe ordering. The straight FS segments are also prone to produce (and originate from) nesting instabilities; that is, a large portion of the FS is connected in \vec{k} space to another reciprocal lattice vector \vec{q} . Figure 26a) shows the schematic plot explaining such an effect, where the main band hybridizes with an Umklapp band shifted by the amount \vec{G} in \vec{k} space. The hybridization opens a gap 2Δ , which lowers the electronic energy of the system. Fermi nesting means that large portions of the FS will be gapped, gaining more energy and making the distortion more likely, which is consistent with the insulating behavior above T_C .

The charge and orbital ordering in LCMO can be viewed as a quasi-one-dimensional electronic structure with reduced dimensionality as compared to the well-known charge-exchange (CE)-type structure: $d_{3x^2-r^2}$ or $d_{3y^2-r^2}$ orbital ordering of Mn^{3+} occurs along the c axis (Fig. 26(b)). The $d_{3z^2-r^2}$ orbital of Mn^{3+} is clipped by three Mn^{4+} ions. Such a regular pattern of the distinct charges modifies the uniformity of the charge density, leading to the development of the CDW condensate.

The coherent oscillations in our measurements show strong dependence of period, amplitude, and damping rate on the hole doping concentration and average A -site ion radius, r_A . This indicates that the observed oscillations are closely related to the charge density wave, i.e., the collective excitation mode.

We measured hole doping concentration dependence of ΔR in LMO. Similar to the LCMO sample, the reflectivity change, ΔR , also shows a slow oscillatory component on top of a bi-exponential decay in its parent compound LMO. However, the 800-nm data of LMO reveal a clearly different modulation period of ~ 45 ps, in contrast to ~ 27.6 ps observed in LCMO. The oscillations in LMO are weaker but persist longer.

Further evidence comes from the differences in the dependence of period, amplitude, and damping rate on the average A -site ion radius, r_A in LCMO and PCMO single crystals. The average A -site ion radius, r_A , is directly related to the electronic properties of the various manganite phases based on microscopic Hamiltonians, including strong electron-phonon JT and/or Coulomb interactions [88-89, 117, 121]. As reported by Fiebig et al., the modulation period for PCMO single crystal at 800 nm is ~ 40 ps [129], which is much longer than in LCMO.

Additionally, recent studies suggest that the ground states of manganite tend to be intrinsically inhomogeneous due to strong tendencies toward phase separation, typically involving ferromagnetic metallic and antiferromagnetic charge- and orbital-ordered insulating domains. The oscillations in the time-resolved spectroscopic data are due to the antiferromagnetic charge- and orbital-ordered insulating phases. As indicated by Dagotto et al., electronic phase separation between phases with different carrier densities leads to nanometer-scale coexisting clusters [12]. In contrast to the small damping rate in CDW conductors, the strongly overdamped behavior of the

oscillatory component in LCMO can be explained by the broad size distribution for the nanoscale regions and irregularly shaped mixed-phases [12]. Moreover, we do not observe any anisotropy in LCMO because of its percolative nature [12].

More details of our data (Fig. 26c) can be explained by the coupling of the nesting-induced CDW with the Jahn-Teller distortion. For example, as indicated by ARPES, the pseudogap depletes spectral weight from a large energy range (~ 1 eV) around E_F , which is a very large energy scale for a CDW-style gap alone (Fig. 21). Further, the gap edges are experimentally observed to be “soft” or gently sloping, as opposed to the sharp edges expected from a simple CDW gap (Fig. 20). The cooperation of the CDW with the Jahn-Teller distortion explains these unusual phenomena, as the typical energy scale of the Jahn-Teller distortion is near 1 eV. In addition, x-ray results indicate that the magnitude of the Jahn-Teller distortion varies in space, meaning that the resulting gap will have various energy scales and so the gap edge will be soft. This also implies that the carrier hopping probability t_{ij} will vary from one site to another. Recent theoretical calculations suggest that if such a variation in t_{ij} exists, then nanoscale phase separation and percolative conduction are expected [130].

5. 2. 3 Temperature evolution of the collective mode

Evidence for cooperation of CDW with Jahn-Teller distortion is found from the temperature evolution of the low-energy collective mode. Figure 27 shows measurements of ΔR from an LCMO thin film as a function of time delay Δt between the pump and probe beam at different temperatures near T_C . In addition to the

instantaneous electronic response to the pump pulse and two different decay processes, an overdamped oscillatory component is clearly observed for different temperatures.

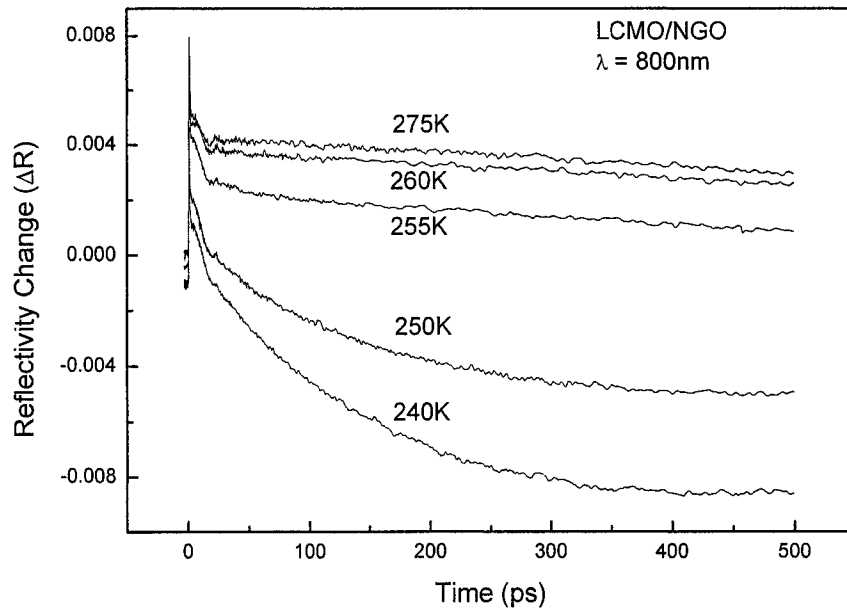


Figure 27. Transient reflectivity change ΔR of LCMO on NGO at different temperatures near T_C .

Figure 28 displays the coherent overdamped oscillations of the LCMO film at several temperatures (below and above T_C) without the exponentially decaying part. At $T \ll T_C$, the oscillations are less damped, three or more are observed due to a relatively small damping constant. With increasing temperature, the oscillations become more damped and only two are found around T_C due to a heavy damping constant. Above T_C the oscillations become stronger again. Figure 28 (b) shows the corresponding Fourier transforms of the signal transients of Fig. 28 (a). The frequency of the oscillations decreases from 64.1 GHz at 10 K to 35.3 GHz at T_C , and finally

increases to 53.75 GHz at room temperature. The oscillations exhibit clear softening near T_C .

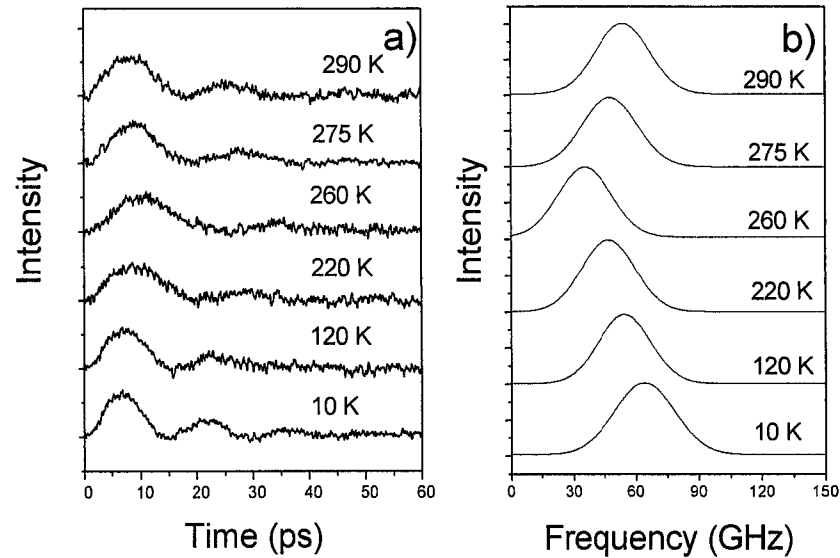


Figure 28. (a) Coherent oscillations of LCMO at different temperatures without decay components; (b) Fourier transforms of the signal transients shown in (a).

At a photon energy of 1.55 eV, the real part of the dielectric function of LCMO is constant with temperature as shown by Kim *et al* [123]. Therefore, the softening of the oscillations cannot be explained by collective modes of CDW alone, where the frequency shift would be related only to the background dielectric function. A cooperative Jahn-Teller type distortion of the MnO_6 octahedra coupled to the CDW can explain our results. This is in very good agreement with recent electrical transport measurements at low temperatures, which showed a strong coupling between the carriers and a low-frequency JT-distorted phonon mode [88-89, 117, 121].

X-ray diffuse scattering measurements and ARPES of a layered manganite, $\text{La}_{1.2}\text{Sr}_{1.8}\text{Mn}_2\text{O}_7$ give direct evidence for a slowly modulated cooperative Jahn-Teller-type distortion of the MnO_6 octahedra where the strength of the distortion is determined by the amplitude of the charge modulation [13, 131]. As shown in Fig. 29, if the MnO_6 octahedron is Jahn-Teller distorted, the probability that another MnO_6 octahedron is similarly distorted will oscillate within the sheet along the modulation direction, and approach zero with increasing distance from the origin due to the finite

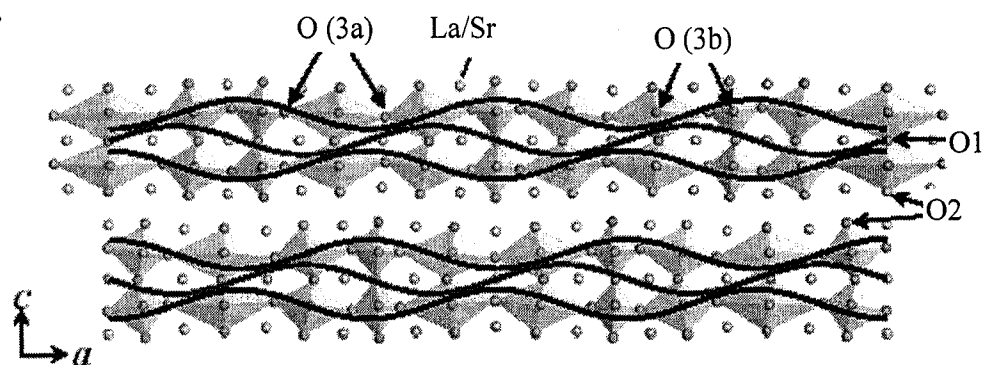


Figure 29. Crystallographic representation of the one-dimensionally modulated structure associated with CDW in a layered manganite, $\text{La}_{1.2}\text{Sr}_{1.8}\text{Mn}_2\text{O}_7$ [131].

range of correlations [131]. When viewed in this fashion, the smoothly varying pattern of orbital stripes that forms perpendicular to the modulation direction is readily apparent. The Jahn-Teller effect cooperates with the CDW and competes with the itinerancy energy of double exchange. The structural correlations cause complex rotations of the MnO_6 octahedra, exotic orderings of the electronic orbitals, and commensuration effects that relate to periodicity mismatches between the crystal lattice and the magnetic and electronic lattices [13, 131].

The softening of the collective mode may provide significant information about local structural changes associated with charge density fluctuations. As predicted by the soft-mode model of structural phase transitions, at each transition the frequency of

soft normal modes decreases as T_C is approached from above or below. In Fig. 28b), the Fourier spectra between 10 and 290 K show clearly structural phase transition behavior. In particular, we note that the frequency shift of the observed low frequency oscillations near T_C is comparable to those measured for internal TO phonon modes, i.e., the bending and stretching modes of the MnO_6 octahedra. This phonon consists mainly of a stretching vibration of the bond between the manganese ion and the oxygen ion, which is situated along the direction of the mode polarization. Therefore, the softening of collective mode is associated with the orthorhombic distortion of GdFeO_3 type.

5. 2. 4 Quasiparticle dynamics

Further information on electron-, lattice-, and spin- degree of freedom can be obtained from quasiparticle relaxation dynamics. As shown in Fig. 23, the decay of ΔR in the metallic phase of LCMO shows three-component behavior, two positive and one negative in magnitude. At low temperature ($T < T_C$), ΔR shows initially a fast positive bi-exponential decay with relaxation times $\tau_A = 0.5 \sim 4$ ps and $\tau_B = 50 \sim 100$ ps. The fast process reveals the thermalization of photoexcited quasi-particles which occurs on a time scale $\tau_{QP} = 0.3 \sim 3$ ps. The second process is characteristic for JT polaron relaxation and is related to the inhomogenous nature of the material. Here, we discuss the second process.

Figure 30 shows the temperature dependence of $\Delta R(t=0) = \Delta R_0$. The vertical dotted line denotes T_C as determined by electrical resistivity and magnetization measurements. To ensure that the pump-probe experiments are performed in the third-order regime we have measured the power dependence of ΔR_0 , and found the

expected linear dependence on the pump intensity (shown in the inset of Fig. 31). We also measured ΔR_0 as a function of temperature at two different power levels 15 and 27 mW (shown in Fig. 30). The temperature dependence of ΔR for the two power levels (ΔR_0 normalized at 260 K) is identical indicating that the pump intensity weakly perturbs the system.

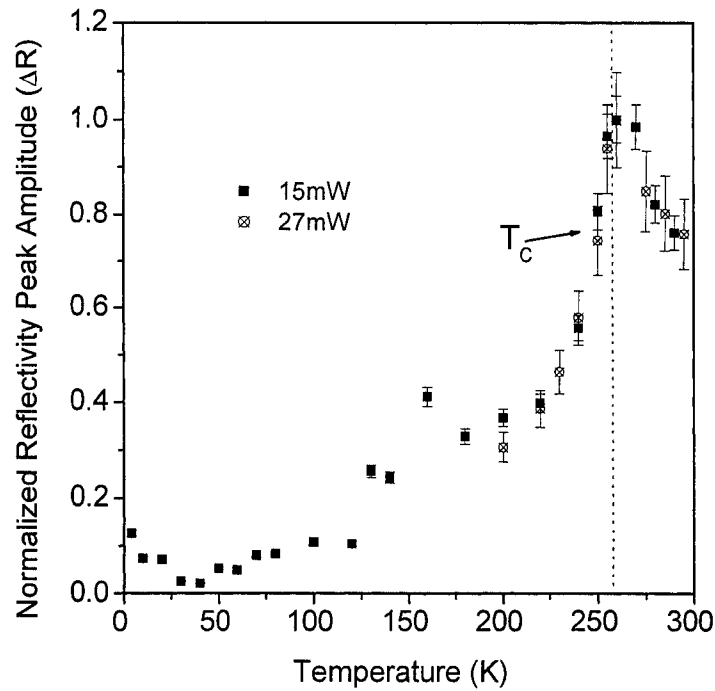


Figure 30. ΔR_0 of LCMO vs temperature for two different pump beam power.

In the optical spectrum, LCMO has a broad absorption band at 1.3 eV, which is evident in the paramagnetic phase. Several groups have attributed this 1.3 eV absorption band to charge transfer excitation of an electron from the lower JT split e_g level of a Mn^{3+} ion to the unoccupied and unsplit e_g level of adjacent Mn^{4+} ions [132]. Moreover, Zhao *et al.* found a fast conductive transient (~ 150 ps) in impulsive optical conductivity measurements from LCMO and attributed this component to the

photoionization of the Jahn-Teller small polaron close to T_C [132]. This interpretation is consistent with our data. As shown in Fig. 30, the excitation process is first enhanced with increasing temperature near T_C , i.e., from 230–260 K due to the increased overlap of the photon energy with the JT split e_g band. The transient reflectivity signal then decreases above T_C as the band broadens and the absorption decreases. At low temperature ($T \ll T_C$), ΔR gradually decreases with lowering temperature. The absorption behavior below T_C is consistent with a large polaron as indicated by Kim *et al* [123]. Further evidence for polaron formation is given by the temperature dependence of the fast relaxation time τ_B associated with the positive component of ΔR (shown in Fig. 31)). Based on the electronic nature of the optical

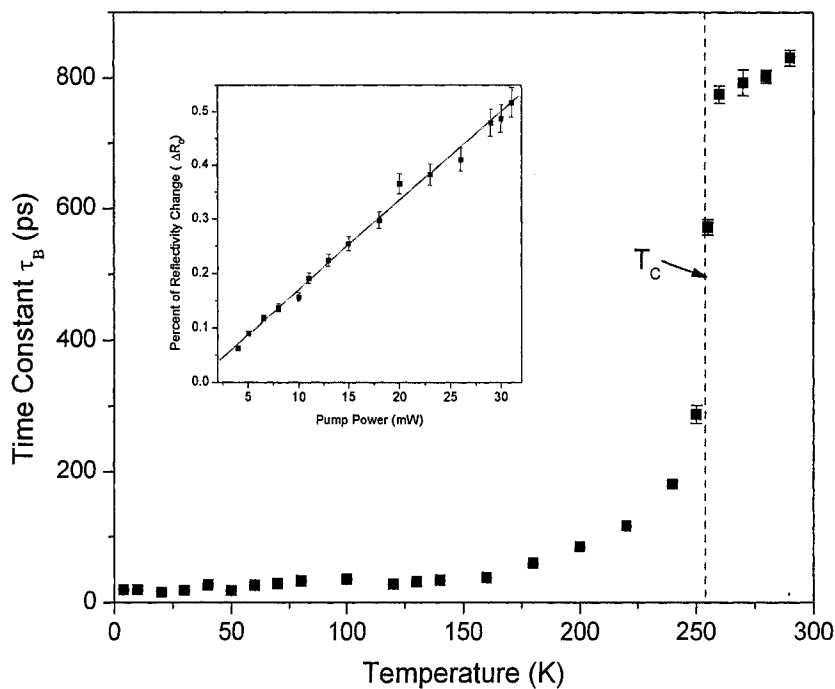


Figure 31. Temperature dependence of second fast relaxation component, τ_B ; Inset shows the power dependence of ΔR_0 .

transitions at 1.55 eV, the fast decay time τ_B is related to the thermalization and localization time of electrons made itinerant by photons. For the ferromagnetic metallic state, τ_B is found to be between 20 to 100 ps indicating the existence of itinerant large polarons. This component can still be observed around 4 K, well below T_C . Near T_C , Jahn-Teller effects begin to dominate, τ_B is enhanced by almost an order of magnitude due to the formation of JT small polaron, which will localize carriers. In the PI state (above T_C), $\tau_B > 800$ ps, because the localization time is relatively long.

However, recent studies have shown that individual polarons may not be sufficient to describe the carrier dynamics of manganites near the Curie temperature. Several theoretical and experimental results indicate that spatial phase separation may occur between hole-rich (FM) and hole poor (antiferromagnetic insulating) regions [109]. This tendency should be least for doping levels of LCMO in the middle of the FM regime. Still, evidence of charge inhomogeneities at low temperature was reported from muon spin resonance [103], x-ray absorption [104], and optical experiments [105-106], whereas at high temperatures polaronlike inhomogeneities were inferred from neutron scattering experiments [92, 107] and x-ray absorption [108]. The phase transition and associated magnetoresistance properties were also related to a percolation of metallic ferromagnetic domains from scanning tunneling spectroscopy [109]. The phase transition behavior shown in Figs. 30 and 31 also indicate the percolative nature of the MI transition. In particular the gradual increase of τ_B from 30 to 200 ps in the range from 150 to 250 K is indicative of the coexistence of high-volume region associated with delocalized carriers and a low-volume region associated with localized carriers. In this context, the spontaneous metal-to-insulator transition is associated with a low to high volume transition.

5. 2. 4 Slow spin relaxation process

In addition to the initial fast relaxation processes, a very long-lived negative ΔR remains sufficiently long, decay time $\tau_{SL} \sim 100 \mu s$, that a negative signal is clearly observable even after 1 ms in LCMO and LMO (Figs. 32a) and b)). Transient optical reflectivity and transmission measurements from charge-ordered PCMO, LCMO,

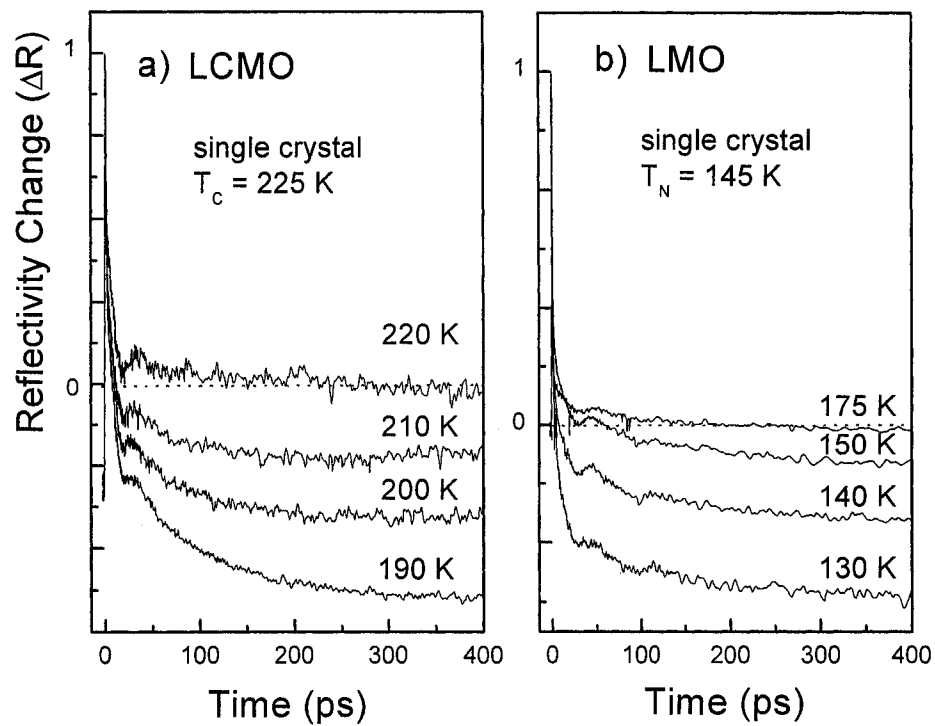


Figure 32. Transient reflectivity ΔR of: a) LCMO and b) LMO single crystals around T_C (or T_N) at 800 nm. The dotted lines indicate the zero position.

LSMO, and NSMO thin films, as well as, single crystals have also shown a negative long-lived component at low temperature. Further information on the long-lived

relaxation process in LCMO and LMO is obtained from the temperature dependence of ΔR measured at a time-delay $t = 500$ ps, referred to as $\Delta \tilde{R}$ (Fig. 32).

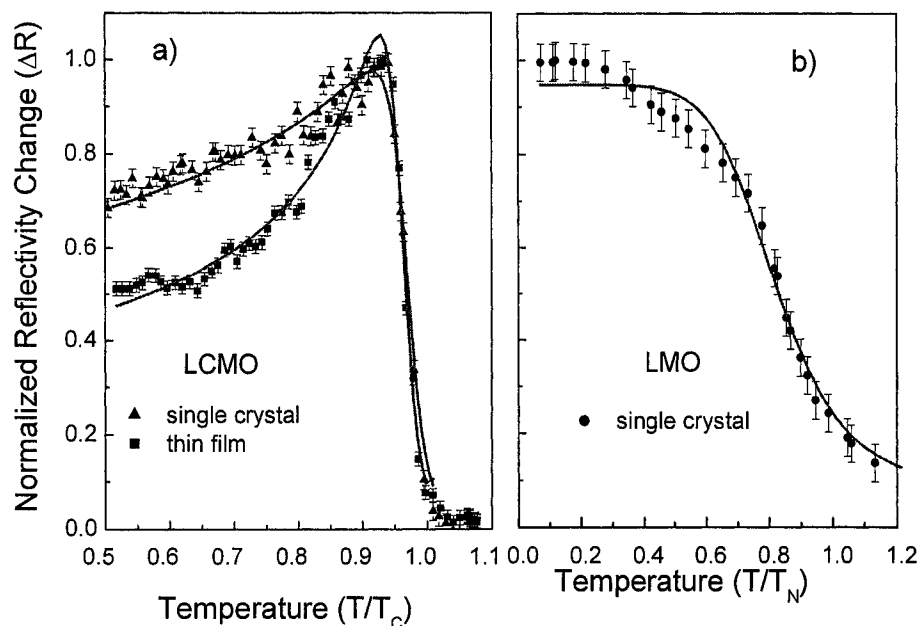


Figure 33. Temperature dependence of $\Delta \tilde{R}$ at $\Delta t = 500$ ps: a) LCMO single crystal ($\lambda_{\text{pump}} = 1.4 \mu\text{m}/\lambda_{\text{probe}} = 800$ nm) and 400-nm thin film ($\lambda_{\text{pump}} = 800$ nm/ $\lambda_{\text{probe}} = 5.2 \mu\text{m}$), and b) LMO single crystal ($\lambda_{\text{pump}} = 1.29 \mu\text{m}/\lambda_{\text{probe}} = 800$ nm). The solid lines indicate the power-law dependence.

The temperature dependence of $\Delta \tilde{R}$ for LCMO single crystal ($\lambda_{\text{pump}} = 1.4 \mu\text{m}/\lambda_{\text{probe}} = 800$ nm) and thin film ($\lambda_{\text{pump}} = 800$ nm/ $\lambda_{\text{probe}} = 5.2 \mu\text{m}$) are qualitatively the same and independent of wavelength (Fig. 33a)). The normalized $\Delta \tilde{R}$ increases with increasing temperature followed by an abrupt drop to zero around T_C . In contrast, for LMO ($\lambda_{\text{pump}} = 1.29 \mu\text{m}/\lambda_{\text{probe}} = 800$ nm) $\Delta \tilde{R}$ decreases slowly at low temperature and drops significantly around T_N (Fig. 33b)).

We observed this long-lived relaxation component both in the metallic and insulating phase as indicated in the transient optical reflectivity and transmission measurements from charge-ordered PCMO, LSMO, NSMO, and LCMO. But there is no evidence of this component in the transient reflectivity change of the paramagnetic phase as we measured from LSMO thin film, which shows a phase transition from ferromagnetic metal to paramagnetic metal at 325 K. Thus the component can only be related to the magnetic ordering phase, i.e., ferromagnetic or antiferromagnetic states. The non-zero $\Delta \tilde{R}$ above T_N indicates that a residual anti-ferromagnetic (AFM) order exists in LMO above the Neel temperature. The long-lived decay of $\Delta \tilde{R}$ is ascribed to a slow spin relaxation process.

The fact, that in both manganites $\Delta \tilde{R}$ drops nearly to zero above the transition temperature, is a strong indication that the long-lived $\Delta \tilde{R}$ signal arises: a) from a metastable excitation involving localized states, and b) that the decay of these states involves a spin-flip process. The lifetime $\tau_{SL} \sim 100 \mu s$ of these metastable states is comparable with the spin-lattice relaxation time measured by the μ SR technique [103]. Similar results have been reported by Kise *et al.* from time-resolved pump-probe magneto-optical Kerr study on the critical dynamics of the double exchange ferromagnet: $\text{Sr}_2\text{FeMoO}_6$ [23]. The authors suggested a slow spin relaxation process toward the quasi-equilibrium state through weak heat exchange with the reservoir at quasi-equilibrium temperature.

The solid line in Fig. 33b) shows that $\Delta \tilde{R}$ in LMO follows approximately a $(T_N - T)^\alpha$ dependence ($\alpha \cong 0.5$), which is similar to the temperature dependence of the magnetization. As the temperature approaches T_N and the magnetic order decreases in LMO, the metastable state excitations resulting from spin scattering decreases and $\Delta \tilde{R}$ starts to drop. In contrast to LMO, the T-dependence of $\Delta \tilde{R}$ is more complex in

LCMO. The transient reflectivity first increases with increasing temperature and then for $T > 0.9T_C$ follows a $(T_C - T)^\beta$ dependence with $\beta \approx 0.8 - 1$ (solid line in Fig. 33a)).

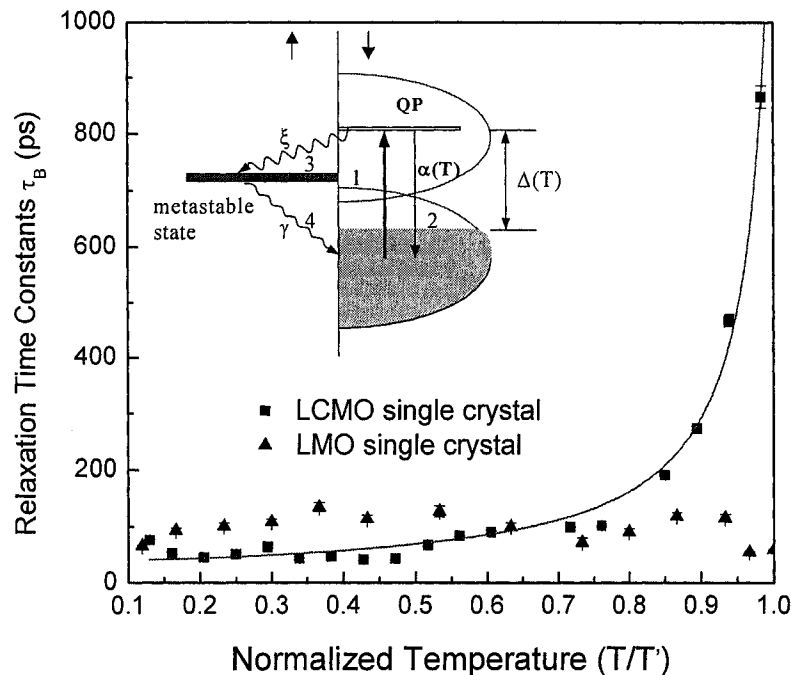


Figure 34. The relaxation time τ_B as a function of temperature T for LCMO and LMO single crystals. The solid line indicates the power-law dependence. The inset depicts a schematic diagram of carrier excitation/relaxation processes in LCMO.

The various processes giving rise to the photoinduced reflectivity change in LCMO are depicted in Fig. 34 (inset). An ultrashort laser pulse first excites electrons via interband transitions. These hot electrons very rapidly release their energy via electron-electron and electron-phonon collisions reaching QP states near the Fermi energy (step 1). The QPs can recombine with states in the pseudogap (step 2) or relax to metastable states via spin-flip processes (magnons are released) caused by strong electron-lattice coupling (step 3). The carriers in the metastable states will relax with a recombination rate $\gamma = 1/\tau_{SL}$, while magnons are absorbed (step 4). As the pseudogap

opens up with increasing temperature and the spectral weight of states at the Fermi level decreases the decay rate of excited QPs decreases (step 2) and more quasiparticles will be scattered into metastable states (step 3). This effect leads to the initial rise of $\Delta \tilde{R}$ which is inverse proportional to the density of states in the pseudogap, i.e., for $T \sim 0.9T_C$, $\Delta \tilde{R} \propto (T_C - T)^{-b}$ with $b \approx 0.3 - 0.5$ (solid line in Fig. 33a)).

Further information on the relaxation dynamics of photoexcited quasi-particles can be obtained from the polaron relaxation time τ_B . Figure 34 shows τ_B as a function of temperature for LMO and LCMO single crystals. In LMO single crystal, τ_B is found to be completely temperature independent below T_N consistent with a static Jahn-Teller gap. For LCMO single crystal, τ_B remains nearly constant below $0.45 T_C$ and starts to increase above $0.7T_C$. A similar T-dependence has been reported in LCMO thin films (Fig. 32). The relaxation time τ_B follows a $(T_C - T)^{-\beta}$ dependence, i.e. $\tau_B \propto 1/\Delta \tilde{R}$, shown as a solid line in Fig. 34. This result strongly supports our interpretation that the quasi-particle relaxation dynamics involves fully spin-aligned pseudogap states near E_F .

Recently, ultrafast melting of a charge-ordered state has been reported in the photo-irradiated colossal magnetoresistive compound PCMO [129]. Pump-probe spectroscopy experiments reveal the formation of a conducting phase with typical features of an insulator–metal transition after less than 1 ps [129]. This phase is metastable and can be maintained in $\sim \mu\text{s}$ time scale. The metastable states are determined by energy barriers with a wide distribution of energies that lead to a distribution of relaxation times and stretched exponential forms of relaxation. Thus, the temperature evolution of the long-lived relaxation component provides

quantitative insight into the structure of the free energy surface in the ordered phases of doped manganites and its temperature evolution [133].

5. 2. 5 Strain-effect on spin relaxation dynamics

Uniaxial lattice distortion can easily be introduced in thin films due to lattice mismatch between the film and substrate. Understanding the role of strain and

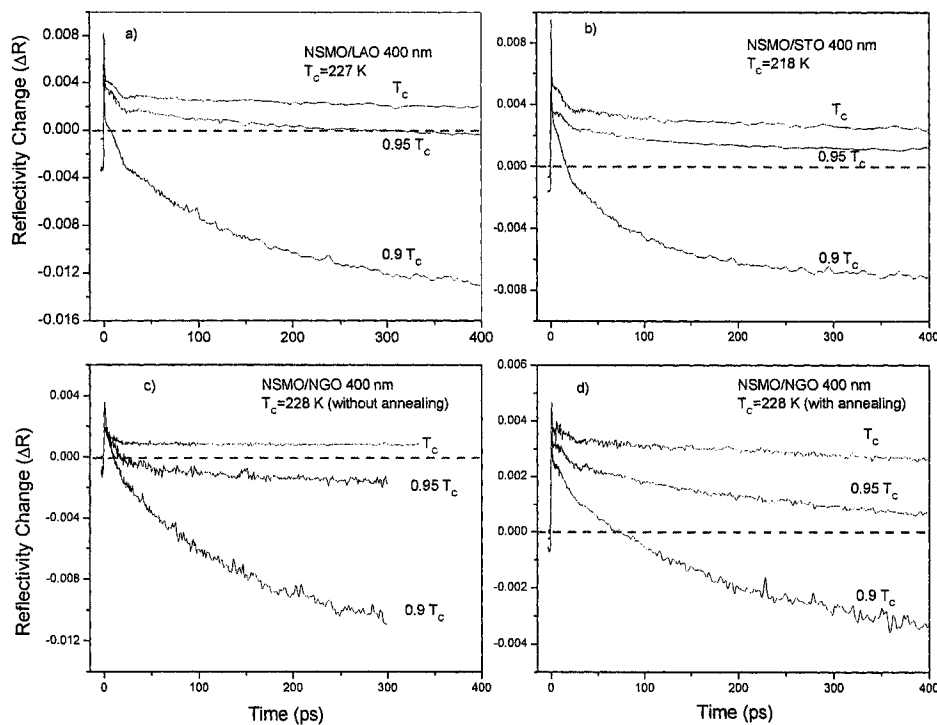


Figure 35. Transient reflectivity ΔR of NSMO (400 nm) on different substrates: (a) LaAlO_3 (001), (b) SrTiO_3 (001), NdGaO_3 (110), and (d) NdGaO_3 (110) with postoxygen annealing. The dotted lines indicate the zero line.

microstructure on magnetism and transport is a necessary step in elucidating the origin of CMR in manganites [134-143]. In this section, we report on the effect of strain on carrier relaxation dynamics in NSMO near the MI transition temperature.

NSMO thin films grown on three different types of substrates with thickness 400 nm and different growth condition (with or without post-annealing) are employed. The substrates are LaAlO_3 (001) (LAO), SrTiO_3 (001) (STO), and NdGaO_3 (110) (NGO), which can induce biaxial compressive, tensile, and very little strain in the NSMO thin films, respectively. The NSMO thin films were grown epitaxially on these substrates by pulsed laser deposition [144]. The samples were characterized by electrical resistivity and magnetization measurements (the Curie temperatures are 225 K, 215 K, and 228 K for LAO, STO, and NGO substrates respectively).

Figure 35 a) - d) shows measurements of ΔR from thin NSMO films on different substrates as a function of time delay t between the pump and probe beam at different temperatures. The dotted lines show the zero position. The decay of ΔR in the metallic phase of NSMO also shows three-component behavior, two positive and a negative one. The positive ones decay with characteristic times on the subpicosecond and picosecond time scale. Here, we mainly focus our discussion on the long-lived negative component of ΔR .

The temperature-dependent ΔR signal from NSMO thin films on different substrates (LAO, STO, and NGO) are quite distinct as shown in Fig. 35 (a) ~ (d). For instance, at $T = 0.95T_C$, the pump-probe signal drops below the zero line around $t \sim 250$ ps for the compressively strained NSMO thin film on LAO substrate (Fig. 35(a)), while for tensile strained NSMO thin film on STO substrate ΔR stays positive far beyond 400 ps (Fig. 35(b)), and for near-zero strained NSMO on NGO, ΔR becomes negative after only a few picoseconds (Fig. 35(c)). The transient reflectivity signal of the oxygen post-annealed NSMO sample grown on NGO is shifted towards positive values compared to the as-grown sample [Fig. 35(d)]. The positive part of the transient reflectivity signal becomes much longer (> 450 ps) for the annealed sample.

Figure 35 indicates that the relaxation dynamics of NSMO depends strongly on the strain, structure, and oxygen content of the film. The difference in dynamical behavior is attributed to changes in grain boundaries (unit cell volume) and long-range magnetic ordering.

The dynamics of the spin system in strained NSMO is very different from that

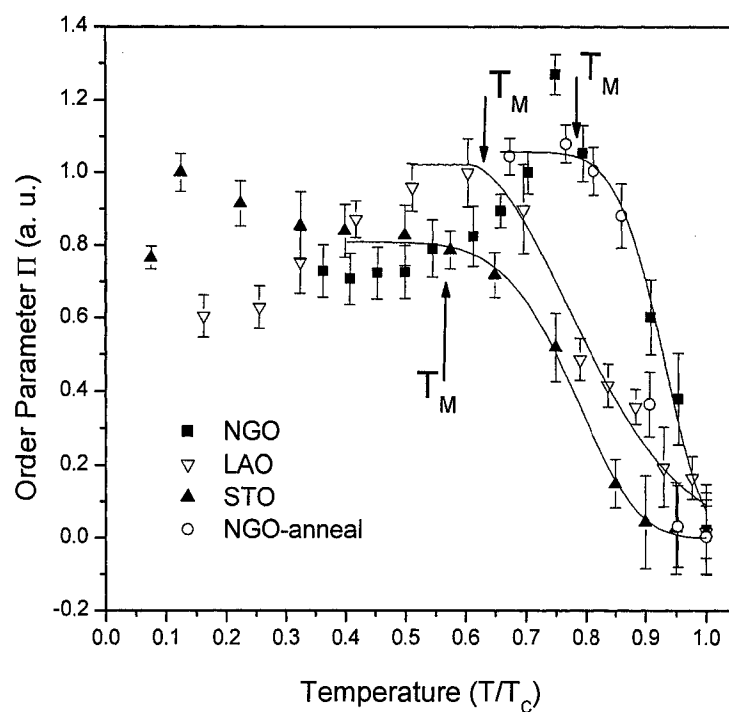


Figure 36. Long relaxation component Π vs the temperature obtained from ΔR for different strained NSMO thin films. The solid lines show fits Eq. (31).

of the unstrained material. The very slow spin thermalization process below T_c indicates the anomalously long spin wave relaxation in NSMO thin films (Fig. 35). The temperature dependence of the long relaxation component, Π , is in good

agreement with magnetic susceptibility measurements. As shown in Fig. 36, the dramatic change in Π as the temperature approaches T_C indicates that this negative component of ΔR directly reflects the critical behavior of the magnetic phase transition. Time-resolved reflectivity measurements provide us a unique opportunity to study the dynamics of the spin system and the order–disorder characteristics of the ferromagnetic–paramagnetic phase transition in NSMO [12].

The manganites tend to be intrinsically inhomogeneous due to a strong tendency towards phase separation. The phase separation has two different origins: (i) electronic phase separation between phases with different carrier densities that leads to nanometer scale coexisting clusters, and (ii) disorder induced phase separation with percolative characteristics between equal-density phases, driven by disorder near the first order metal–insulator transition. Both types of phase separation will qualitatively lead to similar temperature dependence of the order parameter. However, strain-induced static distortion waves will affect mainly the disorder induced phase separation. As shown in Fig. 36, the behavior of Π proceeds in two stages: above a “disordering” temperature T_M , a disordered paramagnetic phase appears, and the parameter Π exhibits a power-law dependence on the temperature. Systems with power-law decay of order-correlation parameters are said to have quasi-long-range order (QLRO) [145]. Thus, this intermediate state of mixed ferromagnetic metal and paramagnetic insulator phases clearly shows a temperature-dependent QLRO. Above T_C , the spin correlation is short range, and the ferromagnetic phase disappears.

The order-correlation parameter, i.e., Π , allows us to relate the critical behavior of the ordering parameter to the critical exponents of the static parameters, i.e., correlation length and spin-wave stiffness in the XY model. The QLRO–disorder transition is caused by reduced thermodynamic stiffness, similar to the Kosterlitz–

Thouless (KT) transition [146]. According to the two-dimensional XY model the order-correlation parameter, i.e., Π , diverges exponentially around T_M as:

$$\xi(T) \propto \exp\{B[T_M/(T-T_M)]^\nu\} \quad (31)$$

where $0.1696 < \nu < 0.4$. The solid lines in Fig. 36 show fits of Eq. (31) for NSMO films grown on different substrates. The arrows indicate the disordering temperature T_M of the different strained NSMO films. Figure 36 shows that the power-law decay of long-range correlations [Eq. (1)] depends strongly on the strain. Strain creates static distortion waves in the interfacial region caused by the thin film–substrate interaction potential and leads to the breakdown of long-range spin ordering. At low temperature, the disorder concentration is very low (tending exponentially toward zero with $T \rightarrow 0$ K) and the internal correlation inside the film does not change significantly in response to strain consistent with a constant value of Π . With an increase in temperature, static distortion waves caused by strain break down the order parameters. If the substrate is commensurate with the two-dimensional (2D) lattice, such as the NSMO thin film grown on a slightly strained NGO substrate, the strain force will be weaker and the long-range spin correlation can be kept toward higher temperature ($\sim 0.8T_C$). For incommensurate substrates, like in the case of NSMO on STO or LAO, the long-range spin correlation will be strongly disturbed by the creation of static distortion waves. Thus, the critical spin-disordering temperature T_M is much lower ($\sim 0.6T_C$) compared to the case of NSMO on NGO substrates. The “disordering” temperature T_M varies according to the creation of static distortion waves under different strain forces.

Chapter 6

Summary and conclusions

We have studied in detail the detected collective oscillation modes and the electronic and/or magnetic excitation and relaxation processes in CDW and CMR conductors in order to explore the low energy dynamics of different correlated phases, and elucidate the manner in which these dynamics evolve through low temperature phase transitions, e.g., metal-insulator, charge-ordering, ferromagnetic-paramagnetic. We have investigated the low-energy collective excitations of the charge-density wave in the quasi-one dimensional conductors: $K_{0.3}MoO_3$ and $K_{0.33}MoO_3$ by time-resolved two-color pump-probe spectroscopy. The dispersion relation of the transverse phase mode is measured in the frequency range from 5 – 40 GHz by time resolved transient reflectivity spectroscopy. We developed a model to describe the photogeneration and detection mechanism of collective modes based on light absorption in two-color pump probe experiments. According to the model, the dispersion of the long-wavelength phasons can be measured by changing the probe wavelength. The model

is sufficiently general to be applied to the investigation of low-energy collective mode excitations in colossal magnetoresistance materials as well as charge-density wave conductors.

Under weak light illumination (< 5 mW) of $\text{K}_{0.3}\text{MoO}_3$ at 30 K, the transverse phase mode exhibits an acoustic-like dispersion relation in the low-frequency limit, in agreement with the classical CDW theory [14, 70]. Furthermore, the phason velocity is anisotropic with the velocity perpendicular to the chains being significantly smaller. The amplitude mode exhibits a weak (optic-like) dispersion relation with a frequency of 1.66 THz at 30 K.

Our data obtained by femtosecond time-resolved spectroscopy on doped perovskite manganites show that the physics of low-energy collective modes is closely related to the opening of a pseudogap resulting from charge/orbital ordering phases. The charge and orbital ordering in LCMO can be viewed as a quasi-one-dimensional electronic structure with reduced dimensionality as compared to the well-known charge-exchange (CE)-type structure: $d_{3x^2-r^2}$ or $d_{3y^2-r^2}$ orbital ordering of Mn^{3+} occurs along the c axis. The $d_{3z^2-r^2}$ orbital of Mn^{3+} is clipped by three Mn^{4+} ions. Such a regular pattern of the distinct charges modifies the uniformity of the charge density, leading to the development of the CDW condensate. Moreover, the coupling of the nesting-induced CDW with the Jahn-Teller distortion explains the temperature evolution of our data. Such a regular pattern of the distinct charges modifies the uniformity of the charge density, leading to the development of a CDW condensate, which cooperates with Jahn-Teller distortion and compete with the electron itinerancy favored by double exchange. Evidence for this mechanism is provided by the temperature evolution of the low-energy collective mode. The softening of the oscillations cannot be explained by collective modes of CDW alone.

A cooperative Jahn-Teller type distortion of the MnO_6 octahedra coupled to the CDW is necessary to explain our results. This is in very good agreement with recent electrical transport measurements at low temperatures, which showed a strong coupling between the carriers and a low-frequency Jahn-Teller distorted phonon mode.

These observations led us to investigate quantitatively the photoexcited carrier relaxation dynamics in doped manganites. We show that the quasiparticle dynamics in the vicinity of a metal-insulator transition are strongly affected by the presence of a pseudogap, phase separation and percolation, which are strongly dependent on temperature. Further, a long-lived relaxation component is also observed, both in the metallic and insulating phase as indicated in the transient optical reflectivity and transmission measurements from various manganites. There is no evidence of this process in the transient reflectivity change of the paramagnetic phase as measured in LSMO thin film, which shows a phase transition from ferromagnetic metal to paramagnetic metal at 325 K. Therefore this long-lived process is strongly related to the magnetic ordering phase, i.e., ferromagnetic or antiferromagnetic states. The dynamics of the spin system in strained NSMO is found to be very different from that of the unstrained material. The very slow spin thermalization process below T_C indicates the anomalously long spin wave relaxation in NSMO thin films.

Bibliography

1. M. Imada, A. Fujimori, and Y. Tokura, "Metal-insulator transitions", *Rev. Mod. Phys.* 70, 1038 (1998).
2. Ed. By D. M. Ginsberg, "Physical properties of the high T_C superconductors", Vols. I-V, (World Scientific, Singapore, 1989).
3. A. Ramirez, "Colossal magnetoresistance", *Phys. Cond. Matt.* 9, 8171 (1997).
4. Y. Tokura and Y. Tomioka, "Colossal magnetoresistive manganites", *J. Magn. Magn. Materials* 200, 1 (1999).
5. J. M. D. Coey, M. Viret, and S. Von Molnar, "Mixed-valence manganites", *Adv. Phys.* 48, 167 (1999).
6. G. R. Stewart, "Heavy-fermion systems", *Rev. Mod. Phys.* 56, 755 (1984).
7. For a detailed description, see C.N.R. Rao, and B. Raveau, *Transition Metal Oxides* (VCH Publishers, New York, 1995).
8. Y. Tomioka, A. Asamitsu, Y. Moritomo, H. Kuwahara, and Y. Tokura, "Collapse of a charge-ordered state under a magnetic field in $\text{Pr}_{1/2}\text{Sr}_{1/2}\text{MnO}_3$ ", *Phys. Rev. Lett.* 74, 5108 (1995).
9. Y. Okimoto, Y. Tomioka, Y. Onose, Y. Otsuka, and Y. Tokura, "Charge ordering and disordering transition in $\text{Pr}_{1-x}\text{Ca}_x\text{MnO}_3$ ($x=0.4$) as investigated by optical spectroscopy", *Phys. Rev. B* 57, R9377 (1998).

10. V. Kiryuklin, D. Casa, J. P. Hill, B. Keimer, A. Vigliante, Y. Tomioka, and Y. Tokura, "An x-ray induced insulator-metal transition in a magnetoresistive manganite", *Nature* 386, 813 (1997).
11. E. Saitoh, S. Okamoto, K. T. Takahashi, K. Tobe, K. Yamamoto, T. Kimura, S. Ishihara, S. Maekawa, and Y. Tokura, "Observation of orbital waves as elementary excitations in a solid", *Nature* 410, 180 (2001).
12. E. Dagotto, T. Hotta, and A. Moreo, "Colossal magnetoresistant material: the key role of phase separation", *Phys. Rep.* 344, 1 (2001), and references therein.
13. Y. -D. Chuang, A. D. Gromko, D. S. Dessau, T. Kimura, and Y. Tokura, "Fermi surface nesting and nanoscale fluctuating charge/orbital ordering in colossal magnetoresistive oxides", *Science* 292, 1509 (2001).
14. G. Grüner, *Density Waves in Solids* (Addison-Wesley, Reading, MA, 1994); G. Grüner, "The dynamics of charge-density waves", *Rev. Mod. Phys.* 60, 1129 (1988) and reference therein.
15. R. von Helmolt, J. Wecker, B. Holzapfel, L. Schultz, and K. Samwer, "Giant negative magnetoresistance in perovskitelike $\text{La}_{2/3}\text{Ba}_{1/3}\text{MnO}_x$ ferromagnetic films", *Phys. Rev. Lett.* 71, 2331 (1993).
16. M. McCormack, S. Jin, T. H. Tiefel, R. M. Fleming, Julia M. Philips, and R. Ramesh, "Very large magnetoresistance in perovskite-like La-Ca-Mn-O thin films", *Appl. Phys. Lett.* 64, 3045 (1994).
17. S. Jin, T. H. Tiefel, M. McCormack, R. A. Fastnacht, R. Ramesh, and L. H. Chen, "Thousandfold change in resistivity in magnetoresistive La-Ca-Mn-O films", *Science* 264, 413 (1994).

18. P. Schiffer, A. P. Ramirez, W. Bao, and S.-W. Cheong, "Low Temperature Magnetoresistance and the Magnetic Phase Diagram of $\text{La}_{1-x}\text{Ca}_x\text{MnO}_3$ ", *Phys. Rev. Lett.* 75, 3336 (1995).
19. D. Mihailovic, C.J. Stevens, B. Podobnik, J. Demsar, M. Zavrtanik, D. Smith, J.F. Ryan, "Evidence for Two-Component Superconductivity in the Femtosecond Optical and Transient Photoconducting Response of $\text{YBa}_2\text{Cu}_3\text{O}_{7\pm\delta}$ ", *Physica C* 282-287, 186 (1997).
20. D. Mihailovic, B. Podobnik, J. Demsar, G. Wagner, and J. Evetts, "Divergence of the quasiparticle lifetime with doping and evidence for pre-formed pairs below T^* in $\text{YBa}_2\text{Cu}_3\text{O}_{7\pm\delta}$: Direct measurements by femtosecond time-resolved spectroscopy", *J. Phys. Chem. Sol.* 59, 1934 (1998).
21. V. V. Kabanov, J. Demsar, B. Podobnik, and D. Mihailovic, "Quasiparticle relaxation dynamics in superconductors with different gap structures: theory and experiments on $\text{YBa}_2\text{Cu}_3\text{O}_{7\pm\delta}$ ", *Phys. Rev. B* 59, 1497 (1999).
22. E. Beaurepaire, J.-C. Merle, A. Daunois, and J.-Y. Bigot, "Ultrafast Spin Dynamics in Ferromagnetic Nickel", *Phys. Rev. Lett.* 76, 4250 (1996).
23. T. Kise, T. Ogasawara, M. Ashida, Y. Tomioka, Y. Tokura, and M. Kuwata-Gonokami, "Ultrafast Spin Dynamics and Critical Behavior in Half-Metallic Ferromagnet: $\text{Sr}_2\text{FeMoO}_6$ ", *Phys. Rev. Lett.* 85, 1986 (2000).
24. R. A. Kaindl, M. Woerner, T. Elsaesser, D. C. Smith, J. F. Ryan, G. A. Farnan, M. P. McCurry, and D. G. Walmsley, "Ultrafast Mid-Infrared Response of $\text{YBa}_2\text{Cu}_3\text{O}_{7-\delta}$ ", *Science* 287, 470 (2000).
25. R. D. Averitt, A. I. Lobad, C. Kwon, S. A. Trugman, V. K. Thorsmolle, and A. J. Taylor, "Ultrafast Conductivity Dynamics in Colossal Magnetoresistance Manganites", *Phys. Rev. Lett.* 87, 017401 (2001).

26. Yuhang Ren, Gunter Lüpke et al., (to be published).
27. C. Thomsen, H. T. Grahn, H. J. Maris, and J. Tauc, "Surface generation and detection of phonons by picosecond light pulses", *Phys. Rev. B.* 34, 4129 (1986).
28. J. M. Chwalek, C. Uher, J. F. Whitaker, G. A. Mourou, and J. A. Agostinelli, "Subpicosecond time-resolved studies of coherent phonon oscillations in thin-film $\text{YBa}_2\text{Cu}_3\text{O}_{6+x}$ ($x < 0.4$)", *Appl. Phys. Lett.* 58, 980 (1991).
29. H. J. Zeiger, J. Vidal, T. K. Cheng, E. P. Ippen, G. Dresselhaus, M. S. Dresselhaus, "Theory for displacive excitation of coherent phonons", *Phys. Rev. B* 45, 768 (1992).
30. O. B. Wright, "Thickness and sound velocity measurement in thin transparent films with laser picosecond acoustics", *J. Appl. Phys.* 71, 1617 (1992).
31. J. Demsar, K. Biljakovic, and D. Mihailovic, "Single particle and collective excitations in the one-dimensional charge density wave solid $\text{K}_{0.3}\text{MoO}_3$ probed in real time by femtosecond spectroscopy", *Phys. Rev. Lett.* 83, 800 (1999).
32. P. B. Allen, "Theory of thermal relaxation of electrons in metals", *Phys. Rev. Lett.* 59, 1460 (1987).
33. A. I. Lobad, A. J. Taylor, C. Kwon, S. A. Trugman, and T. R. Gosnell, "Laser induced dynamic spectral weight transfer in $\text{La}_{0.7}\text{Ca}_{0.3}\text{MnO}_3$ ", *Chem. Phys.* 251, 227 (2000).
34. A. I. Lobad, R. D. Averitt, C. Kwon, and A. J. Taylor, "Spin-lattice interaction in colossal magnetoresistance manganites", *Appl. Phys. Lett.* 77, 4025 (2000).
35. A. I. Lobad, R. D. Averitt, and A. J. Taylor, "Picosecond dynamics of the spin-lattice relaxation in $\text{La}_{0.7}\text{Ca}_{0.2}\text{MnO}_3$: Magnetic-field dependence", *Phys. Rev. B* 63, R060410 (2001).
36. For example, see O. Madelung, "Introduction to Solid State Theory" (Springer Verlag, Berlin, 1978).
37. M. I. Kaganov, I. M. Lifshitz, L. V. Tantarov, "Relaxation between electrons and lattice", *Zh. Exsp. Theor. Fiz.* 31, 232 (1956) [*Sov. Phys. JETP* 4, 173 (1957)].
38. R. W. Schoenlein, W. Z. Lin, J. G. Fujimoto, G. L. Eesley, "Femtosecond studies of nonequilibrium electronic processes in metals", *Phys. Rev. Lett.* 58, 1680 (1987).

39. H. E. Elsayed-Ali, T. B. Norris, M. A. Pessot, and G. A. Mourou, "Time-resolved observation of electron-phonon relaxation in copper", *Phys. Rev. Lett.* 58, 1212 (1987).
40. J. G. Fujimoto, J. M. Liu, E. P. Ippen, N. Bloembergen, "Femtosecond laser interaction with metallic tungsten and nonequilibrium electron and lattice temperatures", *Phys. Rev. Lett.* 53, 1837 (1984).
41. P. B. Allen, "Empirical electron-phonon λ values from resistivity of cubic metallic elements", *Phys. Rev. B* 36, 2920 (1987).
42. P. B. Allen, "Neutron spectroscopy of superconductors", *Phys. Rev. B* 6, 2577 (1972).
43. S. D. Brorson, "Femtosecond thermomodulation measurements of transport and relaxation in metals and superconductors", thesis, Research Laboratory of Electronics, Massachusetts Institute of Technology, Cambridge, USA, 1990.
44. S. D. Brorson, A. Kazeroonian, J. S. Moodera, D. W. Face, T. K. Cheng, E. P. Ippen, M. S. Dresselhaus, G. Dresselhaus, "Femtosecond room-temperature measurement of the electron-phonon coupling constant γ in metallic superconductors", *Phys. Rev. Lett.* 64, 2172 (1990).
45. D. C. Hutchings, M. Sheik-Bahae, D. J. Hagan, E. W. Van Stryland, "Kramers-Kronig relations in nonlinear optics", *Opt. Quantum Electron.* 24, 1 (1992).
46. J. M. D. Coey, M. Viret, L. Ranno, "Electron Localization in Mixed-Valence Manganites", *Phys. Rev. Lett.* 75, 3910 (1995).
47. L. Ghivelder, I. Abrego Castillo, N. Mcn Alford, G. J. Tomka, P. C. Riedi, J. MacManus-Driscoll, A. K. M. Akther Hossain, L. F. Cohen, "Specific heat of $\text{La}_{1-x}\text{Ca}_x\text{MnO}_{3-\delta}$ ", *J. Magn. Magn. Mater.* 189, 274 (1998).

48. Y. H. Jeong, S. H. Park, T. Y. Koo, K. B. Lee, "Fisher-Langer relation and scaling in the specific heat and resistivity of $\text{La}_{0.7}\text{Ca}_{0.3}\text{MnO}_3$ ", *Solid State Ionics*. 108, 249 (1998).
49. J. J. Hamilton, E. L. Keatley, H. L. Ju, A. K. Raychaudhuri, V. N. Smolyaninova, R. L. Greene, "Low-temperature specific heat of $\text{La}_{0.67}\text{Ba}_{0.33}\text{MnO}_3$ and $\text{La}_{0.8}\text{Ca}_{0.2}\text{MnO}_3$ ", *Phys. Rev. B*. 54, 14926 (1996).
50. For a review of the Peierls transition, see J. P. Pouget and R. Comes in *Charge Density Waves in Solids*, edited by L. P. Gor'kov and G. Grüner (North Holland, Amsterdam, 1989), p. 85.
51. G. Travaglini, I. Mörke, P. Wachter, "CDW evidence in one-dimensional $\text{K}_{0.3}\text{MoO}_3$ by means of Raman scattering", *Sol. State. Comm.* 45, 289 (1983).
52. J. P. Pouget, B. Hennion, C. Escribe-Filippini, M. Sato, "Neutron-scattering investigations of the Kohn anomaly and of the phase and amplitude charge-density-wave excitations of the blue bronze $\text{K}_{0.3}\text{MoO}_3$ ", *Phys. Rev. B* 43, 8421 (1991).
53. E. Tutis, S. Barisic, "Dynamic structure factor of a one-dimensional Peierls system", *Phys. Rev. B* 43, 8431 (1991).
54. P. A. Lee, T. M. Rice, and P. W. Anderson, "Conductivity from charge or spin density waves", *Solid State Commun.* 22, 703 (1974).
55. J. Demsar, K. Biljakovic, and D. Mihailovic, "Single Particle and collective excitations in the one-dimensional charge density wave solid $\text{K}_{0.3}\text{MoO}_3$ probed in real time by femtosecond spectroscopy", *Phys. Rev. Lett.* 83, 800 (1999); J. Demsar, L. Forró, H. Berger, and D. Mihailovic, "Femtosecond snapshots of gap-forming charge-density-wave correlations in quasi-two-dimensional dichalcogenides $1T\text{-TaS}_2$ and $2H\text{-TaSe}_2$ ", *Phys. Rev. B* 66, 041101 (2002).

56. J. Demsar, "Photoexcited carrier relaxation in high temperature superconductors probed by ultrafast optical spectroscopy", Ph. D. thesis, University of Ljubljana, Ljubljana, Jan. 2002.
57. A. Virosztek and K. Maki, "Collective modes in charge-density waves and long-range Coulomb interactions", *Phys. Rev. B.* 48, 1368 (1993).
58. C. Thomsen, H. T. Grahn, H. J. Maris, J. Tauc, "Picosecond interferometric technique for study of phonons in the Brillouin frequency range", *Opt. Comm.* 60, 55 (1986).
59. Y. H. Ren, X. H. Zhang, G. Lüpke, M. Schneider and M. Onellion, I. E. Perakis, Y. F. Hu and Qi Li, "Observation of strongly damped GHz phonon-polariton oscillations in $\text{La}_{0.67}\text{Ca}_{0.33}\text{MnO}_3$ ", *Phys. Rev. B* 64, 144401 (2001).
60. M. H. Dunn and M. Ebrahimzadeh, "Parametric generation of tunable light from continuous-wave to femtosecond pulses", *Science* 286, 1513 (1999).
61. C. G. Durfee, S. Backus, M. M. Murnane, and H. C. Kapteyn, "Ultrabroadband phase-matched optical parametric generation in the ultraviolet by use of guided waves", *Opt. Lett.* 22, 1565 (1997).
62. U. Emmerichs, S. Woutersen, and H. J. Bakker, "Generation of intense femtosecond optical pulses around 3 μm with kHz rep-rate", *J. Opt. Soc. Am. B* 14, 1480 (1997).
63. Tsunami manual, Spectra-Physics.
64. Spitfire manual, Spectra-Physics.
65. OPA-600C manual, Spectra-Physics.
66. Zhuan Xu, Youxing Huang, Zhongqing Wu, Xuanjia Zhang, "Growth of red bronze $\text{K}_{0.33}\text{MoO}_3$ single crystals", *Materials Lett.* 57, 946 (2002).

67. C. S. Hong, W. S. Kim, E. O. Chi, K. W. Lee, and N. H. Hur, "Colossal magnetoresistance in $\text{La}_{0.7}\text{Ca}_{0.3}\text{MnO}_{3-\delta}$: comparative study of single-crystal and polycrystalline material", *Chem. Mater.* 12, 3509 (2000).
68. G. C. Xiong, Q. Li, H. L. Ju, S. N. Mao, L. Senapati, X. X. Xi, R. T. Greace, and T. Venkatesan, "Giant magnetoresistance in epitaxial $\text{Nd}_{0.7}\text{Sr}_{0.3}\text{MnO}_{3-\delta}$ thin films", *Appl. Phys. Lett.* 66, 1427 (1995).
69. For comprehensive reviews of CDWs, *Electronic Properties of Quasi-One-Dimensional Materials*, edited by P. Monceau, (Reidel, Dordrecht, 1985); *Low-Dimensional Electronic Properties of Molybdenum Bronzes and Oxides*, edited by C. Schlenker (Kluwer Academic Publishers, 1989); and *Physics and Chemistry of Low Dimensional Inorganic Conductors*, edited by C. Schlenker and M. Greenblatt (Plenum, New York, 1996), in press.
70. N. Kida and M. Tonouchi, "Spectroscopic evidence for a charge-density-wave condensate in a charge-ordered manganites: observation of a collective excitation in $\text{Pr}_{0.7}\text{Ca}_{0.3}\text{MnO}_3$ by using THz time-domain spectroscopy", *Phys. Rev. B* 66, 024401 (2002).
71. M. Karttunen, M. Haataja, K. R. Elder, and M. Grant, "Defects, order, and hysteresis in driven charge-density waves", *Phys. Rev. Lett.* 83, 3518 (1999).
72. R. E. Thorne, "Charge-density-wave conductors", *Physics Today*, May 1996, p. 42.
73. N. W. Ashcroft, N. D. Mermin, *Solid State Physics*, Holt, Rinehart and Winston, New York, 1976.
74. R. E. Peierls, *Quantum theory of solids*, Clarendon Press, Oxford, 1955.

75. T. W. Kim, D. Reagor, G. Grüner, K. Maki, A. Virosztek, "Temperature dependence of the charge-density-wave mass and relaxation time", *Phys. Rev. B* 40, 5372 (1989).
76. G. Travaglini, I. Mörke, P. Wachter, "CDW evidence in one-dimensional $K_{0.3}MoO_3$ by means of Raman scattering", *Sol. State. Comm.* 45, 289 (1983).
77. J. P. Pouget, B. Hennion, C. Escribe-Filippini, M. Sato, "Neutron-scattering investigations of the Kohn anomaly and of the phase and amplitude charge-density-wave excitations of the blue bronze $K_{0.3}MoO_3$ ", *Phys. Rev. B* 43, 8421 (1991).
78. T. E. Stevens, J. K. Wahlstrand, J. Kuhl, and R. Merlin, "Cherenkov radiation at speeds below the light threshold: phonon-assisted phase matching", *Science* 291, 627 (2001).
79. H.-Y. Hao and H. J. Maris, "Study of phonon dispersion in silicon and germanium at long wavelengths using picosecond ultrasonics", *Phys. Rev. Lett.* 84, 5556 (2000).
80. H.-Y. Hao and H. J. Maris, "Dispersion of the long-wavelength phonons in Ge, Si, GaAs, quartz, and sapphire", *Phys. Rev. B* 63, 224301 (2001).
81. G. Travaglini, P. Wachter, J. Marcus, and C. Schlenker, "Optical properties of the red bronze $K_{0.33}MoO_3$ ", *Sol. State. Comm.* 42, 407 (1982).
82. G. Mihaly, *Phys. Scr.* 29, 67(1989); G. Mihaly, T. W. Kim, and G. Grüner, *Phys. Rev. B* 39, R13009 (1989).
83. H. K. Ng, G. A. Thomas, and L. F. Schneemeyer, *Phys. Rev. B* 33, 8755 (1986).
84. S. Girault, A. H. Moudden, J. P. Pouget, "Critical x-ray scattering at the Peierls transition of the blue bronze", *Phys. Rev. B* 39, 4430 (1989).

85. C. Zener, "Interaction between the d -Shells in the Transition Metals. II. ferromagnetic compounds of manganese with perovskite structure", *Phys. Rev.* 82, 403 (1951).
86. P. W. Anderson and H. Hasegawa, "Considerations on double exchange", *Phys. Rev.* 100, 675 (1955).
87. P. G. de Gennes, "Effects of double exchange in magnetic crystals", *Phys. Rev.* 118, 141 (1960).
88. A. J. Millis, P. B. Littlewood, and B. I. Shraiman, "Dynamic Jahn-Teller Effect and Colossal Magnetoresistance in $\text{La}_{1-x}\text{Sr}_x\text{MnO}_3$ ", *Phys. Rev. Lett.* 77, 175 (1996).
89. A. J. Millis, "Fermi-liquid-to-polaron crossover. II. double exchange and the physics of colossal magnetoresistance", *Phys. Rev. B* 54, 5405 (1996).
90. H. Röder, J. Zhang, and A. R. Bishop, "Lattice effects in the colossal-magnetoresistance manganites", *Phys. Rev. Lett.* 76, 1356 (1996).
91. K. H. Kim, J. Y. Gu, H. S. Choi, G. W. Park, and T. W. Noh, "Frequency shifts of the internal phonon modes in $\text{La}_{0.7}\text{Ca}_{0.3}\text{MnO}_3$ ", *Phys. Rev. Lett.* 77, 1877 (1996).
92. J. M. De Teresa, M. R. Ibarra, P. A. Algarabel, C. Ritter, C. Marquina, J. Blasco, J. Garcia, A. Del Moral, Z. Arnold, "Evidence for magnetic polarons in the magnetoresistive perovskites", *Nature* 386, 256 (1997).
93. M. R. Ibarra, P. A. Algarabel, C. Marquina, J. Blasco, and J. García, "Large magnetovolume effect in Yttrium doped La-Ca-Mn-O perovskite", *Phys. Rev. Lett.* 75, 3541 (1995).

94. S. J. L. Billinge, R. G. DiFrancesco, G. H. Kwei, J. J. Neumeier, and J. D. Thompson, "Direct observation of lattice polaron formation in the local structure of $\text{La}_{1-x}\text{Ca}_x\text{MnO}_3$ ", *Phys. Rev. Lett.* 77, 715 (1996).
95. M. Jaime, H. T. Hardner, M. B. Salamon, M. Rubinstein, P. Dorsey, and D. Emin, "Hall-effect sign anomaly and small-polaron conduction in $(\text{La}_{1-x}\text{Gd}_x)_{0.67}\text{Ca}_{0.33}\text{MnO}_3$ ", *Phys. Rev. Lett.* 78, 951 (1997).
96. S. G. Kaplan, M. Quijada, H. D. Drew, D. B. Tanner, G. C. Xiong, R. Ramesh, C. Kwon, and T. Venkatesan, "Optical evidence for the dynamic Jahn-Teller effect in $\text{Nd}_{0.7}\text{Sr}_{0.3}\text{MnO}_3$ ", *Phys. Rev. Lett.* 77, 2081 (1996).
97. K. H. Kim, J. H. Jung, and T. W. Noh, "Polaron absorption in a perovskite manganite $\text{La}_{0.7}\text{Ca}_{0.3}\text{MnO}_3$ ", *Phys. Rev. Lett.* 81, 1517–1520 (1998).
98. A. Moreo, S. Yunoki, E. Dagotto, "Phase separation scenario for manganese oxides and related materials", *Science*, 283, 2034 (1999).
99. Y. Tokura, "Colossal Magnetoresistance Oxides", Y. Tokura, Ed. Gordon & Breach Science Publishers, UK 2000.
100. N. D. Mathur and P. B. Littlewood, "Mesoscopic texture in manganites", *Physics Today*, 56, 25 (2003).
101. N. D. Mathur, P. B. Littlewood, "The self-organised phases of manganites", *Solid State Commun.* 119, 271 (2001).
102. M. Uehara, S. Mori, C. H. Chen, S. -W. Cheong, "Percolative phase separation underlies colossal magnetoresistance in mixed-valent manganites", *Nature* 399, 560 (1999).
103. R. H. Heffner, L. P. Le, M. F. Hundley, J. J. Neumeier, G. M. Luke, K. Kojima, B. Nachumi, Y. J. Uemura, D. E. MacLaughlin, and SW. Cheong,

- “Ferromagnetic ordering and unusual magnetic ion dynamics in $\text{La}_{0.67}\text{Ca}_{0.33}\text{MnO}_3$ ”, *Phys. Rev. Lett.* 77, 1869 (1996).
104. C. H. Booth, F. Bridges, G. H. Kwei, J. M. Lawrence, A. L. Cornelius, and J. J. Neumeier, “Lattice effects in $\text{La}_{1-x}\text{Ca}_x\text{MnO}_3$ ($x=0 \rightarrow 1$): Relationships between distortions, charge distribution, and magnetism”, *Phys. Rev. B* 57, 10 440 (1998).
105. S. Yoon, H. L. Liu, G. Schollerer, S. L. Cooper, P. D. Han, D. A. Payne, S.-W. Cheong, and Z. Fisk, “Raman and optical spectroscopic studies of small-to-large polaron crossover in the perovskite manganese oxides”, *Phys. Rev. B* 58, 2795 (1998).
106. H. L. Liu, S. Yoon, S. L. Cooper, S. -W. Cheong, P. D. Han, and D. A. Payne, “Probing anisotropic magnetotransport in manganese perovskites using Raman spectroscopy”, *Phys. Rev. B* 58, R10 115 (1998).
107. J. W. Lynn, R. W. Erwin, J. A. Borchers, Q. Huang, A. Santoro, J-L. Peng, and Z. Y. Li, “Unconventional ferromagnetic transition in $\text{La}_{1-x}\text{Ca}_x\text{MnO}_3$ ”, *Phys. Rev. Lett.* 76, 4046 (1996).
108. A. Lanzara, N. L. Saini, M. Brunelli, F. Natali, and A. Bianconi, P. G. Radaelli, S. -W. Cheong, “Crossover from large to small Polarons across the metal-insulator transition in manganites”, *Phys. Rev. Lett.* 81, 878 (1998).
109. M. Fäth, S. Freisem, A. A. Menovsky, J. Aarts, and J. A. Mydosh, “Spatially inhomogeneous metal-insulator transition in doped manganites”, *Science* 285, 1540 (1999).
110. D. S. Dessau, T. Saitoh, C. -H. Park, Z.-X. Shen, P. Villeda, N. Hamada, Y. Moritomo, and Y. Tokura, “ k -dependent electronic structure, a large “ghost”

- fermi surface, and a pseudogap in a layered magnetoresistive oxide”, *Phys. Rev. Lett.* 81, 192 (1998).
111. T. Saitoh, D. S. Dessau, Y. Moritomo and T. Kimura, Y. Tokura, N. Hamada, “Temperature-dependent pseudogaps in colossal magnetoresistive oxides”, *Phys. Rev. B* 62, 1039 (2000).
 112. G. L. Eesley, “Observation of non-equilibrium heating in copper”, *Phys. Rev. Lett.* 51, 2140 (1983).
 113. J. H. Park, E. Vescovo, H. -J. Kim, C. Kwon, R. Ramesh, and T. Venkatesan, “Direct evidence for a half-metallic ferromagnet”, *Nature* 392, 794 (1998).
 114. R. Joynt, “Pseudogaps and extrinsic losses in photoemission experiments on poorly conducting solids”, *Science* 284, 777 (1999).
 115. D. S. Dessau and T. Saitoh, “Intrinsic versus extrinsic pseudogaps in photoemission spectra of poorly conducting solids”, *Science* 287, 767a (2000).
 116. K. Schultz, M. A. James, P. G. Steeneken, and G. A. Sawatzky, R. Suryanarayanan, G. Dhalenne, and A. Revcolevschi, “Weight of zero-loss electrons and sum rules in extrinsic processes that can influence photoemission spectra”, *Phys. Rev. B* 63, 165429 (2001).
 117. D. J. Singh and W. E. Pickett, “Pseudogaps, Jahn-Teller distortions, and magnetic order in manganite perovskites”, *Phys. Rev. B* 57, 88 (1998).
 118. A. J. Millis, P. B. Littlewood, B. I. Shraiman, “Double exchange alone does not explain the resistivity of $\text{La}_{1-x}\text{Sr}_x\text{MnO}_3$ ”, *Phys. Rev. Lett.* 74, 5144 (1995).
 119. H. Roder, J. Zang, A. I. Bishop, “Lattice effects in the colossal-magnetoresistance manganites”, *Phys. Rev. Lett.* 76, 1356 (1996).
 120. A. S. Alexandrov and A. M. Bratkovsky, “Carrier density collapse and colossal magnetoresistance in doped manganites”, *Phys. Rev. Lett.* 82, 141 (1999).

121. V. Ferrari, M. J. Rozenberg, R. Weht, “The anomalous metallic ferromagnetic state of Sr doped manganites”, preprint available at <http://xxx.lanl.gov/abs/cond-mat/9906131>.
122. A. Moreo, M. Mayr, A. Feiguin, S. Yunoki, E. Dagotto, “Giant cluster coexistence in doped manganites and other compounds”, *Phys. Rev. Lett.* 84, 5568 (2000).
123. K. H. Kim, J. Y. Gu, H. S. Choi, G. W. Park, and T. W. Noh, “Frequency shifts of the internal phonon modes in $\text{La}_{0.7}\text{Ca}_{0.3}\text{MnO}_3$ ”, *Phys. Rev. Lett.* 77, 1877 (1996).
124. A. Biswas, M. Rajeswari, R. C. Srivastava, T. Venkatesan, R. L. Greene, Q. Lu, A. L. de Lozanne, A. J. Millis, “Strain-driven charge-ordered state in $\text{La}_{0.67}\text{Ca}_{0.33}\text{MnO}_3$ ”, *Phys. Rev. B* 63, 184424 (2001).
125. T. Asaka, S. Yamada, S. Tsutsumi, C. Tsuruta, K. Kimoto, T. Arima, and Y. Matsui, “Charge/orbital ordering structure of $\text{Pr}_{1-x}\text{Ca}_x\text{MnO}_3$ ($x=3/8$) examined by low-temperature transmission electron microscopy”, *Phys. Rev. Lett.* 88, 097201 (2002).
126. K. H. Kim, S. Lee, T. W. Noh, and S. -W. Cheong, “Charge Ordering Fluctuation and Optical Pseudogap in $\text{La}_{1-x}\text{Ca}_x\text{MnO}_3$ ”, *Phys. Rev. Lett.* 88, 167204 (2002).
127. S. Mori, C. H. Chen, and S. -W. Cheong, “Pairing of charge-ordered stripes in $(\text{La,Ca})\text{MnO}_3$ ”, *Nature* 392, 473 (1998).
128. T. Hotta, A. Feiguin, E. Dagotto, “Topological Scenario for Stripe Formation in Manganese Oxides”, *Phys. Rev. Lett.* 84, 2477 (2000).

129. M. Fiebig, K. Miyano, Y. Tomioka, and Y. Tokura, “Sub-picosecond photo-induced melting of a charge-ordered state in a perovskite manganite”, *Appl. Phys. B* 71, 211 (2000).
130. M. Mayr, A. Moreo, J. A. Vergés, J. Arispe, A. Feiguin, and E. Dagotto, “Resistivity of mixed-phase manganites”, *Phys. Rev. Lett.* 86, 135 (2001).
131. B. J. Campbell, R. Osborn, D. N. Argyriou, L. Vasiliu-Doloc, J. F. Mitchell, S. K. Sinha, U. Ruett, C. D. Ling, Z. Islam, and J. W. Lynn, “Structure of nanoscale polaron correlations in $\text{La}_{1.2}\text{Sr}_{1.8}\text{Mn}_2\text{O}_7$ ”, *Phys. Rev. B* 65, 014427 (2002).
132. Y. G. Zhao, J. J. Li, R. Schreekala, H. D. Drew, C. L. Chen, W. L. Cao, C. H. Lee, M. Rajeswari, S. B. Ogale, R. Ramesh, G. Baskaran, and T. Venkatesan, *Phys. Rev. Lett.* 81, 1310 (1998).
133. R. M. Roshko and C. Viddal, “Modelling the magnetic response within the ferromagnetic phase of the substituted perovskite $\text{La}_{0.7}\text{Sr}_{0.3}\text{MnO}_3$ ”, *J. Appl. Phys.* (to be published)
134. Y. H. Ren, H. B. Zhao, G. Lüpke, Y. F. Hu and Qi Li, “Strain-dependent spin dynamics in $\text{Nd}_{0.67}\text{Sr}_{0.33}\text{MnO}_3$ near the metal–insulator transition”, *J. Appl. Phys.* 91, 7514 (2002).
135. R. V. Helmolt, J. Wecker, B. Holzapfel, L. Schultz, and K. Samwer, “Giant negative magnetoresistance in perovskitelike $\text{La}_{2/3}\text{Ba}_{1/3}\text{MnO}_x$ ferromagnetic films”, *Phys. Rev. Lett.* 71, 2331 (1993).
136. H. L. Ju, C. Kwon, Q. Li, R. L. Greene, and T. Venkatesan, “Giant magnetoresistance in $\text{La}_{1-x}\text{Sr}_x\text{MnO}_z$ films near room temperature”, *Appl. Phys. Lett.* 65, 2108 (1994).

137. L. M. Berndt, V. Balbarin, and Y. Suzuki, "Magnetic anisotropy and strain states of (001) and (110) colossal magnetoresistance thin films", *Appl. Phys. Lett.* 77, 2903 (2000).
138. K. A. Thomas, P. S. I. P. N. De Silva, L. F. Cohen, A. Hossain, M. Rajeswari, T. Venkatesan, R. Hiskes, and J. L. MacManus-Driscoll, "Influence of strain and microstructure on magnetotransport in $\text{La}_{0.7}\text{Ca}_{0.3}\text{MnO}_3$ thin films", *J. Appl. Phys.* 84, 3939 (1998).
139. S. Jin, T. H. Tiefel, M. McCormack, H. M. O'Bryan, L. H. Chen, R. Ramesh, and D. Schurig, "Thickness dependence of magnetoresistance in La-Ca-Mn-O epitaxial films", *Appl. Phys. Lett.* 67, 557 (1995).
140. S. E. Lofland, S. M. Bhagat, H. L. Ju, G. C. Xiong, T. Venkatesan, R. L. Greene, and S. Tyagi, "Ferromagnetic resonance and intrinsic properties of $\text{La}_{0.67}\text{Ba}_{0.33}\text{MnO}_z$ ", *J. Appl. Phys.* 79, 5166 (1996).
141. C. Kwon, M. C. Robson, K.-C. Kim, J. Y. Gu, S. E. Lofland, S. M. Bhagat, Z. Trajanovic, M. Rajeswari, T. Venkatesan, A. R. Kratz, R. D. Gomez, and R. Ramesh. "Stress-induced effects in epitaxial ($\text{La}_{0.7}\text{Sr}_{0.3}\text{MnO}_3$ films", *J. Magn. Mater.* 172, 229 (1997).
142. H. S. Wang and Q. Li, "Strain-induced large low-field magnetoresistance in $\text{Pr}_{0.67}\text{Sr}_{0.33}\text{MnO}_3$ ultrathin films", *Appl. Phys. Lett.* 73, 2360 (1998).
143. Y. Suzuki, Y. Wu, J. Yu, U. Ruediger, A. D. Kent, T. K. Nath, and C. B. Eom, "Domain structure and magnetotransport in epitaxial colossal magnetoresistance thin films", *J. Appl. Phys.* 87, 6746 (2000).
144. G. C. Xiong, Q. Li, H. L. Ju, S. N. Mao, L. Senapati, X. X. Xi, R. T. Greace, and T. Venkatesan, "Giant magnetoresistive memory effect in $\text{Nd}_{0.7}\text{Sr}_{0.3}\text{MnO}_3$ ", *Appl. Phys. Lett.* 66, 1427 (1995).

145. M. Chaikin and T. C. Lubensky, *Principles of Condensed Matter Physics*, Cambridge University Press, Cambridge, UK, 1995, p. 296.
146. J. M. Kosterlitz and D. J. Thouless, "Ordering, metastability and phase transitions in two-dimensional systems", *J. Phys. C* 6, 1181 (1973).

Vita

Yu-Hang Ren

The author was born on September 16, 1971, in Dong Yang, Zhejiang, China. He completed his Bachelor of Science degree in Physics with Honors in May 1995 and entered the Graduate School at Zhejiang University in August 1995. He completed his Ph. D work for Condensed Matter Physics in May 1999. The author entered the graduate program at the College of William and Mary in 1999. With the completion of this thesis and satisfaction in all other degree requirements, the author completed his Ph. D degree in Applied Science department under scientific supervision of Dr. Gunter Lüpke (Laser & Optics, Electronic materials), April 2003.